

Instant FLIM enables 4D *in vivo* lifetime imaging of intact brains

Yide Zhang^{1,6}, Ian H. Guldner^{2,4,5}, Evan L. Nichols^{2,3}, David Benirschke¹,

Cody J. Smith^{2,3}, Siyuan Zhang^{2,4,5} & Scott S. Howard^{1,4*}

¹*Department of Electrical Engineering, University of Notre Dame, Notre Dame, IN, USA*

²*Department of Biological Sciences, University of Notre Dame, Notre Dame, IN, USA*

³*Center for Stem Cells and Regenerative Medicine, University of Notre Dame, IN, USA*

⁴*Mike and Josie Harper Cancer Research Institute, University of Notre Dame, IN, USA*

⁵*Indiana University Melvin and Bren Simon Cancer Center, Indianapolis, IN, USA*

⁶*Caltech Optical Imaging Laboratory, Andrew and Peggy Cherng Department of Medical*

Engineering, California Institute of Technology, Pasadena, CA, USA

*Correspondence should be addressed to S.S.H. (showard@nd.edu)

Abstract

Traditional fluorescence microscopy is blind to molecular microenvironment information that is present in the emission decay lifetime. With fluorescence lifetime imaging microscopy (FLIM), physiological parameters such as pH, refractive index, ion concentration, dissolved gas concentration, and fluorescence resonance energy transfer (FRET) can be measured. Despite these benefits, existing FLIM techniques are typically slow, noisy, and hard to implement due to expensive instrumentation and complex post-processing. To overcome these limitations, we present instant FLIM, a method that allows real-time acquisition and display of two-photon intensity, lifetime, and phasor imaging data. Using analog signal processing, we demonstrate *in vivo* four-dimensional (4D) FLIM movies by imaging mouse and zebrafish glial cell response to injury over 12 hours through intact skulls. Instant FLIM can be implemented as an upgrade to an existing multiphoton microscope using cost-effective off-the-shelf components, requires no data post-processing, and is demonstrated to be compatible with FD-FLIM super-resolution techniques.

Main

Imaging molecular contrast is essential to continued advances in cellular biology. Fluorescence microscopy has been a significant tool over the past decades in imaging cellular and sub-cellular molecular contrast¹. Traditional fluorescence microscopy typically obtains molecular contrast by labelling parts of cells with different fluorophores and imaging emission intensity while changes in the molecular microenvironment are captured with FLIM. When combined with multiphoton microscopy (MPM)^{2,3}, FLIM can provide lifetime measurements *in vivo* with 3D resolution, deep penetration, and reduced photodamage^{4,5}. Despite the wealth of information provided by lifetime,

widespread use of FLIM in biomedical imaging has been limited due to slow acquisition and data processing speed, low signal-to-noise ratio (SNR), and high instrumentation cost⁶⁻¹¹.

State-of-the-art time-domain (TD)¹⁰⁻¹² or frequency-domain^{7,8,13,14} (FD) FLIM techniques have been reported to overcome the limitations of FLIM. A high-speed TD-FLIM system utilized a high-frequency digitizer to directly sample the fluorescence signal and achieved high-speed imaging of metabolic dynamics in living cells¹¹. Another TD-FLIM system employed the analog mean-delay method to accelerate lifetime measurements and realized real-time visualization of fixed tissues¹⁰. For FD-FLIM techniques, the recently proposed siFLIM method used a dedicated camera to demonstrate video-rate lifetime imaging of living cells¹⁴. Another prominent FD-FLIM method is FastFLIM, which utilized digital heterodyning and achieved an optimal photon efficiency⁸. Although these techniques have shown great promise in increasing the speed, improving the SNR, or reducing the cost of FLIM systems, none of them can simultaneously tackle all these challenges. Furthermore, these challenges become more significant for *in vivo* FLIM in deep tissue, where useful ballistic photons are scarce due to severe scattering, and prolonged imaging time is not feasible because of animal movements¹⁵.

Here, we demonstrate instant FLIM, an MPM-FLIM system that simultaneously addresses the challenges in speed, SNR, and implementation faced by existing FLIM techniques. The implementation diagram of instant FLIM is shown in **Fig. 1a (Supplementary Figs. 1,2)**. The parallel, analog computing in instant FLIM enables simultaneous, real-time measurement of fluorophore intensity, lifetime, and lifetime phasor plots^{16,17} for multiple decay analysis and real-time segmentation (**Fig. 1b,c, Supplementary Fig. 3, Supplementary Notes 1-3**). Furthermore,

instant FLIM approaches the theoretically ideal FLIM SNR performance by employing the mode-locked ultrafast pulses as the modulation source^{6,9} (**Supplementary Fig. 4, Supplementary Note 4**), demonstrating imaging and analysis in 12 $\mu\text{s}/\text{pixel}$ (**Supplementary Table 2**). Moreover, instant FLIM can be implemented easily by upgrading existing two-photon microscopes using off-the-shelf RF components and our open-source software (**Supplementary Protocols 1,2**). Finally, instant FLIM is deconvolution-free and fit-free, as lifetime images and phasor plots can be generated instantaneously through basic matrix operations with no extra computation time or memory, eliminating the bottleneck of state-of-the-art FLIM systems^{8,10,11}.

The real-time signal processing and near-ideal mode-locked pulses in instant FLIM enables high-speed computation of lifetime phasor plots and super-resolution imaging. Phasor plots facilitate FLIM analysis by resolving fluorescence heterogeneity through performing Fourier transforms on fluorescence decay signals¹⁶. Instant FLIM enables phasor plots generation at the same speed as intensity images without computing Fourier transforms (**Fig. 1d,e, Supplementary Fig. 5, Supplementary Video 1**). This high-speed analysis allows real-time labeling of pixels with similar phasor components (g and s)^{16,18} by two complementary approaches: the manual region of interest (ROI) labeling and the unsupervised machine learning (K-means clustering) approaches¹⁹ (**Fig. 1f**). Additionally, super-resolution FLIM images are generated by combining instant FLIM with generalized stepwise optical saturation (GSOS) microscopy²⁰ (**Supplementary Note 5**), providing a super-resolution FLIM image with preserved lifetime information and a $\sqrt{2}$ -fold increase in spatial resolution (**Fig. 1g**). We further acquired 3D super-resolution FLIM stacks by applying GSOS to pairs of diffraction limited (DL) instant FLIM stacks of a fixed Cx3cr1-GFP/+ mouse brain acquired with different excitation powers (**Supplementary Fig. 6, Supplementary**

Video 2). Structures in GSOS stacks are resolved with higher resolution in both maximized projections and 3D reconstructions compared to the ones in DL stacks.

The *in vivo* performance of instant FLIM is characterized by measuring the fluorescence lifetimes and phasor components of green fluorescence protein (GFP) expressed in living zebrafish and mice. Although GFP has stable fluorescence lifetimes²¹, lifetime changes can be observed when the intracellular microenvironments varies (e.g., temperature fluctuations²²). Before measuring GFP lifetime *in vivo*, we performed an *in vitro* instant FLIM experiment by imaging GFP expressed in living cells. To observe the changes in GFP lifetimes, we acquired instant FLIM images of MDA-MB-231-GFP cells under 18 different temperatures from 18.1 °C to 46.7 °C (**Supplementary Fig. 7**). While the intensity images show no clear distinctions under different temperatures, the fluorescence lifetimes decrease consistently as temperature increases. The changes are also visualized by using the phasor ROI or K-means clustering labeling techniques to segment the images based on their lifetime/phasor variations.

To test instant FLIM as an intravital modality we first imaged *Tg(pul:gfp)* zebrafish at 4 days post fertilization (dpf) using regulatory sequences of *pul* to express GFP in myeloid cells such as microglia and macrophages (**Fig. 2a**). We imaged neural regions where both CNS (central nervous system) and PNS (peripheral nervous system) myeloid cells could be detected and identifiable by their anatomical location. Lifetime measurements reported at least two distinct GFP lifetime profiles using the phasor approach (**Fig. 2b-e**). When examined as a phasor plot, PNS myeloid cells clustered distinctly compared to CNS myeloid cells (**Fig. 2b,c**). CNS myeloid cells also segregated into at least two distinct clusters by their *g* component, suggesting that lifetime can

report heterogeneity among CNS myeloid cells (**Fig. 2c, Supplementary Fig. 8**). We next asked if lifetime differences were present in distinct subdomains of individual CNS-located myeloid cells over time by collecting 3D stacks every 15 minutes for 4 hours. These experiments demonstrated that individual CNS-myeloid cells label with adjacent subdomains were distinguishable by lifetime differences. Temporal analysis of τ shows that individual subdomains of cells change over time as cells migrate (**Fig. 2f**). These changes largely occur within cellular subdomains as the average τ of the cell remains constant during homeostasis (**Fig. 2g**).

We further expanded the instant FLIM application to mouse model intravital imaging (**Fig. 2h, Supplementary Fig. 9**). Using Cx3cr1-GFP/+ adult mice with a thinned skull, we observed Cx3cr1-GFP+ adult microglia displayed dynamic and complex branching emanating from the cell body (**Fig. 2i, Supplementary Fig. 9**). Imaging depth was estimated to be ~130 μm , and when combined with adaptive optics^{17,23}, 3D FLIM stacks were generated up to ~300 μm deep in the brain (**Supplementary Fig. 10, Supplementary Video 3, Supplementary Note 6**). We measured g , s , and τ and compared these values between the cell bodies and protrusions. While we did not detect differences in g and s , surveilling protrusions displayed increased τ compared to the cell bodies, indicating that protrusions have a distinct fluorescence lifetime (**Fig. 2j, Supplementary Fig. 9**). We also employed 4D instant FLIM by taking 3D stacks of mouse microglia every two minutes. These images demonstrated that while microglia have dynamic processes, under homeostatic conditions the lifetimes of the cell bodies and surveilling protrusions are stable (**Fig. 2k,l**).

We next used instant FLIM to determine if we could detect potential lifetime changes that could occur in CNS, specifically injury-induced activation. To do this, we created lesions in *Tg(pul:gfp)* zebrafish with the mode-locked laser and created 4D instant FLIM movies of microglial response to the injury by collecting 3D stacks every 15 minutes for 12 hours (**Fig. 3a**). Consistent with an injury response, microglia migrated to the site of injury (**Fig. 3b**) and instant FLIM detected decrease in the s component of microglia after injury (**Fig. 3b-e, Supplementary Fig. 8, Supplementary Video 4**). In plotting average lifetimes of each microglia, pre-injury microglia clustered together (**Fig. 3c**). After 60 minutes, microglia lifetimes segregated into two clusters in opposite directions of lifetime change. This clustering continued after 60 minutes with few cells resembling pre-injury lifetimes (**Fig. 3c**). We next analyzed lifetime subdomains in individual microglia. After injury, microglia adjusted their lifetimes, as denoted by the increase of red subdomains in individual cells, with continuing changes through 75 minutes post-injury (mpi) (**Fig. 3f,g, Supplementary Fig. 8**), demonstrating instant FLIM's ability to detect changes *in vivo* after physiological challenge.

We next performed 4D instant FLIM in focal laser injury mouse model (**Fig. 3h**). Adult mice microglia are markedly more abundant than zebrafish larval microglia. Focal injuries in the adult mouse brain parenchyma induced an instantaneous response from the microglia where processes were extended toward the site of injury (**Supplementary Figs. 9,11, Supplementary Videos 5,6**). Adult mouse microglial processes surround the lesion site similar to the cloaking arrangement of macrophages in the PNS²⁴. Next, we measured the lifetime components of the cell bodies, responding protrusions, and protrusion tips over the course of injury, from 2 minutes before the injury (-2 mpi) to 22 minutes after the injury (22 mpi) (**Fig. 3i,j, Supplementary Fig. 9**). These

measurements did not detect differences in g , s , or τ from -2 mpi to 22 mpi but did detect changes in τ between each of the cellular domains. Further, we analyzed lifetime dynamics throughout the process of protrusion extension to cloak the injury site. These measurements indicated that τ in each subdomain of the microglia remained relatively stable (**Fig. 3k,l**). These data demonstrate the ability of instant FLIM to delineate lifetimes in diverse cellular domains in mouse brains.

We have demonstrated a novel instant FLIM system that allows super-resolution FLIM and addresses the challenges in speed, SNR, and implementation faced by conventional FLIM techniques. Besides the quantitative lifetime measurements and the convenient phasor-based image segmentation techniques (**Supplementary Fig. 12, Supplementary Videos 7,8**), instant FLIM also allows researchers to quickly identify fluorescence heterogeneity within tissues by qualitatively observing the composite lifetime images or their surface rendered plots (**Supplementary Fig. 13, Supplementary Video 9**). There are relative minor limitations to instant FLIM: (a) since instant FLIM is a fixed frequency domain approach, photon efficiency decreases with increasing fluorophore lifetime (**Supplementary Fig. 4**), and (b) the analog signal processing RF components could be vulnerable to electromagnetic interference. In conclusion, we present instant FLIM as a powerful tool for long-term 4D *in vivo* FLIM with a wide application in intravital imaging. Due to its easy implementation and open-source software (**Supplementary Fig. 14**), instant FLIM will enable future biological discoveries in a wide variety of disciplines.

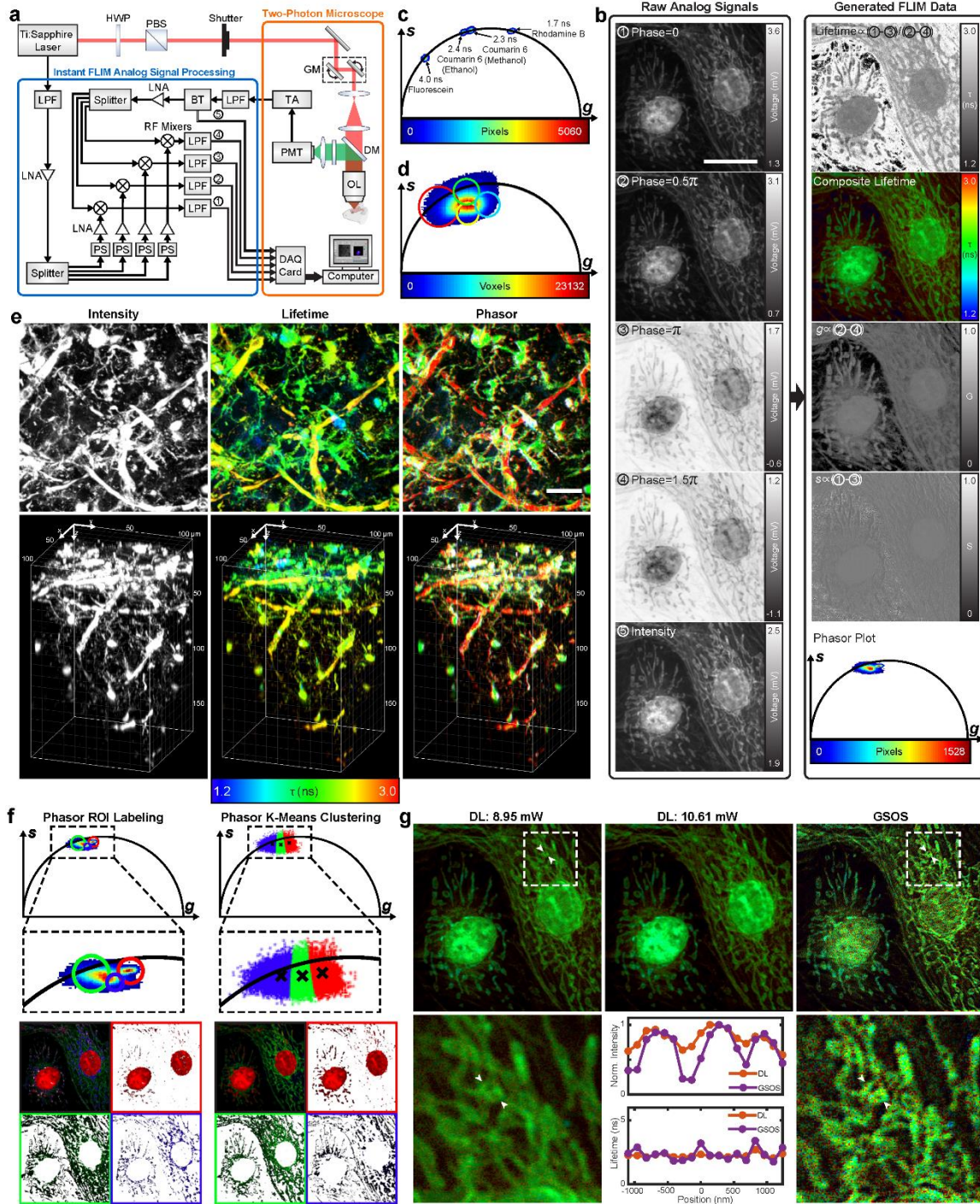


Figure 1

Instant fluorescence lifetime imaging microscopy. (a) Diagram of the instant FLIM system. Excitation (red) is controlled by a half-wave plate (HWP), a polarizing beam splitter (PBS), and a mechanical shutter. The components inside the orange box are the essential parts of a conventional

two-photon microscope: the pivot point of the galvanometer mirrors (GM) is conjugated with the back aperture of the objective lens (OL); fluorescence (green) is collected by the OL, reflected by the dichroic mirror (DM), and projected to the photomultiplier tube (PMT); conventionally, the output current of the PMT is converted to voltage by a transimpedance amplifier (TA) and digitized by a data acquisition (DAQ) card connected to a computer. Instant FLIM upgrades the conventional two-photon microscope by introducing the analog signal processing units enclosed in the blue box: the PMT signal is filtered by a low pass filter (LPF) and separated to RF and DC parts by a bias tee (BT); the RF part is amplified by a low-noise amplifier (LNA), split to four ways, and mixed with the reference signal from the femtosecond laser, which is also split to four ways but with different phases introduced by the phase shifters (PS); the filtered mixed signals from the four RF mixers ((1)-(4)) and the DC part of the PMT signal ((5)) are then simultaneously digitized by the DAQ card. (b) Left, raw analog signals ((1)-(5)) simultaneously acquired by the DAQ card while imaging fixed BPAE cells. Right, raw lifetime images (pixel value as lifetime), composite lifetime images (pixel brightness as intensity, hue as lifetime), phasor components (g and s), and phasor plots can be generated from the raw analog signals ((1)-(5)) instantaneously through basic matrix operations. (c) Phasor plot of four fluorescence lifetime standards acquired with instant FLIM confirming the accuracy of the system: the phasors of these single-lifetime fluorophores all locate on the universal semicircle, and their lifetime measurements match the expected values. (d) Phasor plot of a fixed Cx3cr1-GFP/+ mouse brain measured with instant FLIM, where four ROIs are drawn to label different cellular structures in the phasor ROI-labeled stack in (e). (e) Maximized z-projections (top) and 3D reconstructions (bottom) of the intensity, composite lifetime, and phasor ROI-labeled stacks of the fixed mouse brain identical to (d). (f) Phasor plot can be either manually grouped by ROIs (left) or automatically segmented using the

K-means clustering algorithm (right). Both techniques can segment the raw image by labeling the corresponding pixels with the colors of the ROIs/clusters (bottom). (g) Super-resolution FLIM by combining two-step GSOS with instant FLIM measurements. Top, super-resolution lifetime image of GSOS is obtained by linear combining two diffraction limited (DL) instant FLIM images of the fixed BPAE cells acquired with different excitation powers. Bottom, magnified views of the regions outlined with the white dashed boxes. Middle, line profiles of the normalized intensity and lifetime values at the positions of the white arrowheads for DL and GSOS images. Scale bars, 20 μm .

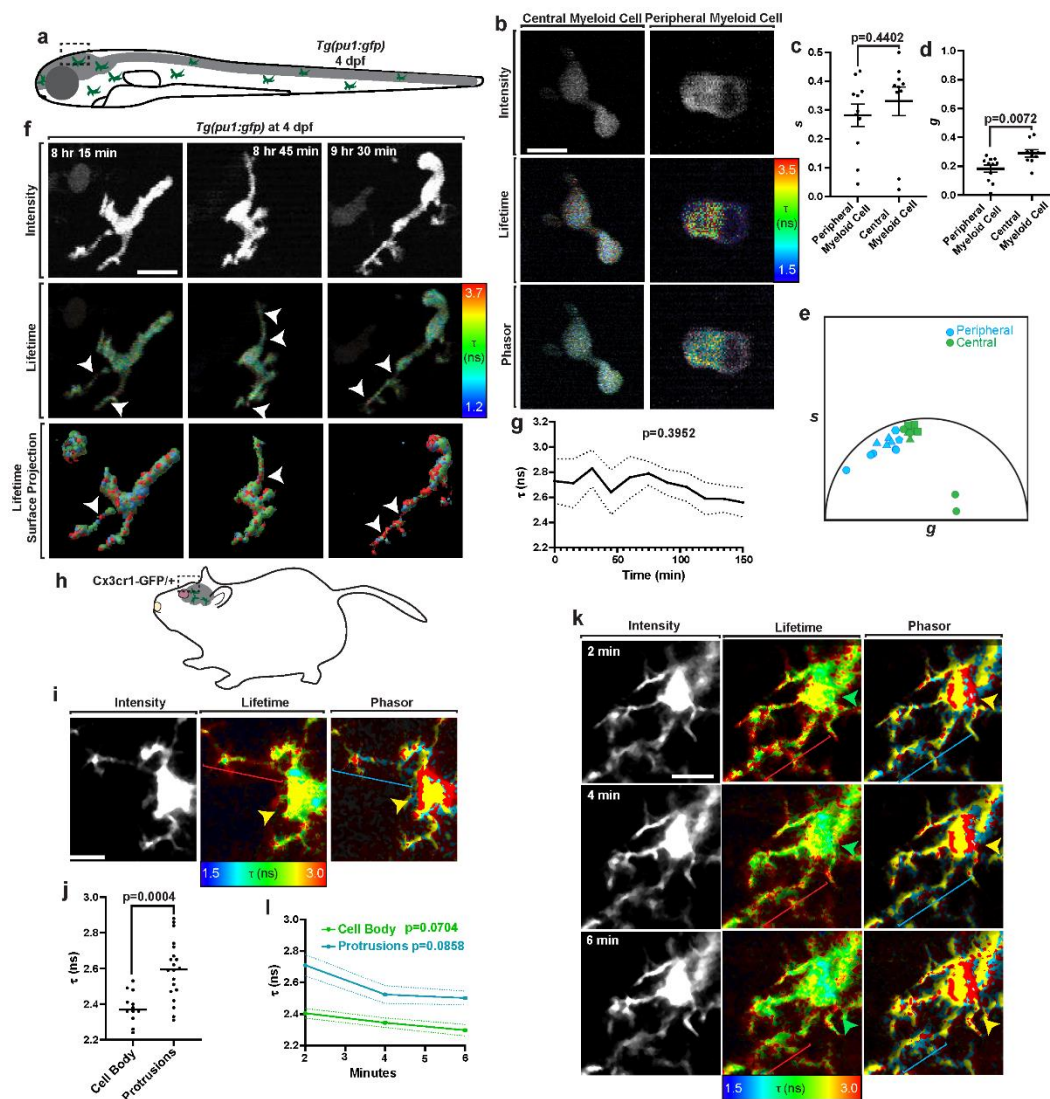


Figure 2

Fluorescence lifetime of microglia in homeostatic states. (a) Schematic of zebrafish paradigm. Larval *Tg(pu1:gfp)* zebrafish at 4 dpf were imaged using instant FLIM. (b) Instant FLIM images of *Tg(pu1:gfp)* zebrafish at 4 dpf of CNS-located and PNS-located myeloid cells. The top images represent fluorescent intensity, the middle images represent fluorescence lifetime, and the bottom images are labeled with phasor ROIs. (c-d) Graph of average s (c) and g (d) lifetime components in CNS-located ($n=10$ cells) and PNS-located ($n=11$ cells) myeloid cells. CNS-located cells have a larger g lifetime component. (e) Plot representing the phasor locations of CNS-located (green) and PNS-located (blue) myeloid cells. (f) Time-lapse FLIM images of *Tg(pu1:gfp)* at 4 dpf at 8 hr 15 min, 8 hr 45 min, and 9 hr 30 min. Rows show Intensity, Lifetime, Phasor, and Lifetime Surface Projection. (g) Plot of lifetime component τ (ns) vs Time (min) for a single cell, showing a decrease from ~2.8 ns to ~2.6 ns over 150 minutes. (h) Schematic of a zebrafish larva with *Cx3cr1-GFP+* cells in the CNS. (i) FLIM images of *Cx3cr1-GFP+* cells showing Intensity, Lifetime, and Phasor. (j) Plot of lifetime component τ (ns) for Cell Body and Protrusions, showing a significant difference ($p=0.0004$). (k) Time-lapse FLIM images at 2, 4, and 6 minutes showing Intensity, Lifetime, and Phasor. (l) Plot of lifetime component τ (ns) vs Minutes for Cell Body (green) and Protrusions (blue), showing a decrease over time ($p=0.0704$ for Cell Body, $p=0.0858$ for Protrusions).

and PNS-located (blue) by their s and g components. Each shape represents a measurement taken from different individual animals. (f) Maximum projections from a 12-hour instant FLIM time-lapse movie of a microglia. The top images represent fluorescent intensity, the middle images represent fluorescence lifetime, and the bottom images surface representations of lifetime subdomains within the cell. White arrowheads denote cellular subdomains with increased lifetimes. (g) Average τ of single microglia over 100 minutes. $n=8$ cells. (h) Schematic of mouse paradigm. Cx3cr1-GFP/+ mice were imaged using instant FLIM. (i) Instant FLIM images of a Cx3cr1 mouse microglia. The left image represents fluorescent intensity, the middle image represents fluorescence lifetime, and the right image is labeled with phasor ROIs. Brackets denote microglia protrusion, and arrowheads denote cell bodies. Colors represent approximate lifetime or phasor pseudo-coloring. (j) Graph of τ in cell bodies and protrusions. $n=12$ cell bodies, $n=20$ protrusions. (k) 4D instant FLIM images of a Cx3cr1 mouse microglia. The left images represent fluorescent intensity, the middle images represent fluorescence lifetime, and the right images are labeled with phasor ROIs. Brackets denote microglia protrusion, and arrowheads denote cell bodies. Colors represent approximate lifetime or phasor pseudo-coloring. (l) Average τ of microglial cell bodies (green) and protrusions (blue) over 3 minutes. $n=3$ cells. Scale bar, $10\mu\text{m}$. (c,d,j) use a two-sided Student's t -test. (g,l) use one-way ANOVAs.

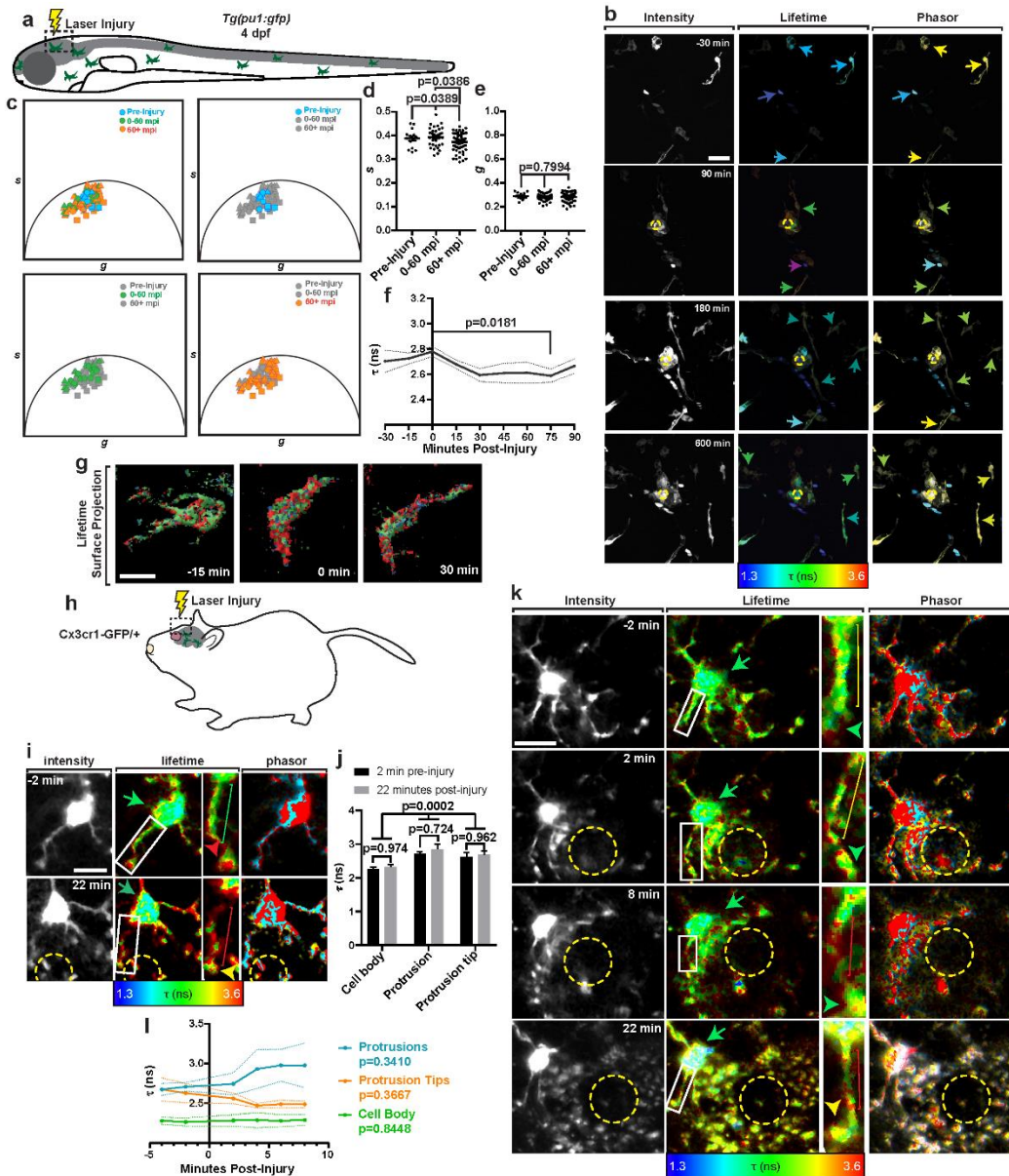


Figure 3

Fluorescence lifetime of microglia following laser injury. (a) Schematic of zebrafish paradigm. Larval *Tg(pu1:gfp)* zebrafish at 4 dpf were imaged using instant FLIM following an injury by a two-photon laser. (b) Instant FLIM images of *Tg(pu1:gfp)* zebrafish at 4 dpf of microglia from a 12-hour time-lapse movie before and after laser injury. The left images represent fluorescent intensity, the middle images represent fluorescence lifetime, and the right images are labeled with phasor ROIs. Dashed yellow circle denotes the lesion site. Arrows denote approximate lifetime

and phasor pseudo-coloring. (c) Plot representing the phasor locations of microglia before laser injury (blue), 0-60 minutes post injury (green), and 60+ mpi (orange) by their s and g components. Each shape represents a measurement taken from different individual animals. (d-e) Graph of average s (d) and g (e) lifetime components in microglia before injury ($n=15$ cells), 0-60 mpi ($n=33$ cells), and 60+ mpi ($n=62$). (f) Average τ of single microglia before and after laser injury. $n=9$ cells. (g) Surface representation of changing lifetime subdomains within single microglia before and after injury. (h) Schematic of mouse paradigm. Cx3cr1-GFP/+ mice were imaged using instant FLIM following an injury by a two-photon laser. (i) Instant FLIM images of a Cx3cr1-GFP/+ mice 2 minutes before and 22 minutes after laser injury. Left images represent fluorescent intensity, middle images represent fluorescence lifetime, and right images are labeled with phasor ROIs. Dashed yellow circle denotes the lesion site. Arrows denote cell body, brackets denote protrusions, and arrowheads denote protrusion tips. Colors denote approximate lifetime and phasor pseudo-coloring. White box denotes inset shown in middle right. (j) Graph of τ in cell bodies, protrusions, and protrusion tips 2 minutes before and 22 minutes after injury. $n=5$ cell bodies, $n=5$ protrusions, $n=5$ protrusion tips. (k) Instant FLIM images of a Cx3cr1-GFP/+ mice from a 30-minute time-lapse before and after laser injury. Left images represent fluorescent intensity, middle images represent fluorescence lifetime, and right images are labeled with phasor ROIs. Dashed yellow circle denotes the lesion site. Arrows denote cell body, brackets denote protrusions, and arrowheads denote protrusion tips. Colors denote approximate lifetime and phasor pseudo-coloring. White box denotes inset shown in middle right. (l) Average τ of cell bodies, protrusions, and protrusion tips before and after laser injury. $n=5$ cell bodies, $n=5$ protrusions, $n=5$ protrusion tips. Scale bar, 10 μ m. (d-f) use a Tukey's HSD test. (j) uses a two-way ANOVA with multiple comparisons. (l) uses a one-way ANOVA.

Acknowledgements

This work was supported by the University of Notre Dame, the Center for Zebrafish Research and Center of Stem Cells and Regenerative Medicine at the University of Notre Dame, the National Science Foundation under Grant No. CBET-1554516 (S.S.H.), the National Institutes of Health R01 CA194697, R01 CA222405 (S.Z.), R01 NS107553 (C.J.S), the Elizabeth and Michael Gallagher Family (C.J.S.), the Alfred P. Sloan Foundation (C.J.S.), and the Berry Family Foundation Graduate Fellowship of Advanced Diagnostics & Therapeutics (AD&T) (Y.Z.).

Author contributions

Y.Z. and S.S.H. conceived and coordinated the project, designed and built the microscope, wrote the control and image-processing software, and performed the imaging experiments. I.H.G. and S.Z. performed the mice surgery, acquired the images, and analyzed the data. E.L.N. and C.J.S. prepared the zebrafish, performed the zebrafish imaging experiments, and analyzed the data. D.B. assisted with the microscope assembly and performed the temperature-dependent imaging experiment. S.S.H., S.Z., and C.J.S. supervised the study. All authors contributed to the writing and editing of the manuscript.

Competing interests

The authors declare no competing financial interests.

Additional information

Supplementary information is available for the paper at XXXXXXXXX.

Correspondence and requests for materials should be addressed to S.S.H.

Methods

Experimental setup and analog signal processing

We implemented the instant FLIM system based on a custom-built two-photon microscope (**Fig. 1a, Supplementary Fig. 1**). The intensity of a mode-locked Ti:sapphire laser (Spectra Physics Mai Tai BB, 710-990 nm, 100 fs, 80 MHz) is controlled by a neutral density filter (NDF), a motorized half-wave plate, and a polarizing beam splitter (PBS). A power meter is used to measure the excitation power by monitoring a small fraction of the laser beam reflected by a glass slide. A mechanical shutter (Thorlabs SHB1T) is used to block the laser beam when no imaging acquisition takes place. A sensorless adaptive optics (AO) setup consisting of a deformable mirror (Thorlabs DMP40-P01), a beam expander composed of two achromatic doublets (Thorlabs AC254-030-B, AC254-075-B), an achromatic quarter-wave plate (Thorlabs AQWP05M-980) and another PBS is utilized to correct the wavefront of the excitation beam in order to improve the imaging depth (**Supplementary Fig. 10, Supplementary Note 6**). The AO setup is optional and can be switched into and out of the optical path using a folding mirror. The laser beam is directed to a conventional two-photon microscopy setup consisting of a pair of galvo scanners (Thorlabs GVS002), a scan lens (Thorlabs AC254-040-B), a tube lens (Thorlabs AC254-200-B), an objective lens (Nikon CFI APO NIR, 40x, 0.8 NA, or Olympus XLPLN25XWMP2, 25x, 1.05 NA), and a motorized stage (Prior OptiScan III). A long pass filter is used to block ambient light from entering the objective. The 2PEF is epi-collected by the objective lens, reflected by a dichroic mirror, filtered through a set of bandpass and short pass filters to eliminate residual excitation, and detected by a PMT (Hamamatsu H7422PA-40) through a collection lens. The current signal from the PMT is amplified and converted to a voltage signal by a transimpedance amplifier (Aricorp DC-100).

The analog signal processing module in instant FLIM utilizes the fluorescence signal from the PMT and the 80 MHz reference signal from the Ti:sapphire laser to generate the intensity, lifetime, and phasor data simultaneously. As shown in **Supplementary Fig. 2**, the PMT signal is filtered by a low pass filter (LPF) (Mini-Circuits BLP-90+) and separated into DC and RF parts by a bias tee (Mini-Circuits ZFBT-282-1.5A+). The DC signal (V_{DC}) is acquired by a data acquisition (DAQ) card (National Instruments PCIe-6323) to reconstruct the intensity image. The RF signal is amplified by a low-noise amplifier (LNA) (Mini-Circuits ZX60-P103LN+) and split to four paths by a 4-way power splitter (Mini-Circuits ZSC-4-3+). Meanwhile, the 80 MHz reference signal from the laser, $v_{ref}(t)$, is filtered by an LPF to eliminate higher harmonics, amplified by an LNA, and split to four signal paths, $v_{80MHz}(t)$, also by a power splitter. A phase shift is introduced to each reference signal path by a pair of phase shifters (Mini-Circuits JSPHS-150 with TB-152+). Note that each phase shifter can introduce a phase shift within π to the 80 MHz signal; connecting them in series introduces a total phase shift within 2π for each path. The phase shifts are independently controlled by the bias voltages generated by the DAQ card. The four phase shifted reference signals are then amplified by LNAs and directed to four RF mixers (Mini-Circuits ZAD-3H+). Each mixer takes a reference signal path, $v_{LO}(t, \varphi)$, to its local oscillator (LO) port and a PMT signal path, $v_{RF}(t)$, to its RF port and generates a mixed signal, $v_{IF}(t, \varphi)$, on its intermediate frequency (IF) port. The analog mixing processes are performed simultaneously during each measurement; therefore, no additional acquisition time compared to conventional two-photon intensity measurement is required in instant FLIM. The IF signals from each mixer are then filtered to DC, i.e., $V_{IF}(\varphi)$, by an LPF (Thorlabs EF502) and measured by another DAQ card (National Instruments PCI-6110). In the end, for each intensity image (2D, 3D, or 4D) acquired, four

corresponding mixer images will be acquired simultaneously. Fluorescence lifetime images as well as phasor plots will then be instantaneously generated through basic matrix operations. The DAQ cards are also used to control the motorized half-wave plate, the shutter, and the galvo mirrors during the imaging process. The motorized stage and the deformable mirror, on the other hand, are controlled directly by the computer through USB ports.

The parts and price list for the implementation of an instant FLIM system is presented in **Supplementary Table 1**. The total cost to upgrade an existing two-photon microscope to an instant FLIM system is less than \$2,500.

Simultaneous generation of intensity, lifetime, and phasor data

With the multiplexing phase shift and analog mixing in instant FLIM, the fluorescence intensity, lifetime, and phasor data can be acquired simultaneously (**Fig. 1b, Supplementary Notes 1-2**). Specifically, the 2PEF intensity image is generated from the DC part of the PMT signal:

$$V_{\text{DC}} = \frac{BP^2c}{T} + O_B, \quad (1)$$

where P is the excitation power, c is the fluorophore concentration, T is the modulation period of the Ti:sapphire laser, B and O_B are the conversion loss and offset from the bias tee's RF&DC to DC ports, respectively. The lifetime and phasor data, on the other hand, are obtained by applying basic mathematical operations on the outputs of the four mixers' IF ports:

$$V_{\text{IF}}(\varphi) = \frac{MP^2c}{T} \sum_i a_i \frac{1}{1 + \tau_i \omega} [\sin(\varphi) + \tau_i \omega \cos(\varphi)] + O_M, \quad (2)$$

where φ is the phase shift introduced by the phase shifters, a_i is the intensity-weighted fractional contribution of the fluorophore with lifetime τ_i ($\sum_i a_i = 1$), ω is the angular modulation frequency, M and O_M are the conversion loss and offset from the mixer's RF to IF ports, respectively. The average (phase¹) lifetime image is calculated as

$$\bar{\tau} = \frac{1}{\omega} \frac{V_{\text{IF}}(0) - V_{\text{IF}}(\pi)}{V_{\text{IF}}(0.5\pi) - V_{\text{IF}}(1.5\pi)}, \quad (3)$$

and the components of the phasors are obtained as

$$\begin{aligned} g &= \frac{B}{2M} \frac{V_{\text{IF}}(0.5\pi) - V_{\text{IF}}(1.5\pi)}{V_{\text{DC}} - O_B} = \sum_i a_i \frac{1}{1 + (\tau_i \omega)^2}, \\ s &= \frac{B}{2M} \frac{V_{\text{IF}}(0) - V_{\text{IF}}(\pi)}{V_{\text{DC}} - O_B} = \sum_i a_i \frac{\tau_i \omega}{1 + (\tau_i \omega)^2}, \end{aligned} \quad (4)$$

where M/B and O_B are calibrated before measurements using the procedures in **Supplementary Note 3**. With the same instant FLIM setup, super-resolution fluorescence lifetime images can be acquired based on the principle of GSOS²⁰ (**Fig. 1g, Supplementary Fig. 6, Supplementary Video 2, Supplementary Note 5**).

Image reconstruction and analysis

All image reconstruction and analysis were performed with the open-source Instant-FLIM-Control and Instant-FLIM-Analysis (**Supplementary Fig. 14, Supplementary Protocols 1,2**) software provided in this work. Additional image processing and visualization were performed using ImageJ (US National Institutes of Health), Matlab (MathWorks), Imaris (Bitplane), or Illustrator (Adobe) software.

The raw intensity [equation (1)], g and s [equation (4)] images from 2D, 3D, and 4D instant FLIM measurements were exported as 32-bit TIF files using the Instant-FLIM-Control program. Whereas the program allows the export of additional FLIM data, to reduce the consumption of the computer's storage space, we exported only the raw intensity, g and s images, which can be used to reconstruct other types of FLIM data. We used the "Correct 3D Drift" ImageJ plugin²⁵ to register the 4D raw images to correct for the sample drift during time-lapse measurements. To perform the image registration simultaneously on the three raw images, we created a color image by merging the raw intensity, g and s images as its red, green, and blue channels, respectively; then, as the 3D image registration was performed on the red (intensity) channel, the other channels were registered simultaneously. The registered image was cropped to remove the empty voxels generated from the registration process, and its channels were split into three separate images, which correspond to the registered intensity, g and s images.

The intensity, g and s images were then imported to the Instant-FLIM-Analysis program to generate other types of FLIM data. Since the raw FLIM data usually have a low SNR⁹, we provided an filtering option in the program, such that one could applied a median filter (3×3 or 5×5 kernels) or smoothing filter on the raw images, one or multiple times, to increase the SNR; note that applying a median filter to the phasor images does not decrease the image resolution¹⁶. In this work, we applied a 3×3 median filter three times on the raw phasor images for all *in vivo* measurements. The program could also uniformly scale the g and s images by a constant ratio to effectively zoom-in or zoom-out the phasor plot while keeping the calculated lifetime unaltered; a ratio between 0.7 to 1.0 was used in our measurements to post-compensate for the inaccuracy in system calibration and make sure that the majority of the phasor points fall inside the universal

semicircle $[(g - 0.5)^2 + s^2 = 0.25]$. We then generated the phasor plot from the pre-processed g and s images. The phasor plot was a 2D histogram of the phasor components, g and s , where the magnitude (represented with a color map) of each grid (with pre-defined size) in the 2D histogram represented the number of phasor points located inside that grid. To perform the phasor analysis, the program allowed the user to either (1) manually draw ROIs on the phasor plot and label the pixels corresponding to the phasor points enclosed with the ROIs with different colors¹⁶, or (2) automatically segment the phasors into K clusters using the K-means clustering algorithm and label the pixels corresponding to the phasor clusters with different colors¹⁹; both labeling techniques could segment the raw image into structures with different lifetime/phasor characteristics (**Fig. 1f**). After the analysis described above, the raw lifetime image (gray-scale image with pixel value as lifetime), composite lifetime image (RGB image with pixel brightness as intensity, hue as lifetime), phasor plot (RGB image), and segmented images based on phasor ROIs or K-means clustering (RGB image) were generated and exported as 32-bit TIF files. For 3D images, the TIF files were imported into ImageJ and the maximized z-projections of the stacks were generated. For 4D measurements, the stacks were first converted to hyperstacks in ImageJ to facilitate the time-lapse analysis, and a time-lapse maximized z-projection sequence could be generated. We also used Imaris to visualize the 3D and 4D stacks (**Fig. 1e, Supplementary Figs. 6,10, Supplementary Videos 3,4,5,7,8**) and enhance the qualitative information of FLIM by surface rendering the composite lifetime images (**Supplementary Fig. 13, Supplementary Video 9**).

To quantify the results of *in vivo* instant FLIM measurements (**Figs. 2,3, Supplementary Figs. 8,9**), we extracted the raw lifetime as well as g and s values from the TIF files exported by

the Instant-FLIM-Analysis program. Specifically, the files were opened in ImageJ, a single-plane ROI was drawn around the cell of interest and the mean value was measured within that ROI. The plots representing the phasor locations of cells were generated using Illustrator. Using the Instant-FLIM-Analysis program, ROIs were drawn on the phasor plots to correspond with the pixels representing individual cells. Individual ROIs were drawn for each cell analyzed. The locations for each of these ROIs were then recapitulated on the comprehensive plot. These specific locations were determined by exporting each phasor plot with the drawn ROIs and determining the coordinates of the ROIs within the exported phasor plot image using ImageJ. The coordinates were then used to place representations of each cell in the proper location on the comprehensive plot in Illustrator.

Animal procedures and sample preparation

All animal studies were conducted in accordance with the University of Notre Dame Institutional Animal Care and Use Committee guidance. The acquisition parameters for all the images shown in this work are presented in **Supplementary Table 2**.

Transgenic mice

Intravital imaging of the mouse brain was performed similarly to previously described²⁶. Briefly, Cx3cr1-GFP/+ mice (generated in-house by crossing Cx3cr1-GFP/GFP mice with wildtype C57Bl/6 mice) were anesthetized with ketamine and xylazine cocktail by intraperitoneal injection. The mouse's head was secured and fixed in place using a stereotaxic instrument (Stoelting Co), and the skull was exposed with a midline scalp incision. A high-speed microdrill (Ideal Microdrill) equipped with a 0.7 mm burr (Fine Science Tools, 19007-09) was used to thin the skull to

approximately 30 μm in thickness, using light sweeping motions to thin the skull gradually without applying significant pressure to the brain. In some instances, dental cement was used to border the thinned skull to form a bowl-like barrier to help contain water for imaging. Following surgery, the anaesthetized mouse was administered a retro-orbital injection of 70 kDa Texas Red-Dextran (Invitrogen D1864) to enable fluorescent detection of blood vessels. The mouse was placed on the stage for imaging and was monitored periodically to ensure that it was fully anesthetized and not under duress. Additional doses of ketamine and xylazine cocktail on an as-needed basis.

Transgenic zebrafish

The transgenic zebrafish line used in this study was *Tg(pu1:gfp)*. All embryos were generated from pairwise matings and raised at 28 °C until imaging. Stable, germline transgenic zebrafish were used for all experiments. Embryos of either sex were used for all experiments. At 4 dpf, the embryos were dechorionated and anesthetized with 3-amino-benzoic acid ester. After anesthetization, embryos were mounted on their ventral side in 0.8% low-melting point agarose in 35 mm Petri dishes with glass bottoms. Following mounting, the embryos were imaged using the instant FLIM system described above.

Fixed mouse brain

To prepare a fixed brain to image for select experiments, a living Cx3cr1-GFP/+ mouse was first deeply anesthetized with isoflurane. Next, the mouse's chest cavity was opened to expose the heart, and the mouse was provided with a 100 μL injection of fixable Dextran 594 directly into the heart. After allowing the dextran to circulate for 1 minute, the mouse was perfused with 10 mL ice-cold

4% PFA to thoroughly fix the brain. Subsequently, the brain was extracted and fixed in 4% PFA overnight at 4 °C, and washed in 1x PBS, after which point it was ready for imaging.

Live MDA-MB-231-EGFP cells

Prior to imaging (**Supplementary Fig. 7**), MDA-MB-231-EGFP cells were cultured in DMEM High Glucose supplemented with 10% FBS and 1% Penicillin-Streptomycin in an incubator at 37 °C, 5% CO₂. Cells were grown to ~80% confluence for the imaging experiments. During imaging, refrigerated or heated culture media were added to the cell culture to change the microenvironment temperature, which was simultaneously monitored by a thermometer placed in the media.

Fixed BPAE cells

FluoCells prepared slide #1 (Invitrogen F36924) was used as a biological test slide to evaluate the performance of the instant FLIM system (**Fig. 1b,f,g**). This test slide contained bovine pulmonary artery endothelial (BPAE) cells labeled with multiple fluorescent dyes: the mitochondria were stained with MitoTracker Red CMXRos, the F-actin was labeled with Alexa Fluor 488 phalloidin, and the nuclei were labeled with DAPI.

Lifetime standards and fluorophore mixtures

Four lifetime standards, i.e., fluorophore solutions with known fluorescence lifetimes, were prepared as previously described^{27,28}: 1 mM coumarin 6 in methanol (2.3 ns at 20 °C), 1 mM coumarin 6 in ethanol (2.4 ns at 20 °C), 1mM fluorescein in 0.1 M NaOH (4.0 ns at 20 °C), and 1 mM rhodamine B in water (1.7 ns at 20 °C) (**Supplementary Fig. 5**). To prepare the standards, the coumarin 6 (Sigma-Aldrich 546283) was dissolved in methanol (VWR BDH2029) and ethanol

(Millipore 818760), respectively; the fluorescein (Sigma-Aldrich F245-6) was dissolved in NaOH 1.0N in aqueous solution (VWR BDH7222); and the rhodamine B (Alfa Aesar A13572) was dissolved in water. The fluorophore mixtures were acquired by mixing the fluorescein and rhodamine B lifetime standards described above with different mole ratios.

Reporting summary

Further information on research design is available in the Nature Research Reporting Summary linked to this article.

Data availability

All data generated in this manuscript are present in the figures and supplemental figures. Data is available upon request.

Code availability

The repositories of the open-source Instant-FLIM-Control (<https://github.com/yzhang34/Instant-FLIM-Control.git>) and Instant-FLIM-Analysis (<https://github.com/yzhang34/Instant-FLIM-Analysis.git>) software are hosted on GitHub and they are freely available for academic use.

References

1. Lichtman, J. W. & Conchello, J.-A. Fluorescence microscopy. *Nat. Methods* **2**, 910–919 (2005).
2. Denk, W., Strickler, J. & Webb, W. Two-photon laser scanning fluorescence microscopy. *Science* (80-.). **248**, 73–76 (1990).
3. Zipfel, W. R., Williams, R. M. & Webb, W. W. Nonlinear magic: multiphoton microscopy in the biosciences. *Nat. Biotechnol.* **21**, 1369–1377 (2003).
4. Sakadžić, S. *et al.* Two-photon high-resolution measurement of partial pressure of oxygen in cerebral vasculature and tissue. *Nat. Methods* **7**, 755–759 (2010).
5. Howard, S. S., Straub, A., Horton, N. G., Kobat, D. & Xu, C. Frequency-multiplexed in vivo multiphoton phosphorescence lifetime microscopy. *Nat. Photonics* **7**, 33–37 (2012).
6. Philip, J. & Carlsson, K. Theoretical investigation of the signal-to-noise ratio in fluorescence lifetime imaging. *Journal of the Optical Society of America A* vol. 20 368–379 (2003).
7. Booth, M. J. & Wilson, T. Low-cost, frequency-domain, fluorescence lifetime confocal microscopy. *J. Microsc.* **214**, 36–42 (2004).
8. Colyer, R. A., Lee, C. & Gratton, E. A novel fluorescence lifetime imaging system that optimizes photon efficiency. *Microsc. Res. Tech.* **71**, 201–213 (2008).
9. Zhang, Y., Khan, A. A., Vigil, G. D. & Howard, S. S. Investigation of signal-to-noise ratio in frequency-domain multiphoton fluorescence lifetime imaging microscopy. *J. Opt. Soc. Am. A* **33**, B1 (2016).
10. Ryu, J. *et al.* Real-time visualization of two-photon fluorescence lifetime imaging microscopy using a wavelength-tunable femtosecond pulsed laser. *Biomed. Opt. Express* **9**,

- 3449 (2018).
11. Bower, A. J. *et al.* High-speed imaging of transient metabolic dynamics using two-photon fluorescence lifetime imaging microscopy. *Optica* **5**, 1290 (2018).
 12. Becker, W. *et al.* Fluorescence lifetime imaging by time-correlated single-photon counting. *Microsc. Res. Tech.* **63**, 58–66 (2004).
 13. So, P. T. C., French, T., Yu, W. M., Berland, K. M. & Dong, C. Y. Time-resolved fluorescence microscopy using two-photon excitation. *Bioimaging* **3**, 49–63 (1995).
 14. Raspe, M. *et al.* siFLIM: single-image frequency-domain FLIM provides fast and photon-efficient lifetime data. *Nat. Methods* **13**, 501–504 (2016).
 15. Helmchen, F. & Denk, W. Deep tissue two-photon microscopy. *Nat. Methods* **2**, 932–940 (2005).
 16. Ranjit, S., Malacrida, L., Jameson, D. M. & Gratton, E. Fit-free analysis of fluorescence lifetime imaging data using the phasor approach. *Nat. Protoc.* **13**, 1979–2004 (2018).
 17. Zhang, Y. *et al.* Three-dimensional deep tissue multiphoton frequency-domain fluorescence lifetime imaging microscopy via phase multiplexing and adaptive optics. in *Multiphoton Microscopy in the Biomedical Sciences XIX* (eds. Periasamy, A., So, P. T. & König, K.) 86 (SPIE, 2019). doi:10.1117/12.2510674.
 18. Sun, Y., Day, R. N. & Periasamy, A. Investigating protein-protein interactions in living cells using fluorescence lifetime imaging microscopy. *Nat. Protoc.* **6**, 1324–1340 (2011).
 19. Zhang, Y. *et al.* Automatic segmentation of intravital fluorescence microscopy images by K-means clustering of FLIM phasors. *Opt. Lett.* **44**, 3928–3931 (2019).
 20. Zhang, Y., Benirschke, D., Abdalsalam, O. & Howard, S. S. Generalized stepwise optical saturation enables super-resolution fluorescence lifetime imaging microscopy. *Biomed.*

- Opt. Express* **9**, 4077 (2018).
21. Jakobs, S., Subramaniam, V., Schönle, A., Jovin, T. M. & Hell, S. W. EGFP and DsRed expressing cultures of Escherichia coli imaged by confocal, two-photon and fluorescence lifetime microscopy. *FEBS Lett.* **479**, 131–135 (2000).
 22. Gohar, A. V. *et al.* Subcellular localization-dependent changes in EGFP fluorescence lifetime measured by time-resolved flow cytometry. *Biomed. Opt. Express* **4**, 1390 (2013).
 23. Ji, N. Adaptive optical fluorescence microscopy. *Nat. Methods* **14**, 374–380 (2017).
 24. Uderhardt, S., Martins, A. J., Tsang, J. S., Lämmermann, T. & Germain, R. N. Resident Macrophages Cloak Tissue Microlesions to Prevent Neutrophil-Driven Inflammatory Damage. *Cell* **177**, 541-555.e17 (2019).
 25. Parslow, A., Cardona, A. & Bryson-Richardson, R. J. Sample Drift Correction Following 4D Confocal Time-lapse Imaging. *J. Vis. Exp.* 1–4 (2014) doi:10.3791/51086.
 26. Grutzendler, J., Kasthuri, N. & Gan, W.-B. Long-term dendritic spine stability in the adult cortex. *Nature* **420**, 812–816 (2002).
 27. Boens, N. *et al.* Fluorescence Lifetime Standards for Time and Frequency Domain Fluorescence Spectroscopy. *Anal. Chem.* **79**, 2137–2149 (2007).
 28. Kristoffersen, A. S., Erga, S. R., Hamre, B. & Frette, Ø. Testing Fluorescence Lifetime Standards using Two-Photon Excitation and Time-Domain Instrumentation: Rhodamine B, Coumarin 6 and Lucifer Yellow. *J. Fluoresc.* **24**, 1015–1024 (2014).

Supplementary Materials

Instant FLIM enables 4D *in vivo* lifetime imaging of intact brains

Yide Zhang^{1,6}, Ian H. Guldner^{2,4,5}, Evan L. Nichols^{2,3}, David Benirschke¹,

Cody J. Smith^{2,3}, Siyuan Zhang^{2,4,5} & Scott S. Howard^{1,4*}

¹*Department of Electrical Engineering, University of Notre Dame, Notre Dame, IN, USA*

²*Department of Biological Sciences, University of Notre Dame, Notre Dame, IN, USA*

³*Center for Stem Cells and Regenerative Medicine, University of Notre Dame, IN, USA*

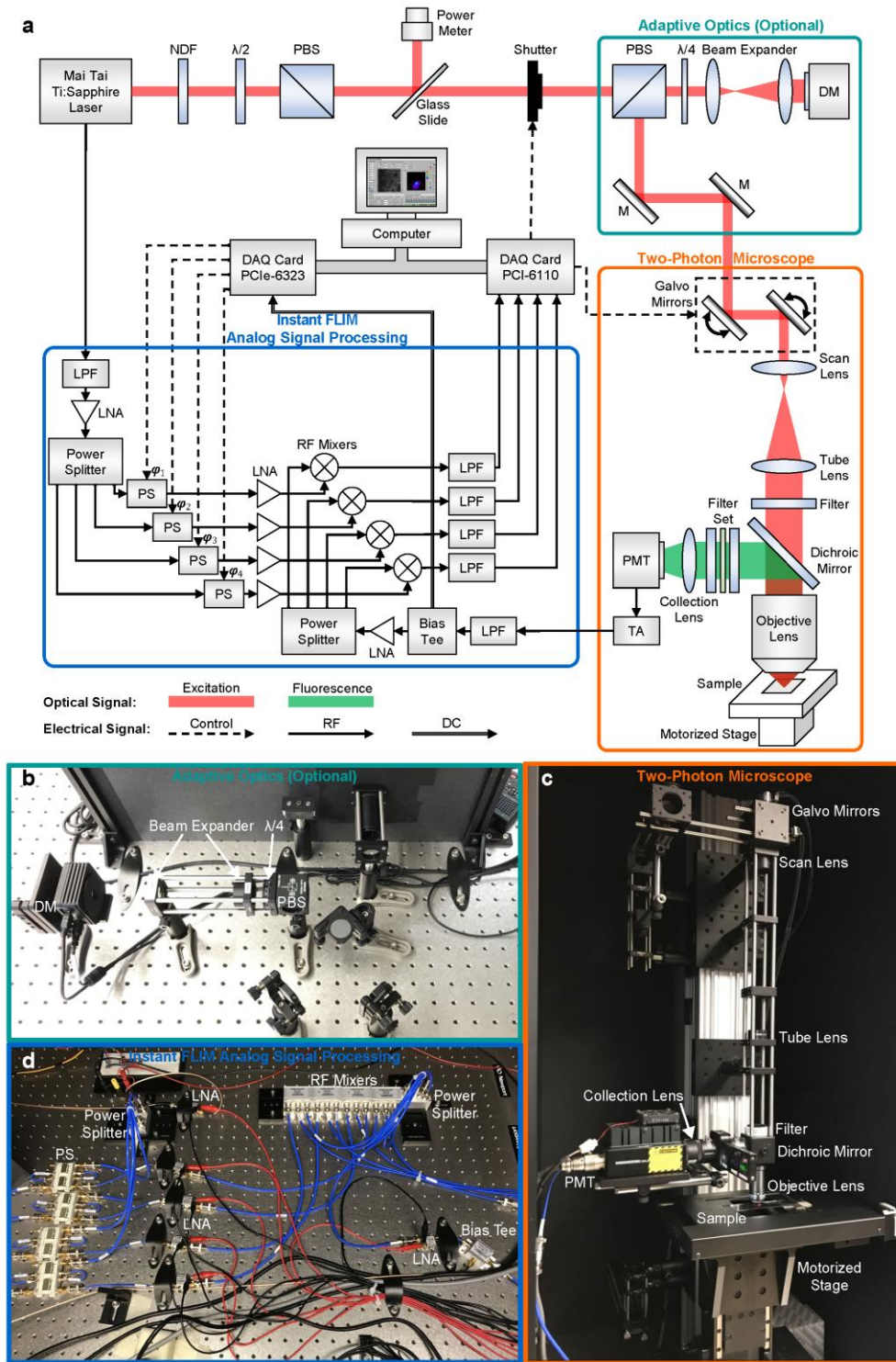
⁴*Mike and Josie Harper Cancer Research Institute, University of Notre Dame, IN, USA*

⁵*Indiana University Melvin and Bren Simon Cancer Center, Indianapolis, IN, USA*

⁶*Caltech Optical Imaging Laboratory, Andrew and Peggy Cherng Department of Medical*

Engineering, California Institute of Technology, Pasadena, CA, USA

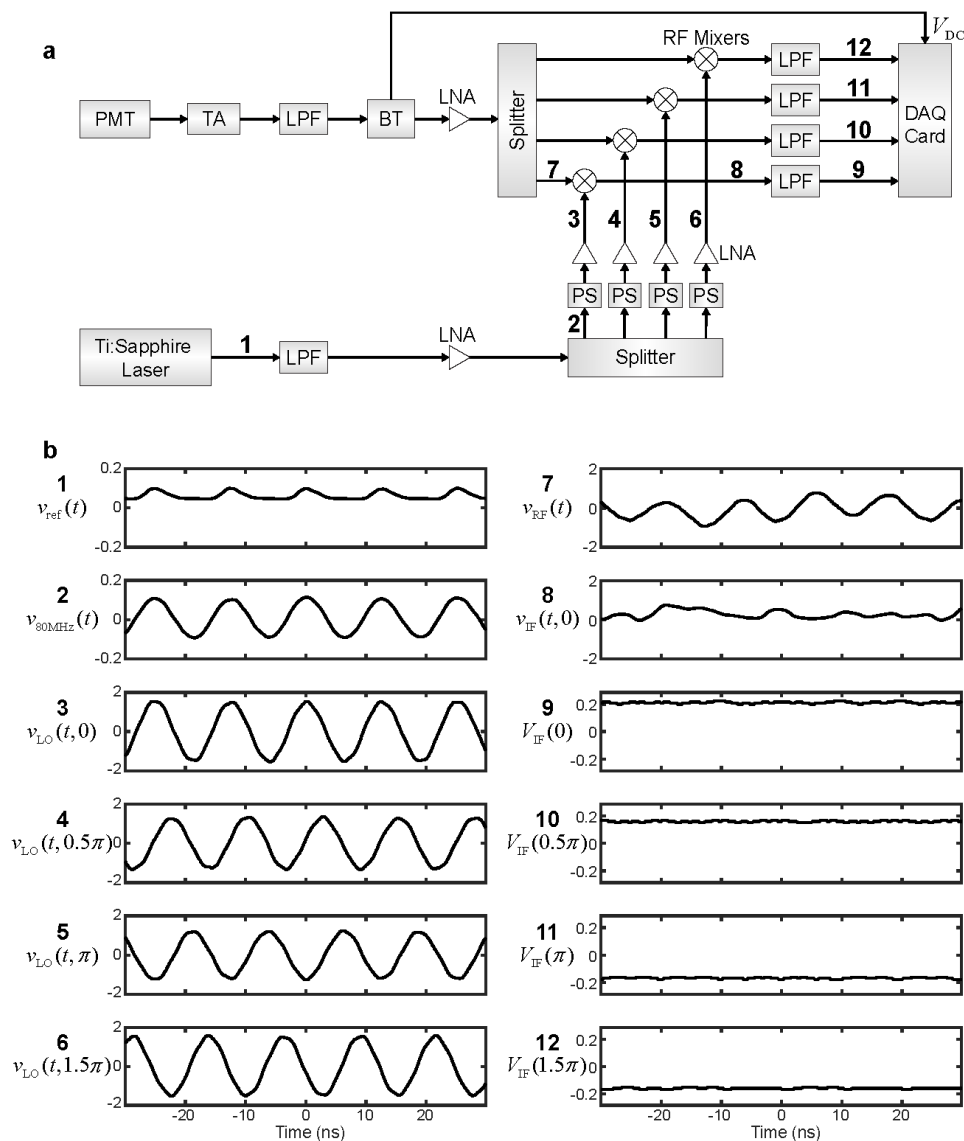
*Correspondence should be addressed to S.S.H. (showard@nd.edu)



Supplementary Figure 1

Diagram and pictures of the instant FLIM system. (a) Detailed diagram of the system configuration. NDF, neutral density filter; $\lambda/2$, half-wave plate; PBS, polarizing beam splitter; λ

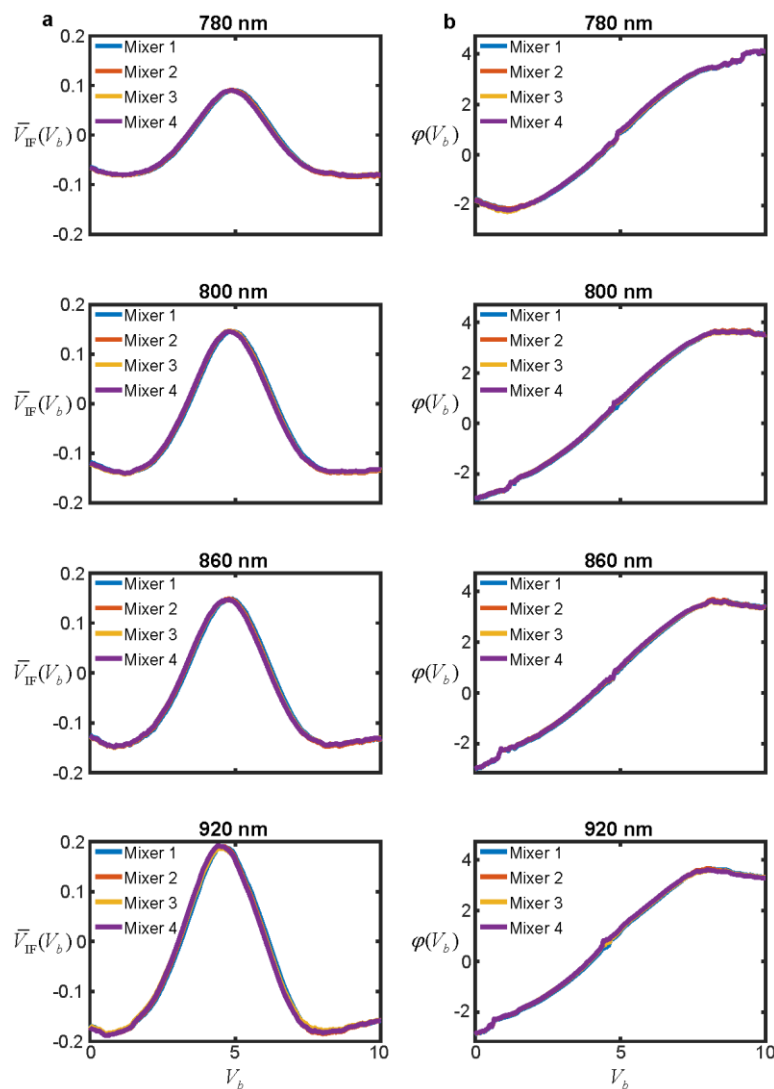
$\lambda/4$, quarter-wave plate; DM, deformable mirror; M, mirror; PMT, photomultiplier tube; TA, transimpedance amplifier; DAQ, data acquisition; LPF, low pass filter; LNA, low-noise amplifier; PS, phase shifter. Three sets of components are grouped together and highlighted as system modules. The two-photon microscope module is a conventional two-photon microscope setup; the optional adaptive optics module can improve the imaging quality and penetration depth; the analog signal processing module is the essential part of an instant FLIM system. (b) Picture of the physical implementation of the optional adaptive optics module. (c) Picture of the physical implementation of the conventional two-photon microscope module. (d) Picture of the physical implementation of the instant FLIM analog signal processing module.



Supplementary Figure 2

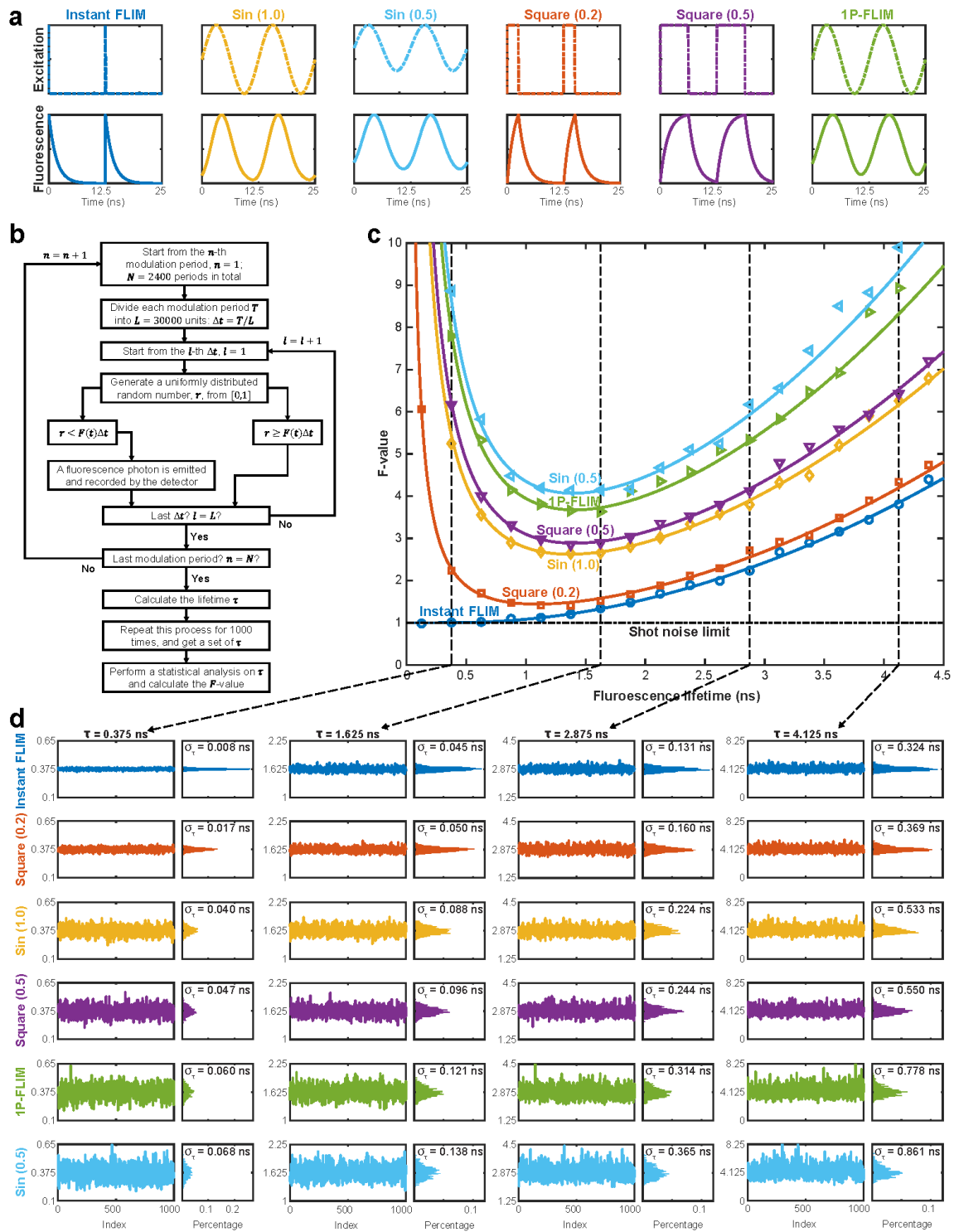
Analog signal processing in instant FLIM. (a) Diagram showing how analog signals are processed in instant FLIM. The signals are labeled with numbers and their typical waveforms are shown in (b). (b) Waveforms of the analog signals under real experimental conditions: excitation wavelength, 920 nm; sample, coumarin 6 in methanol; excitation power, 3.6 mW. These signals are: 1, $v_{ref}(t)$, the reference signal from the mode-locked Ti:sapphire laser; 2, $v_{80MHz}(t)$, the pure 80 MHz signals after low pass filtering, amplifying, and splitting the reference signal; 3-6,

$v_{LO}(t, \varphi)$, the phase shifted reference signals directed to the mixers' LO ports; 7, $v_{RF}(t)$, the low pass filtered, amplified, and split PMT signals directed to the mixers' RF ports; 8, $v_{IF}(t, \varphi)$, the mixed signals generated on the mixers' IF ports; 9-12, $V_{IF}(\varphi)$, the low pass filtered (DC) mixed signals that will be measured by a DAQ card. Unit, volts.



Supplementary Figure 3

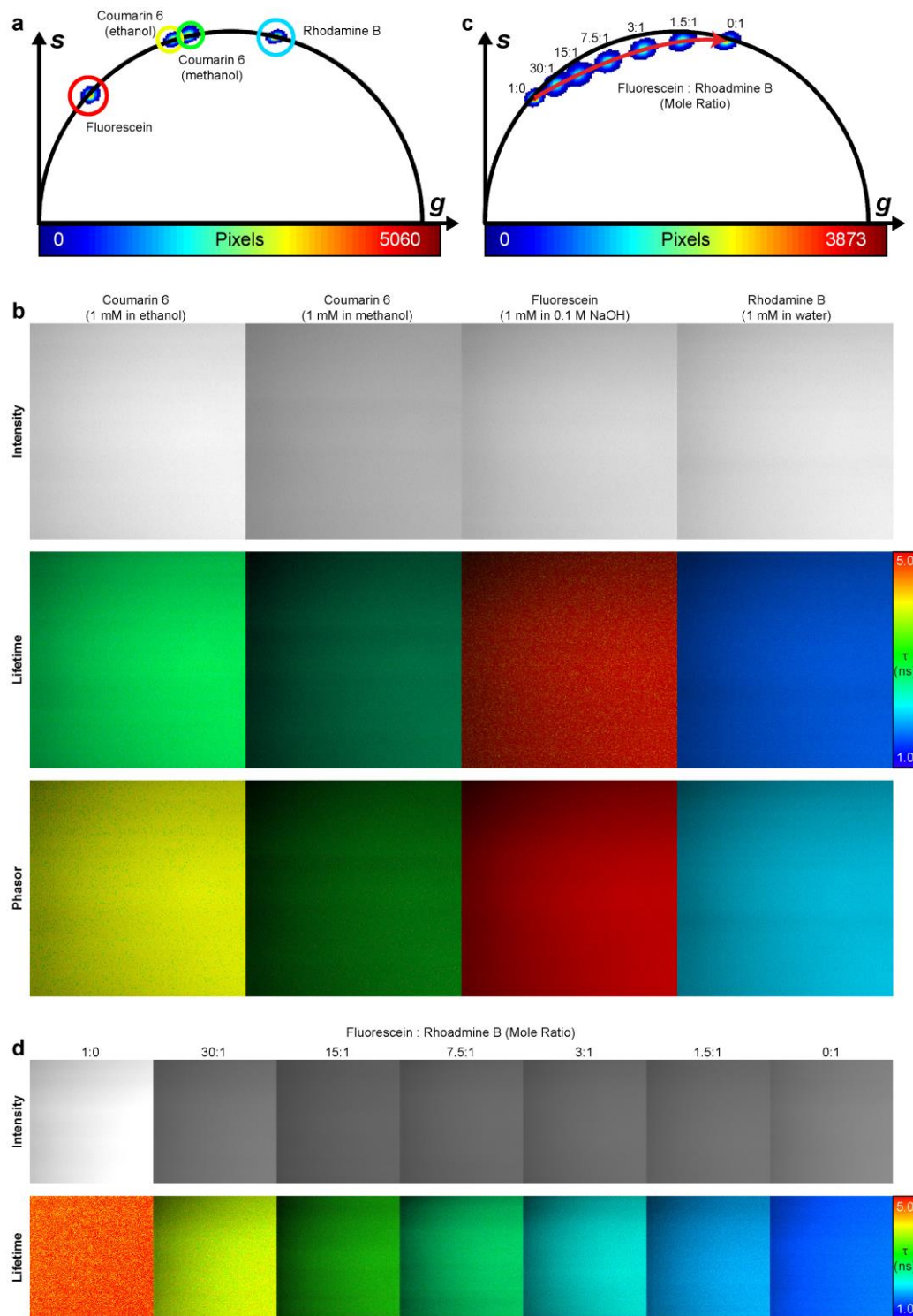
Instant FLIM system calibration using a lifetime standard. (a) Raw calibration curves acquired from a lifetime standard (1 mM coumarin 6 in methanol) by changing the bias voltage (V_b , stepping from 0 to 10V) applied to the four phase shifters and measuring the voltages (\bar{V}_{IF}) on the four mixers' IF ports. A set of calibration curves should be measured for each excitation wavelength that will be used for imaging. Here we show the curves for excitation wavelengths at 780 nm, 800 nm, 860 nm, and 920 nm. Unit, volts. (b) Phase calibration curves, $\varphi(V_b)$, generated using Eq. (S21) based on the raw data in (a). Unit, radians.



Supplementary Figure 4

SNR performances of instant FLIM and conventional FD-FLIM techniques. (a) Excitation and fluorescence waveforms of the six FD-FLIM techniques in comparison: instant FLIM, this work;

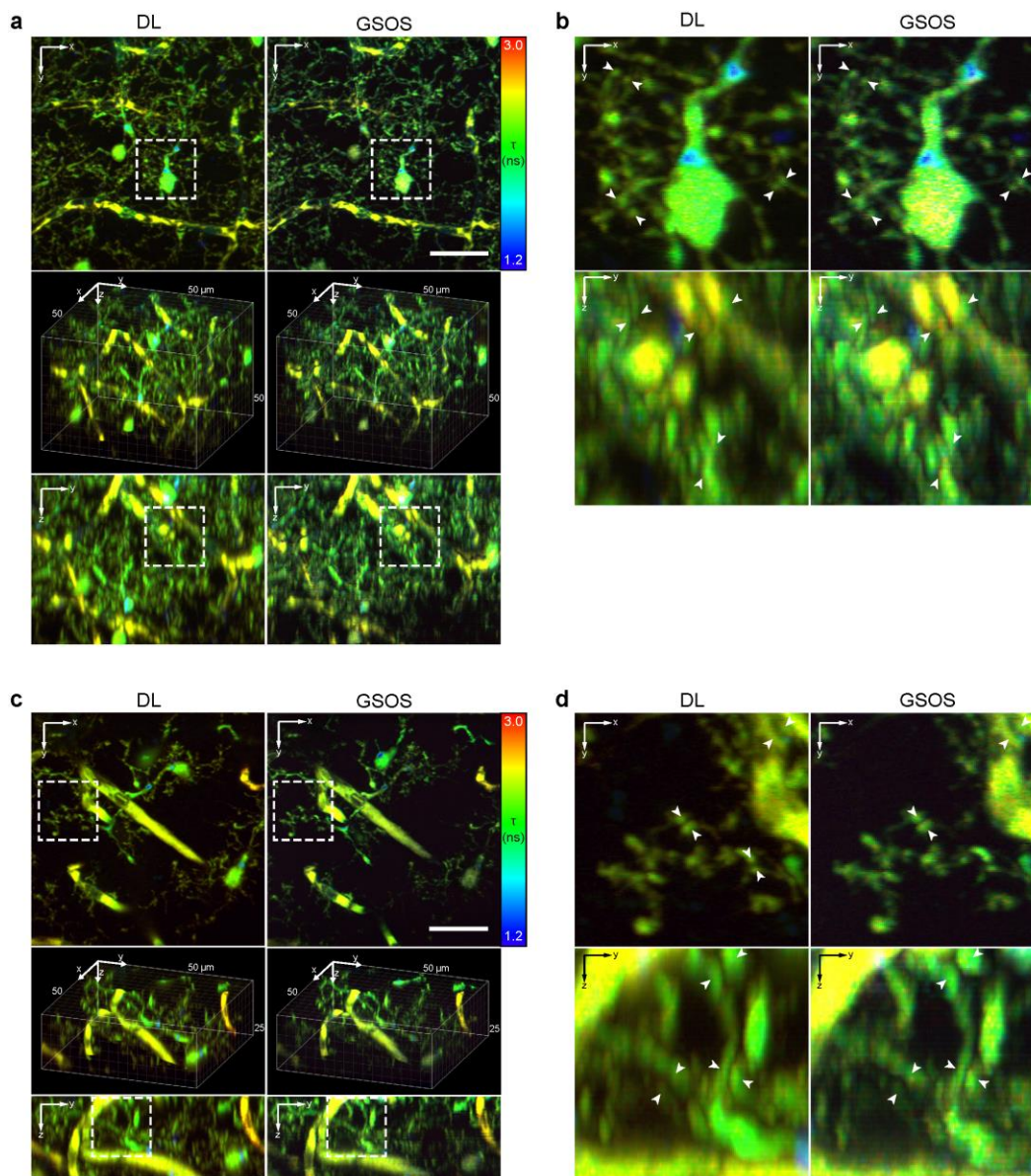
Sin (1.0), two-photon (2P) sinusoidal (1.0 modulation degree) modulation; Sin (0.5), 2P sinusoidal (0.5 modulation degree) modulation; Square (0.2), 2P periodic square wave (0.2 duty cycle) modulation; Square (0.5), 2P periodic square wave (0.5 duty cycle) modulation; 1P-FLIM, one-photon (1P) sinusoidal (1.0 modulation degree) modulation. Modulation period, 12.5 ns (80 MHz). (b) Diagram summarizing the Monte Carlo simulation process. (c) F -values as a function of fluorescence lifetimes with modulation frequency fixed at 80 MHz for different FD-FLIM methods. The symbols and curves are results of the numerical Monte Carlo simulation and the analytical error-propagation analysis, respectively. (d) Simulated lifetime measurements extracted from four different lifetime values in the Monte Carlo simulations for different FD-FLIM methods. The histograms as well as the standard deviations of the lifetime measurements are also shown.



Supplementary Figure 5

Phasor plots of lifetime standards and fluorophore mixtures. (a) Phasor plot of four lifetime standards acquired with an instant FLIM system: 1 mM coumarin 6 in methanol ($\tau = 2.3$ ns at

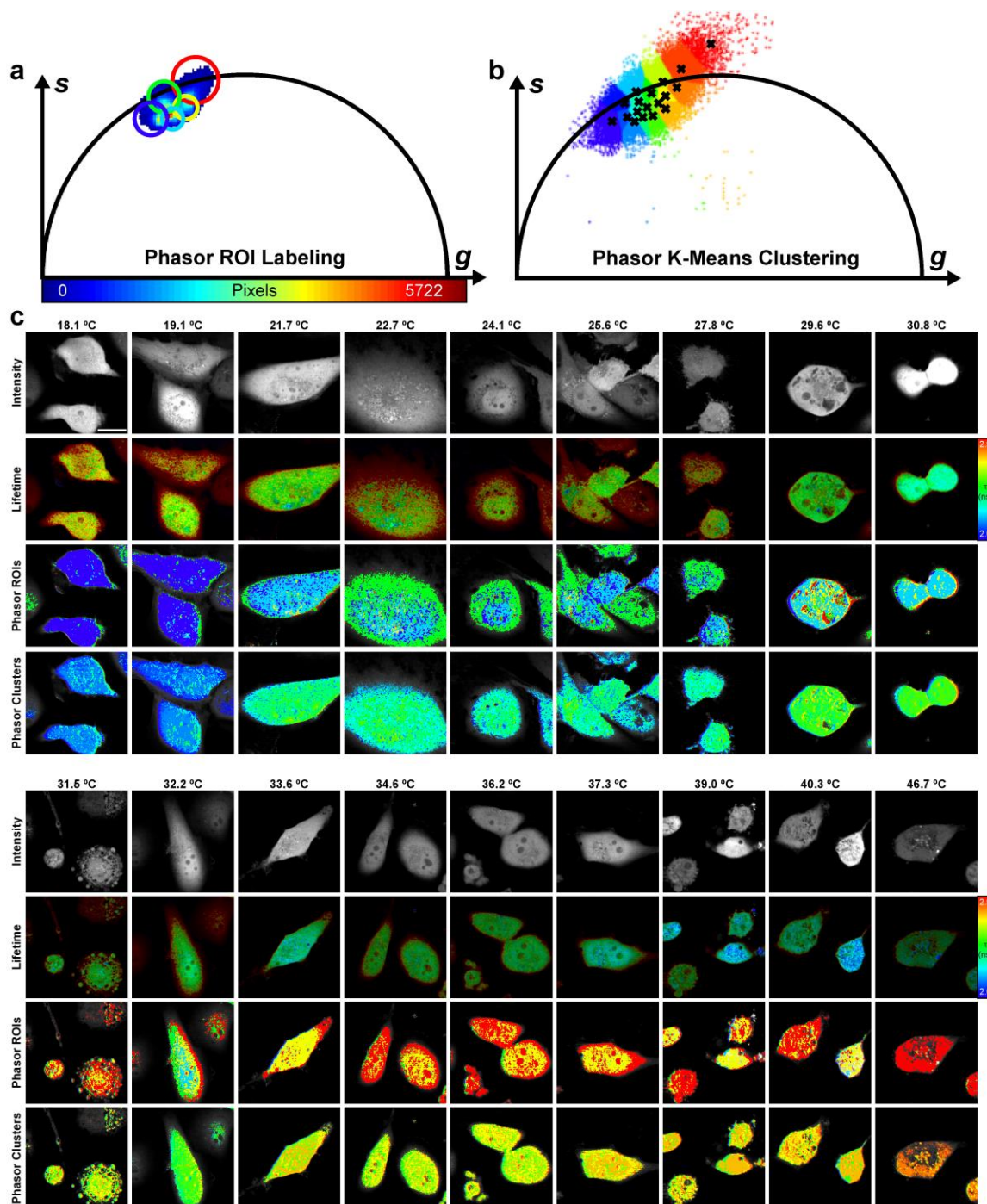
20 °C), 1 mM coumarin 6 in ethanol ($\tau = 2.4$ ns at 20 °C), 1mM fluorescein in 0.1 M NaOH ($\tau = 4.0$ ns at 20 °C), and 1 mM rhodamine B in water ($\tau = 1.7$ ns at 20 °C). Four ROIs are drawn to isolate the phasors of these standards and to label their corresponding pixels in the raw images, as shown in (b). (b) Intensity, lifetime, and phasor ROI-labeled images of the standards in (a). Whereas it is hard to differentiate these standards based on their intensity, it is straightforward to separate them using their lifetime or phasor ROI-labeled images. (c) Phasor plot of fluorophore solutions mixed with different mole ratios of fluorescein and rhodamine B. The red arrow indicates how the phasors shift when more rhodamine B solution is added to the mixture. (d) Intensity and lifetime images of the fluorophore mixtures with different mole ratios of fluorescein and rhodamine B in (c).



Supplementary Figure 6

3D super-resolution FLIM by applying GSOS to instant FLIM data. (a) Composite 3D lifetime stacks of a fixed Cx3cr1-GFP/+ mouse brain (microglia labeled with EGFP; blood vessel injected with Dextran 594) captured by an instant FLIM system conventionally (left) and combined with the two-step GSOS technique (right), where the intensity and fluorescence lifetime are mapped to voxels' brightness and hue, respectively. The conventional diffraction-limited (DL) stack was imaged at a power of 12.31 mW, and the GSOS stack was generated by

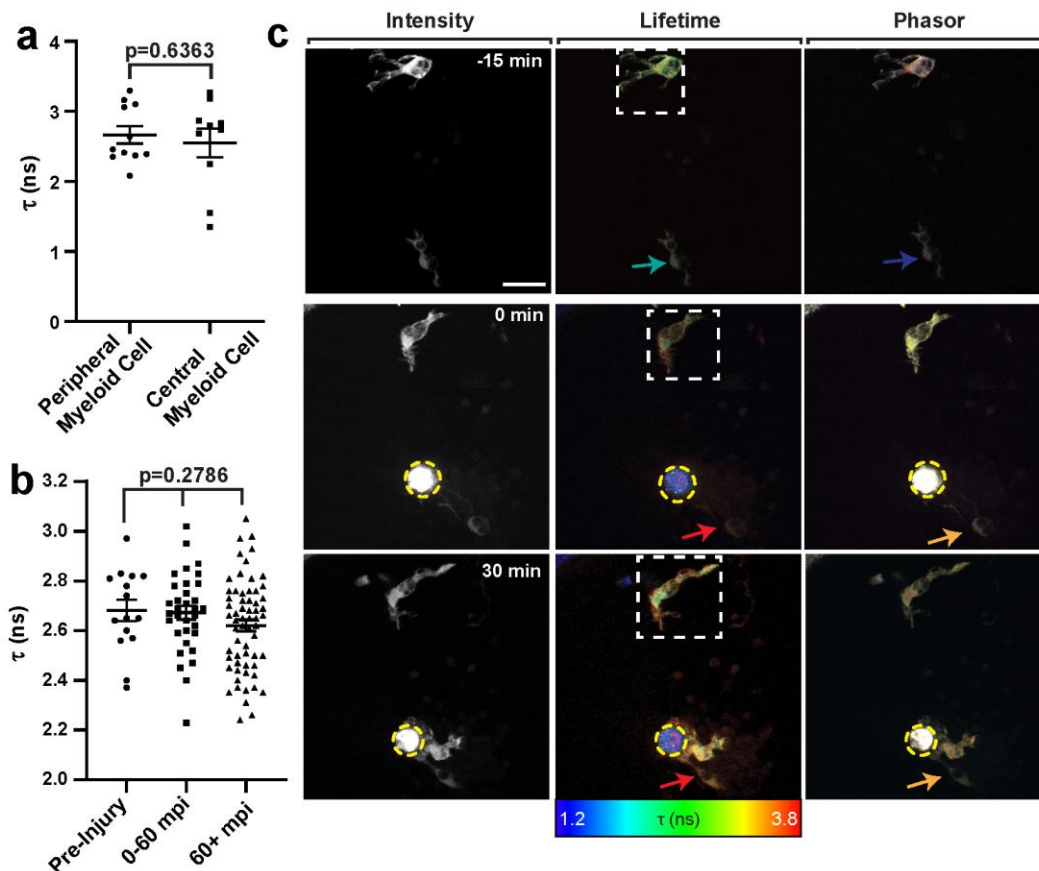
linear combining two stacks imaged at 12.31 mW and 13.44 mW. Shown are the maximized z-projection (top), 3D reconstruction (middle), and maximized x-projection (bottom) of the stacks. (b) Magnified views of the white dashed boxes in (a). White arrows indicate features that are better resolved in the GSOS stack. (c) Composite 3D lifetime stacks of a fixed mouse brain imaged at the same condition as that in (a). (d) Magnified views of the white dashed boxes in (c). White arrows indicate features that are better resolved in the GSOS stack. Scale bar, 20 μm .



Supplementary Figure 7

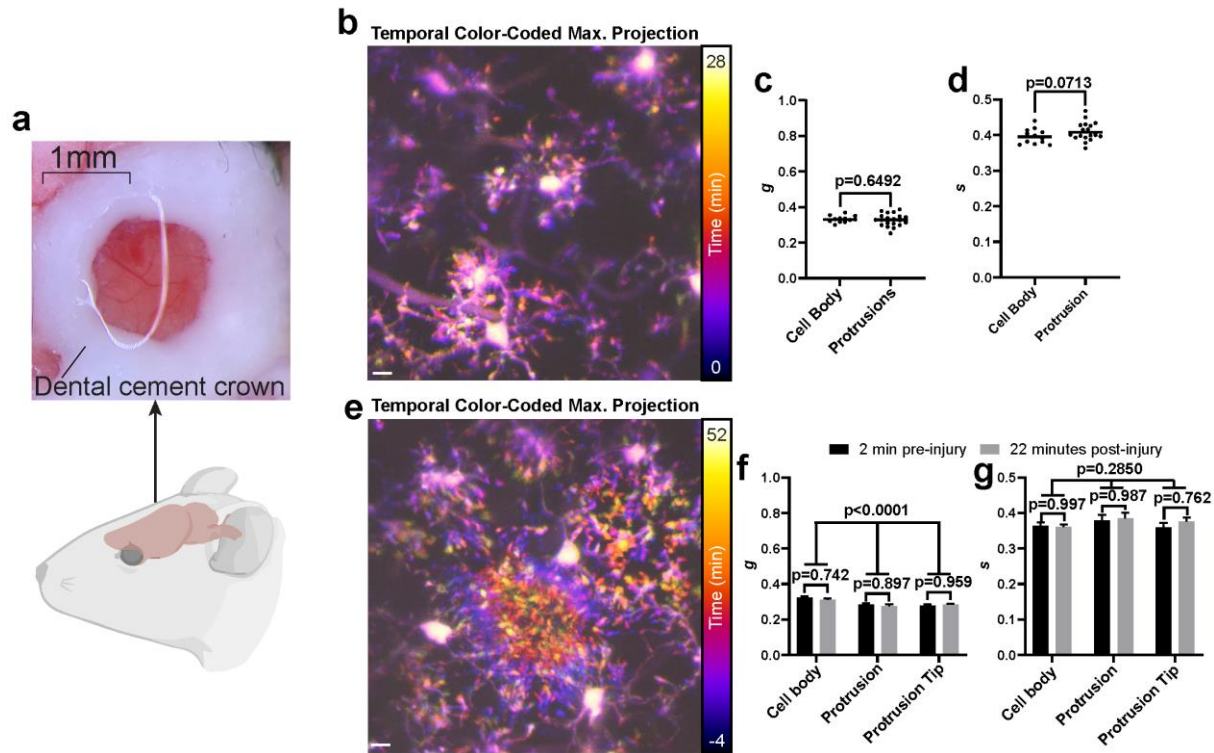
Temperature dependence of GFP lifetimes in live cells. (a) Combined phasor plot of 18 images of MDA-MB-231-EGFP cells acquired with an instant FLIM system. The ROIs are manually drawn to segment the phasor points and are used to label the corresponding pixels in (c). (b)

Phasor plot in (a) processed with the K-means clustering algorithm, where $K=18$ clusters were used to recognize the phasor shift induced by the 18 different temperatures. The phasors are automatically clustered into 18 groups and their corresponding pixels are labeled in (c). (c) Fluorescence intensity, lifetime, phasor ROI-labeled, and phasor K-means clustering-labeled images of the MDA-MB-231-EGFP cells under 18 different temperatures. As temperature increases, the GFP lifetimes decrease and the phasors shift from bottom-left to top-right of the phasor plot. Scale bar, 20 μm .



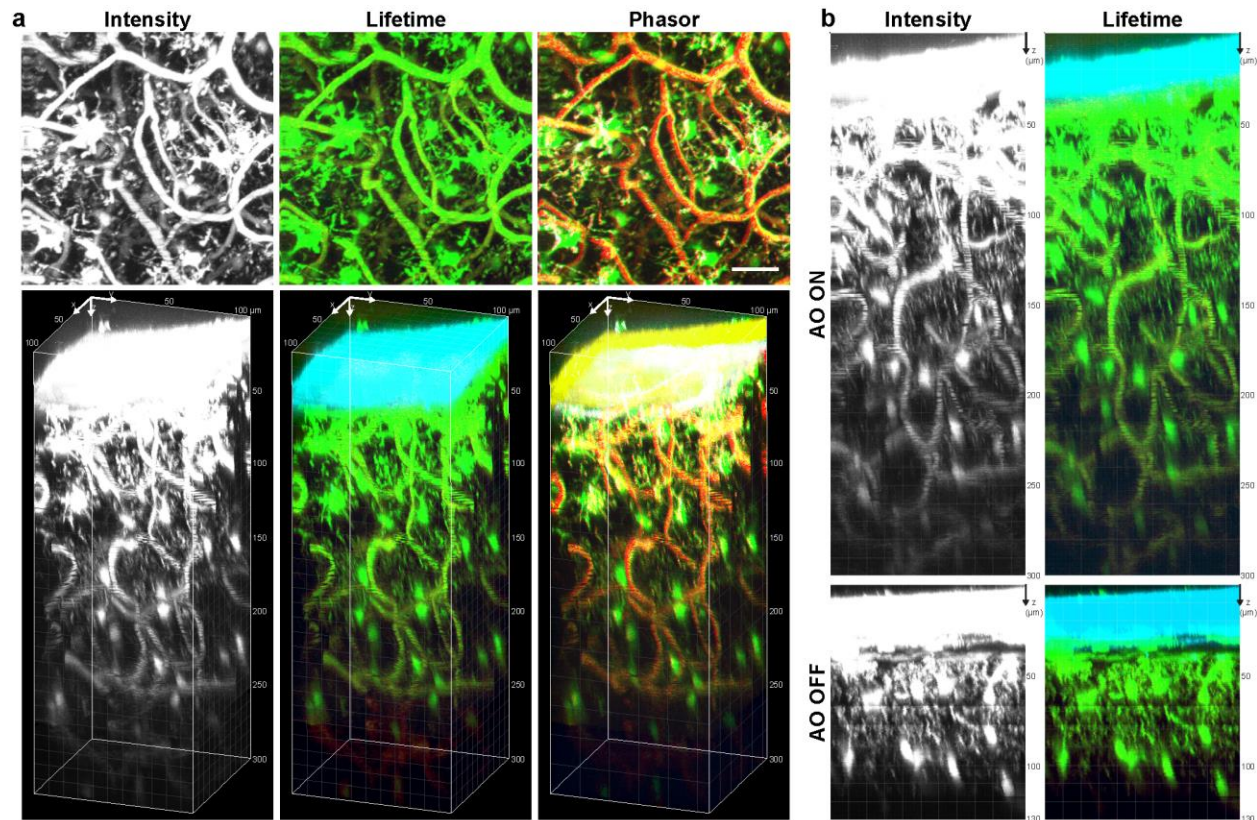
Supplementary Figure 8

Analysis of fluorescence lifetime dynamics in living zebrafish. (a) Graph of average fluorescence lifetime in CNS-located (n=10 cells) and PNS-located (n=11 cells) myeloid cells. (b) Graph of average fluorescence lifetime in microglia before laser injury (n=15 cells), 0-60 mpi (n=32 cells), and 60+ mpi (n=62 cells). (c) Instant FLIM images of *Tg(pul:gfp)* zebrafish at 4 dpf of microglia from a 4-hour time-lapse movie before and after laser injury. The left images represent fluorescent intensity, the middle images represent fluorescence lifetime, and the right images are labeled with phasor ROIs. Dashed yellow circle denotes the lesion site. Arrows denote approximate lifetime and phasor pseudo-coloring. Dashed white circle denotes inset shown in **Fig. 3g**. Scale bar, 10 μ m. (a) uses a Student's *t*-test. (b) uses a one-way ANOVA.



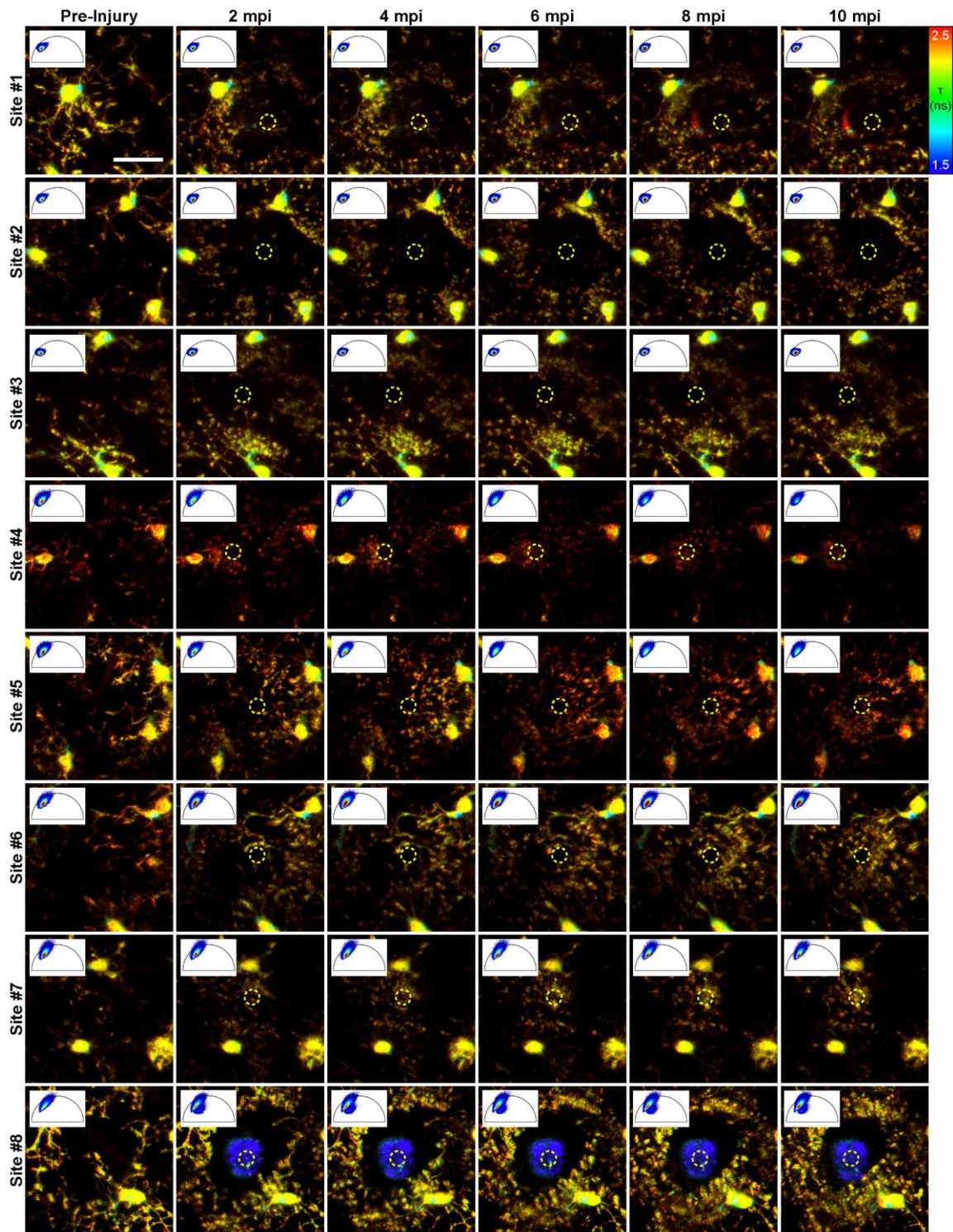
Supplementary Figure 9

Analysis of fluorescence lifetime dynamics in living mice. (a) Image of a thinned mouse skull with a dental cement crown used for imaging. (b) Maximum z-projection image of a Cx3cr1-GFP/+ mouse brain pseudo-colored to represent the temporal dynamics of the microglia. The temporal scale is shown on the right. (c-d) Graphs of g (c) and s (d) lifetime components in microglia cell bodies ($n=12$ cell bodies) and protrusions ($n=20$ protrusions). (e) Maximum z-projection images of a Cx3cr1-GFP/+ mouse brain following laser injury pseudo-colored to represent the temporal dynamics of the microglia. The temporal scale is shown on the right. (f-g) Graphs of g (f) and s (g) lifetime components in cell bodies ($n=5$ cell bodies), protrusions ($n=5$ protrusions), and protrusion tips ($n=5$ protrusion tips) 2 minutes before and 22 minutes after injury. Scale bar, 1 mm (a) and 10 μm (b,e). (c,d) use a Student's t -test. (f-g) use a two-way ANOVA with multiple comparisons.



Supplementary Figure 10

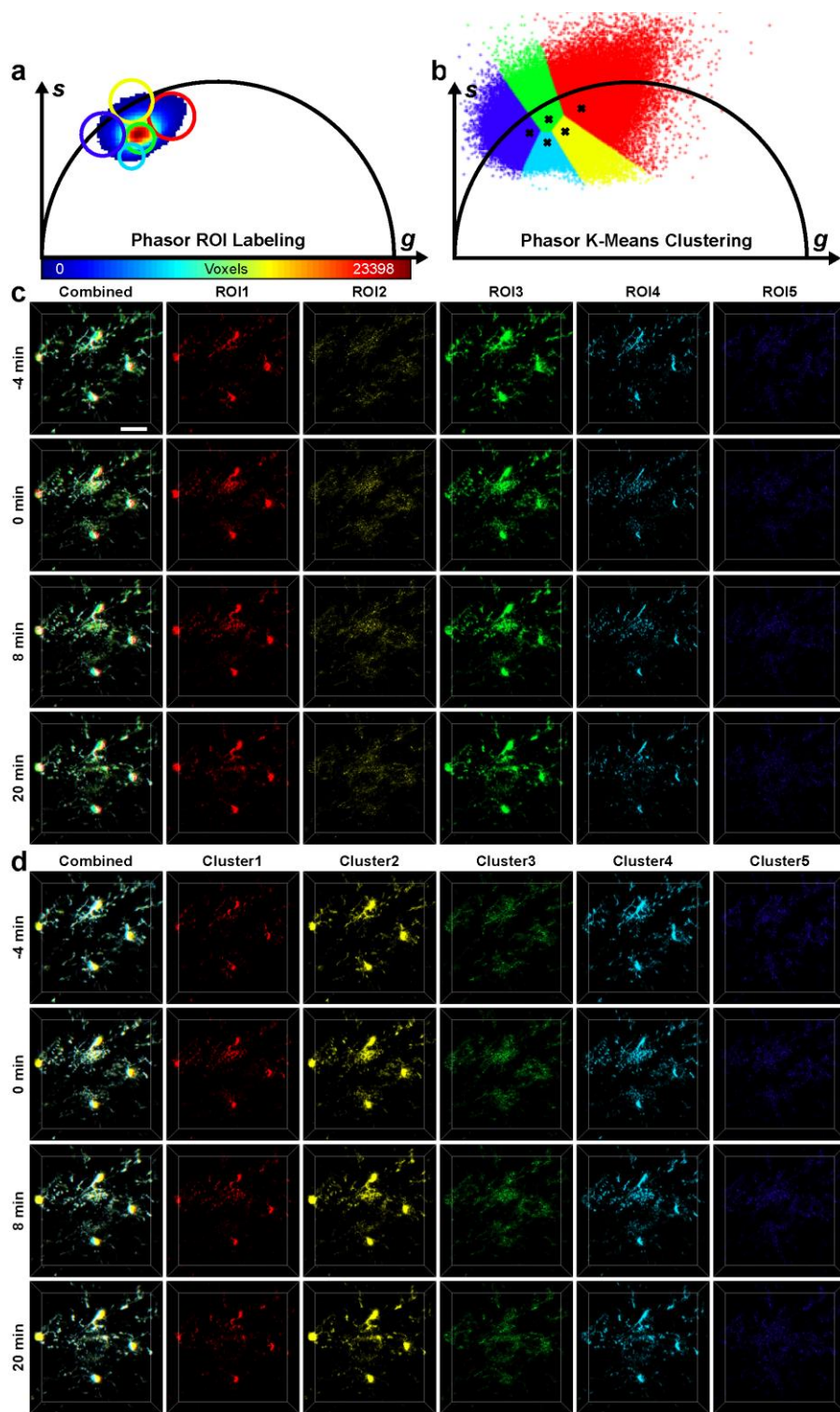
Through-skull 3D FLIM of a living mouse brain imaged by instant FLIM combined with adaptive optics. (a) Two-photon fluorescence intensity, lifetime, and phasor ROI-labeled 3D stacks of an intact brain in a living *Cx3cr1-GFP/+* mouse acquired with an instant FLIM system combined with an adaptive optics (AO) module based on a deformable mirror. The microglia were labeled with EGFP, and the blood vessels were injected with Texas Red-Dextran. Shown are the maximized z-projections (top) and 3D reconstructions (bottom) of the stacks. (b) Top, the maximized x-projections of the intensity and lifetime stacks in (a); bottom, the maximized x-projections of the 3D intensity and lifetime stacks acquired with the instant FLIM system from the same animal but without the AO module. The excitation power was gradually increased from 8.53 mW to 21.13 mW to compensate for the signal loss as the imaging depth increased. Scale bar, 20 μm .



Supplementary Figure 11

3D time-lapse two-photon fluorescence lifetime images (maximized z-projections) and phasor plots of the microglia in a living Cx3cr1-GFP/+ mouse brain. The images were acquired with an

instant FLIM system. A laser injury was induced 2 minutes after the first column by an 800 nm laser with a power of 43.50 mW lasting for 120 s. Each row corresponds to an injury experiment performed on one of two mice. The sites of the injury are denoted with dashed yellow circles. Whereas no obvious change can be seen among the phasors after the injury (second to sixth columns), noticeable differences can be observed between the phasors before (first column) and after the injury (second column). This phenomenon can be better visualized **with Supplementary Video 6**. Scale bar, 20 μm .

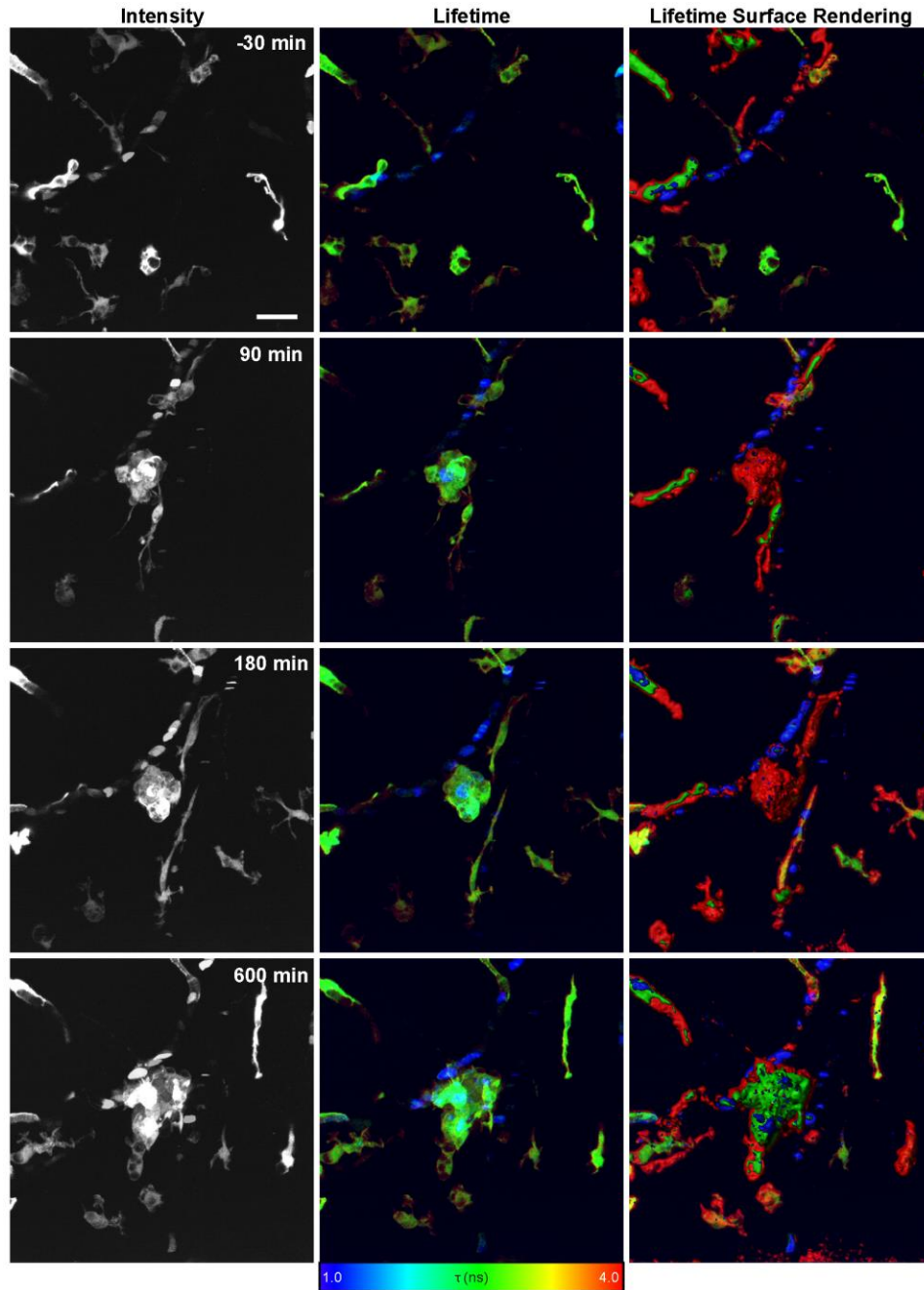


Supplementary Figure 12

K-means clustering applied to 4D instant FLIM data of microglia in a living mouse brain. (a)

Phasor plot of the time-lapse 3D FLIM stacks of the EGFP-labeled microglia in a living Cx3cr1-

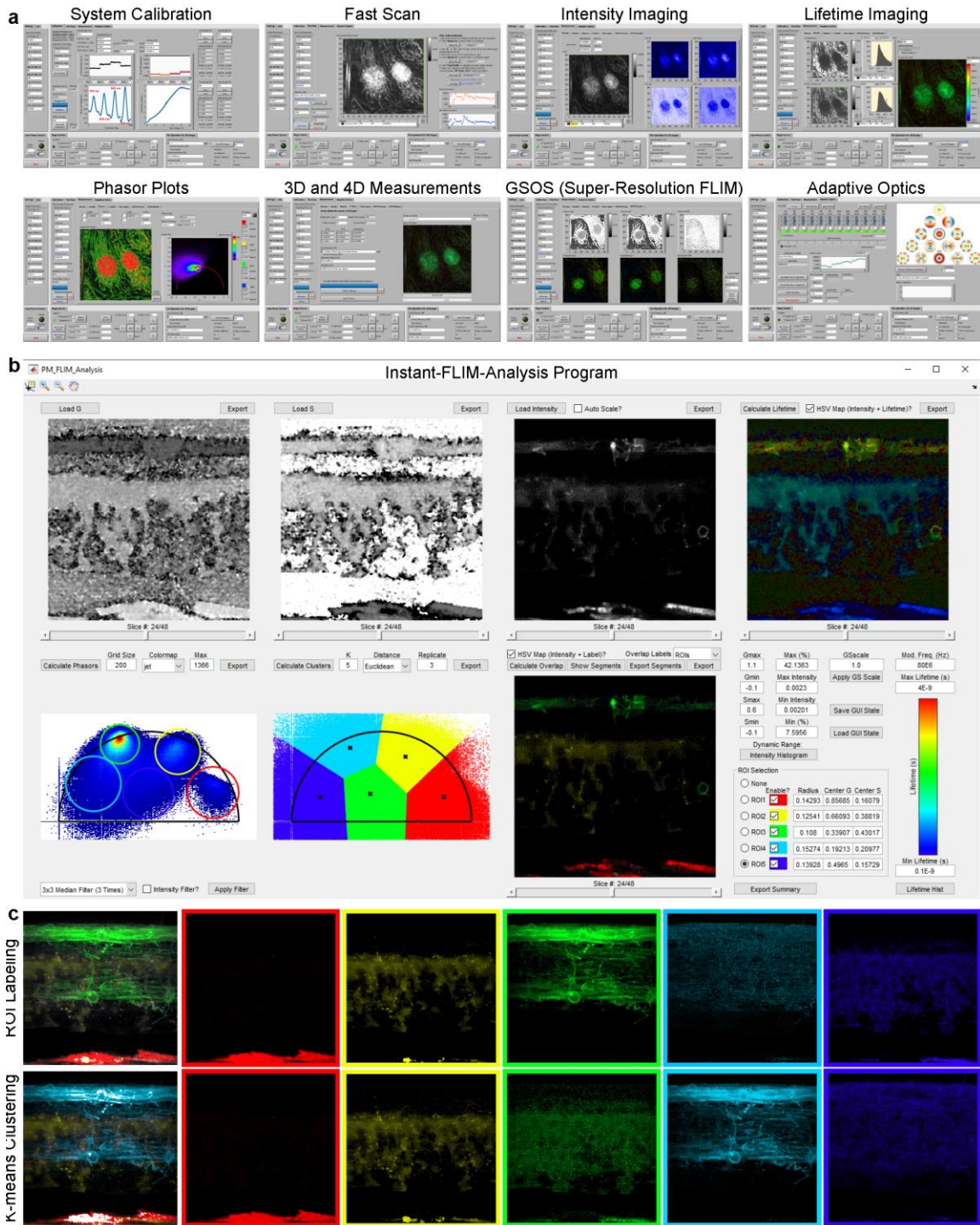
GFP/+ mouse brain acquired with an instant FLIM system. The ROIs are manually drawn to segment the phasor points and are used to label the corresponding voxels in (c). (b) Phasor plot in (a) processed with the automatic K-means clustering algorithm. We chose K=5 clusters as K values smaller or larger than 5 resulted in insufficient or redundant segmentation results. The phasors are automatically clustered into 5 groups and their corresponding voxels are labeled in (d). (c) Reconstructed time-lapse 3D stacks of the *in vivo* microglia labeled with all the phasor ROIs drawn in (a) as well as each one of them. A laser injury was induced right before $t = 0$ by an 800 nm laser with a power of 43.50 mW lasting for 120 s. The whole and the sub-cellular structures labeled with the ROIs all responded to the injury. (d) Reconstructed time-lapse 3D stacks of the same animal in (c) but with the voxels labeled with the phasor groups clustered by the K-means algorithm in (b). Like the structures manually labeled with ROIs in (c), the sub-cellular segments automatically labeled with the K-means algorithm also responded to the injury. Scale bar, 20 μm .



Supplementary Figure 13

Enhancing the qualitative information of FLIM through surface rendering composite lifetime images. Left: maximized z-projections of the 3D time-lapse two-photon intensity images of the microglia in a living *Tg(pul:gfp)* zebrafish brain at 4dpf. Middle: maximized z-projections of the 3D time-lapse composite lifetime images of the same animal, where the intensity and

fluorescence lifetime values are mapped to the voxels' brightness and hue, respectively. Right: maximized z-projections of a 3D time-lapse stacks obtained by decomposing the composite lifetime images in the RGB color space, independently surface rendering the decomposed RGB components, and recombining the rendered R, G, and B surfaces. The stacks were captured every 15 minutes to form the 3D time-lapse images. A laser injury was induced at $t = 0$ by an 800 nm laser at 43.50 mW lasting for 1 s. With the surface rendering, the cellular structures involved in the laser-induced microglia response are better differentiated compared to the ones in the lifetime images. Scale bar, 20 μm .



Supplementary Figure 14

Modules of the Instant-FLIM-Control and Instant-FLIM-Analysis software. (a) System Calibration module calibrates the instant FLIM system using a lifetime standard. Fast Scan

module allows fast acquisition (>1 frame per second) of two-photon intensity images, which can be used to locate the focal position, to find the regions of interest, and to generate image-based metrics for the AO optimization algorithms. Intensity Imaging, Lifetime Imaging, and Phasor Plots modules simultaneously generate fluorescence intensity images, lifetime images, and phasor plots as the instant FLIM system performs measurements. 3D and 4D Measurements module configures 3D and 4D instant FLIM measurements and displays the results. GSOS Module permits two-step GSOS super-resolution FLIM using two groups of instant FLIM images captured under different excitation powers. Adaptive Optics Module (optional) optimizes the Zernike coefficients applied to the deformable mirror using the three AO optimization algorithms described in **Supplementary Note 6**. (b) Screenshot of the Instant-FLIM-Analysis program where the 3D intensity and phasor stacks of a living *Tg(sox10:megfp)* zebrafish embryo (2dpf) acquired with an instant FLIM system were imported and analyzed according to **Supplementary Protocol 2**. (c) Top, maximized z-projections of the exported 3D stacks labeled by the phasor ROIs manually drawn in (b). Bottom, maximized z-projection of the exported 3D stacks labeled by the phasor clusters automatically segmented in (b) using the K-means clustering algorithm, where K=5 clusters were used as it clearly segmented the EGFP-labeled (cyan) and endogenous cellular structures (other colors).

Supplementary Note 1. Principle of instant FLIM.

We first assume the fluorescence sample has a single-exponential decay with an impulse response function $f(t) = \exp(-t/\tau)/\tau$, where τ is the fluorescence lifetime and the function's integral on the time domain ($t \geq 0$) is normalized to one. The modeling and methods for fluorophores with multi-exponential decay are presented in **Supplementary Note 2**. A mode-locked Ti:sapphire laser which outputs femtosecond pulses at 80 MHz is used as the excitation source. Since the femtosecond pulses are so short (100 fs) compared to the 12.5 ns modulation period (80 MHz), we can consider these pulses as a Dirac comb with a period of $T = 12.5$ ns. Mathematically, the excitation irradiance is $I(t) = P\delta_T(t)$, where P is a coefficient related to the average power of the laser beam. Based on the quadratic nature of two-photon excitation, the fluorescence $F(t)$ is proportional to the convolution of $I^2(t)$ and $f(t)$,

$$F(t) = cI^2(t) * f(t) = \frac{P^2c}{\tau} \delta_T(t) * \exp\left(-\frac{t}{\tau}\right), \quad (\text{S1})$$

where c represents the fluorophore concentration. Since the fluorescence signal $F(t)$ is periodic with an angular frequency of $\omega = 2\pi/T$, it can be written as Fourier series,

$$F(t) = \sum_{k=-\infty}^{+\infty} q_k \exp(ik\omega t), \quad (\text{S2})$$

where the Fourier coefficients q_k are

$$q_k = \frac{1}{T} \int_0^T F(t) \exp(-ik\omega t) dt = \frac{P^2c}{T} \frac{1}{1+ik\tau\omega}. \quad (\text{S3})$$

We separate the fluorescence signal $F(t)$ detected by a photomultiplier tube (PMT) into DC and RF parts using a bias tee. The DC part is linearly related to q_0 and can be written as

$$V_{\text{DC}} = Bq_0 + O_B = \frac{BP^2c}{T} + O_B, \quad (\text{S4})$$

where B is the conversion loss from the bias tee's RF&DC to DC ports, and O_B is the offset that is invariant to the PMT signal variations. The RF part, on the other hand, is $\sum_{k \neq 0} q_k \exp(ik\omega t)$.

Since $q_k = q_{-k}^*$, it can also be written as

$$v_{\text{RF}}(t) = 2 \sum_{k \in \mathbb{Z}^+} \text{Re} \{ q_k \exp(ik\omega t) \} = \frac{2P^2c}{T} \sum_{k \in \mathbb{Z}^+} \frac{1}{1 + (k\tau\omega)^2} [\cos(k\omega t) + k\tau\omega \sin(k\omega t)]. \quad (\text{S5})$$

A homodyne detection method is used to extract the lifetime information from the first harmonic (1ω) of $v_{\text{RF}}(t)$. In this work, we use RF mixers to mix the fluorescence signal with the 80 MHz reference signal from the Ti:sapphire laser. We use the reference signal from the laser because **(a)** the laser repetition rate has a ± 1 MHz variance so a fixed-frequency external reference signal could introduce errors, and **(b)** the implementation is cost-effective as all required RF components cost less than \$2,500. The reference signal is low-pass filtered and amplified such that it only contains the fundamental harmonic (1ω). For both the fluorescence and reference signals, a 4-way power splitter is used to split the signal to four paths. We call this operation phase multiplexing because the four paths are operated independently and simultaneously during imaging acquisition. For each reference signal path, a phase shifter is utilized to introduce a voltage-controlled phase shift of φ ($0 - 2\pi$) to the signal. The reference signals are sent to the local oscillator (LO) ports of the mixers and can be denoted as

$$v_{\text{LO}}(t, \varphi) = \sin(\omega t + \varphi). \quad (\text{S6})$$

During the phase multiplexing, the four mixers take the PMT and reference signals to their RF and LO ports, respectively. In theory, the output signal on the intermediate frequency (IF) ports

can be regarded as the product of the signals on its RF and LO ports; in practice, however, a DC offset due to circuit imbalance also exists in the output¹. We denote this DC offset as

$$O_M = O(P_{\text{RF}}) + d, \quad (\text{S7})$$

where $O(P_{\text{RF}})$ is a function of the RF signal's power, P_{RF} , and d is a constant. The DC offset O_M cannot be eliminated; it could be minimized by matching the powers of the RF and LO signals¹, but in our setup P_{RF} is a variable related to the excitation power and fluorophore concentration, and hence the powers of RF and LO do not match. Considering the existence of O_M , we model the output of the mixers as

$$v_{\text{IF}}(t, \varphi) = M v_{\text{LO}}(t, \varphi) v_{\text{RF}}(t) + O_M, \quad (\text{S8})$$

where M is the conversion loss from the mixer's RF to IF ports. The mixers' outputs are then low-pass filtered to eliminate all the harmonics; therefore, the filtered signals are pure DC voltages, as

$$\begin{aligned} V_{\text{IF}}(\varphi) &= \frac{1}{T} \int_0^T v_{\text{IF}}(t, \varphi) dt \\ &= \frac{P^2 M c}{T} \frac{1}{1 + (\tau\omega)^2} [\sin(\varphi) + \tau\omega \cos(\varphi)] + O_M \\ &= \frac{P^2 M c}{T} \frac{1}{\sqrt{1 + (\tau\omega)^2}} \sin[\varphi + \arctan(\tau\omega)] + O_M, \end{aligned} \quad (\text{S9})$$

which are sampled by a DAQ card and used to calculate fluorescence lifetimes.

A calibration procedure described in **Supplementary Note 3** is required before measurement. When the calibration is complete, we can control the phase shifts φ by applying corresponding bias voltages to the phase shifters; we will also have the knowledge of M/B , a ratio between the conversion losses of the mixer and the bias tee, that will be used for lifetime and phasor

calculations. The phase multiplexing measurement is performed by applying four different phase shifts, 0 , 0.5π , π and 1.5π , respectively, to the four phase shifters on the reference signal paths. Based on Eq. (S9), the measured mixer outputs are

$$\begin{aligned}
 V_{\text{IF}}(0) &= \frac{P^2 Mc}{T} \frac{\tau\omega}{1+(\tau\omega)^2} + O_M, \\
 V_{\text{IF}}(0.5\pi) &= \frac{P^2 Mc}{T} \frac{1}{1+(\tau\omega)^2} + O_M, \\
 V_{\text{IF}}(\pi) &= \frac{P^2 Mc}{T} \frac{-\tau\omega}{1+(\tau\omega)^2} + O_M, \\
 V_{\text{IF}}(1.5\pi) &= \frac{P^2 Mc}{T} \frac{-1}{1+(\tau\omega)^2} + O_M.
 \end{aligned}
 \tag{S10}$$

Then, by taking the differences among them, we will have

$$\begin{aligned}
 V_{\text{IF}}(0) - V_{\text{IF}}(\pi) &= \frac{2P^2 Mc}{T} \frac{\tau\omega}{1+(\tau\omega)^2}, \\
 V_{\text{IF}}(0.5\pi) - V_{\text{IF}}(1.5\pi) &= \frac{2P^2 Mc}{T} \frac{1}{1+(\tau\omega)^2},
 \end{aligned}
 \tag{S11}$$

which are proportional to the imaginary and real parts of the first harmonic (1ω) Fourier coefficient of the fluorescence, q_1 , in Eq. (S3). Based on the 1ω measurements in Eq. (S11), it is easy to extract the fluorescence lifetime by

$$\tau = \frac{1}{\omega} \frac{V_{\text{IF}}(0) - V_{\text{IF}}(\pi)}{V_{\text{IF}}(0.5\pi) - V_{\text{IF}}(1.5\pi)}.
 \tag{S12}$$

Supplementary Note 2. Phasor approach to address multi-exponential decay.

We assumed that the fluorescence sample had a single-exponential decay in **Supplementary Note 1**. In this Note, we show that the proposed instant FLIM method is also applicable for fluorophores with multi-exponential decay by employing phasor plot approaches²⁻⁴. Considering that the fluorophore sample consists of multiple fluorophores with different lifetimes, τ_i , the impulse response function becomes

$$f(t) = \sum_i a_i \frac{1}{\tau_i} \exp\left(-\frac{t}{\tau_i}\right), \quad (\text{S13})$$

where a_i is the intensity weighted fractional contribution of the fluorophore with lifetime τ_i , and $\sum_i a_i = 1$. Therefore, Eq. (S3) becomes

$$q_k = \frac{P^2 c}{T} \sum_i a_i \frac{1}{1 + ik\tau_i \omega}, \quad (\text{S14})$$

and Eq. (S11) changes to

$$\begin{aligned} V_{\text{IF}}(0) - V_{\text{IF}}(\pi) &= \frac{2P^2 Mc}{T} \sum_i a_i \frac{\tau_i \omega}{1 + (\tau_i \omega)^2}, \\ V_{\text{IF}}(0.5\pi) - V_{\text{IF}}(1.5\pi) &= \frac{2P^2 Mc}{T} \sum_i a_i \frac{1}{1 + (\tau_i \omega)^2}. \end{aligned} \quad (\text{S15})$$

On the other hand, the DC signal from the bias tee, Eq. (S4), does not change when we assume a multi-exponential decay model. If we divide Eq. (S15) by $2(V_{\text{DC}} - O)$ in Eq. (S4) and the calibration coefficient M/B , we get

$$\begin{aligned} g &= \frac{V_{\text{IF}}(0.5\pi) - V_{\text{IF}}(1.5\pi)}{2(V_{\text{DC}} - O_B)(M/B)} = \sum_i a_i \frac{1}{1 + (\tau_i \omega)^2}, \\ s &= \frac{V_{\text{IF}}(0) - V_{\text{IF}}(\pi)}{2(V_{\text{DC}} - O_B)(M/B)} = \sum_i a_i \frac{\tau_i \omega}{1 + (\tau_i \omega)^2}, \end{aligned} \quad (\text{S16})$$

where g and s are the horizontal and vertical components (coordinates) of phasors on a phasor plot⁴. From the phasor components, we can obtain the average fluorescence (phase) lifetime of the multi-exponential decay by

$$\bar{\tau} = \frac{s}{g\omega} \approx \frac{\sum_i a_i \tau_i}{\sum_i a_i} = \sum_i a_i \tau_i. \quad (\text{S17})$$

The average fluorescence lifetime alone cannot resolve the heterogeneity of multi-exponential decays, as different fluorophore compositions could result in the same average lifetime measurements. The phasor plot, on the other hand, can be used to resolve the heterogeneity because different fluorophore compositions can alter the phasor components even if the average lifetime might be unaltered. As an example, **Supplementary Fig. 5d** shows that whereas the fluorophore mixtures of different mole ratios of fluorescence and rhodamine B, e.g., 15:1 and 7.5:1, have indistinguishable average lifetimes, their difference in the phasor plot (**Supplementary Fig. 5c**) is evident and can be used to differentiate the two mixtures.

Supplementary Note 3. System calibration.

A fluorescence sample with a known lifetime (e.g., 10^{-3} M coumarin 6 in methanol with a lifetime of 2.30 ns⁵) is required for system calibration. The calibration should be repeated for each different excitation wavelength that will be used. Once the calibration is complete, the system is ready for imaging and no more calibration is required. First, the relations between the phase shifts φ and the phase shifters' bias voltages V_b , i.e., $\varphi(V_b)$, should be calibrated for all four signal paths. Considering a fluorescence sample with a known lifetime $\bar{\tau}$ (e.g., $\bar{\tau} = 2.30$ ns for coumarin 6 in methanol⁵) and assuming that the fluorophore concentration is \bar{c} , for the fluorescence signal, Eq. (S9) becomes

$$\bar{V}_{\text{IF}}(V_b) = \frac{P^2 M \bar{c}}{T} \frac{1}{\sqrt{1 + (\bar{\tau}\omega)^2}} \sin[\varphi(V_b) + \arctan(\bar{\tau}\omega)] + O_M. \quad (\text{S18})$$

By changing the bias voltage V_b and measuring \bar{V}_{IF} , we can obtain a curve, $\bar{V}_{\text{IF}}(V_b)$, with maximal and minimal values:

$$\begin{aligned} \bar{V}_{\text{IF,max}} &= \frac{P^2 M \bar{c}}{T} \frac{1}{\sqrt{1 + (\bar{\tau}\omega)^2}} + O_M, \\ \bar{V}_{\text{IF,min}} &= \frac{P^2 M \bar{c}}{T} \frac{-1}{\sqrt{1 + (\bar{\tau}\omega)^2}} + O_M. \end{aligned} \quad (\text{S19})$$

We then have

$$\begin{aligned} \bar{V}_{\text{IF,max}} + \bar{V}_{\text{IF,min}} &= 2O_M, \\ \bar{V}_{\text{IF,max}} - \bar{V}_{\text{IF,min}} &= \frac{2P^2 M \bar{c}}{T} \frac{1}{\sqrt{1 + (\bar{\tau}\omega)^2}}. \end{aligned} \quad (\text{S20})$$

Thus, from Eq. (S18), we can extract the phase calibration curve, $\varphi(V_b)$, as

$$\begin{aligned}\varphi(V_b) &= \arcsin \left[\frac{\bar{V}_{\text{IF}}(V_b) - O_M}{\frac{P^2 M \bar{c}}{T} \frac{1}{\sqrt{1 + (\bar{\tau}\omega)^2}}} \right] - \arctan(\bar{\tau}\omega) \\ &= \arcsin \left[\frac{2\bar{V}_{\text{IF}}(V_b) - (\bar{V}_{\text{IF,max}} + \bar{V}_{\text{IF,min}})}{\bar{V}_{\text{IF,max}} - \bar{V}_{\text{IF,min}}} \right] - \arctan(\bar{\tau}\omega).\end{aligned}\quad (\text{S21})$$

Therefore, an arbitrary phase shift φ between 0 to 2π can be introduced to the system by applying the corresponding voltage V_b from the calibration curve $\varphi(V_b)$. **Supplementary Fig. 3** shows an example of \bar{V}_{IF} signals acquired from the four mixers' IF ports, as well as the phase calibration curve $\varphi(V_b)$ calculated using Eq. (S21), during the system calibration with a coumarin 6 lifetime standard.

Second, the coefficient M/B used in Eq. (S16) and the offset O_B in Eq. (S4) should be obtained during the calibration process. For the same fluorescence sample with a known lifetime $\bar{\tau}$, the DC signal from the bias tee, Eq. (S4), becomes

$$\bar{V}_{\text{DC}} = \frac{BP^2\bar{c}}{T} + O_B. \quad (\text{S22})$$

The offset O_B can be obtained by turning off the laser beam ($P=0$) while measuring \bar{V}_{DC} .

Therefore, based on Eqs. (S20) and (S22), we get

$$\frac{M}{B} = \frac{\bar{V}_{\text{IF,max}} - \bar{V}_{\text{IF,min}}}{2(\bar{V}_{\text{DC}} - O_B)} \sqrt{1 + (\bar{\tau}\omega)^2}, \quad (\text{S23})$$

which is used for lifetime extraction during each measurement.

Note that in **Supplementary Fig. 3** the four mixers have almost identical electrical properties as the calibration curves overlap with each other; therefore, it is valid to assume that the four mixers have identical conversion losses M and DC offset O_M . However, while the conversion loss M is a design specification and can be guaranteed to be identical for the same type of mixers, there is no guarantee that the DC offset O_M is the same for all mixers¹. Thus, an additional calibration for this DC offset difference may be needed. We add a subscript i to denote the signals from the i -th mixer; the fluorescence signal from the i -th mixer's IF port becomes

$$\bar{V}_{\text{IF}i}(V_b) = \frac{P^2 M \bar{C}}{T} \frac{1}{\sqrt{1 + (\bar{\tau}\omega)^2}} \sin[\varphi(V_b) + \arctan(\bar{\tau}\omega)] + O_{Mi}, \quad (\text{S24})$$

where the i -th DC offset is

$$O_{Mi} = O(P_{\text{RF}}) + d_i. \quad (\text{S25})$$

We found through experiments that $O(P_{\text{RF}})$, as a function of the RF signal's power P_{RF} , was identical for all four mixers, and that the DC offset difference was due to d_i . Therefore, we can compensate for this difference by calibrating the differences among d_i . To do that, we turn off the laser beam ($P = 0$) while measuring $\bar{V}_{\text{IF}i}$ from the four mixers:

$$\begin{aligned} \bar{V}_{\text{IF}1} &= O_{M1} = O(P_{\text{RF}}) + d_1, \\ \bar{V}_{\text{IF}2} &= O_{M2} = O(P_{\text{RF}}) + d_2, \\ \bar{V}_{\text{IF}3} &= O_{M3} = O(P_{\text{RF}}) + d_3, \\ \bar{V}_{\text{IF}4} &= O_{M4} = O(P_{\text{RF}}) + d_4, \end{aligned} \quad (\text{S26})$$

and we define two new calibration parameters, d_{13} and d_{24} , as

$$\begin{aligned} d_{13} &= d_1 - d_3 = \bar{V}_{\text{IF}1} - \bar{V}_{\text{IF}3}, \\ d_{24} &= d_2 - d_4 = \bar{V}_{\text{IF}2} - \bar{V}_{\text{IF}4}. \end{aligned} \quad (\text{S27})$$

After the calibration, the DC offset differences among the mixers can be compensated by including d_{13} and d_{24} in FLIM measurements: Eq. (S12) becomes

$$\tau = \frac{1}{\omega} \frac{V_{\text{IF1}}(0) - V_{\text{IF3}}(\pi) - d_{13}}{V_{\text{IF2}}(0.5\pi) - V_{\text{IF4}}(1.5\pi) - d_{24}}, \quad (\text{S28})$$

and finally, the phasor components [Eq. (S16)] are now

$$g = \frac{V_{\text{IF1}}(0.5\pi) - V_{\text{IF3}}(1.5\pi) - d_{13}}{2(V_{\text{DC}} - O_B)(M/B)},$$

$$s = \frac{V_{\text{IF2}}(0) - V_{\text{IF4}}(\pi) - d_{24}}{2(V_{\text{DC}} - O_B)(M/B)}. \quad (\text{S29})$$

Supplementary Note 4. SNR analysis of instant FLIM.

In this Note, we analyze the SNR performance of instant FLIM and compared it with conventional FD-FLIM methods through Monte Carlo simulations and error-propagation modeling^{6,7}. These FD-FLIM methods differ in the modulation waveforms applied on the excitation beam, and consequently, the detected fluorescence signals are also different, as shown in **Supplementary Fig. 4a**. These differences result in different sensitivity and SNR in lifetime measurements. Here, we use the F -value, or photon economy, a widely used figure of merit in FLIM, to quantify and compare SNRs of FLIM measurements. It is defined as the ratio of the uncertainties in lifetime (τ) and intensity (I) measurements:

$$F = \frac{\sigma_\tau / \tau}{\sigma_I / I} = \sqrt{N_{\text{det}}} \frac{\sigma_\tau}{\tau}, \quad (\text{S30})$$

where we denote $I = N_{\text{det}}$, the number of photons detected in a measurement, and use the fact that N_{det} is Poisson distributed such that $\sigma_I = \sqrt{N_{\text{det}}}$. Since the F -value quantifies the uncertainty in lifetime measurements, a smaller F means that the lifetime is measured more

accurately, hence a higher SNR. Whereas a smaller F is desired, it is limited to $F > 1$ due to shot noise; $F = 1$ only exists in an ideal shot-noise-limited FLIM system.

We use Monte Carlo simulations and analytical error-propagation modeling to acquire the F -values of instant FLIM and conventional FD-FLIM methods. The Monte Carlo simulations are performed by dividing each modulation period T (12.5 ns for 80 MHz modulation) into L time units Δt , where L is sufficiently large (30,000) to keep the probability of detecting multiple photons in a single Δt small, thus preventing the piling-up effect⁸. In each Δt , a random number, r , that is uniformly distributed on $[0, 1]$ is generated and compared with the probability density described by the product of the fluorescence signal $F(t)$ and the time unit Δt . If r is larger than $F(t)\Delta t$, the simulation takes that a fluorescence photon is emitted and recorded by the detector. In the analysis of instant FLIM, $F(t)$ is identical to Eq. (S1), while in other cases, $F(t)$ are analytically calculated by convolving the corresponding excitation signal (**Supplementary Fig. 4a**) with the impulse response function, $f(t)$. A modulation period T is completed after the simulation goes through all Δt in that period; then, another T is simulated identically and the emitted photons are cumulatively recorded by the simulation. For a single lifetime measurement, $N = 2,400$ modulation periods are simulated, and the lifetime τ is calculated based on the FD-FLIM technique in use. This lifetime measurement process is then repeated for 1,000 times in order to obtain the statistical properties (mean and variance) and consequently, the F -value, of the lifetime measurement. A diagram summarizing the Monte Carlo simulation process is shown in **Supplementary Fig. 4b**.

The analytical error-propagation modeling is applicable when the lifetime can be written in the following form:

$$\tau = \frac{U}{V} = \frac{\mu_1 + \sigma_1 Y_1}{\mu_2 + \sigma_2 Y_2} = \frac{\mu_1}{\mu_2} \frac{1 + \delta_1 Y_1}{1 + \delta_2 Y_2}, \quad (\text{S31})$$

where U and V are the random variables used in lifetime calculation with means, μ_1 , μ_2 , standard deviations, σ_1 , σ_2 , and coefficients of variation, $\delta_1 = \sigma_1 / \mu_1$, $\delta_2 = \sigma_2 / \mu_2$; Y_1 and Y_2 are auxiliary random variables with zero mean and unity variance. In practice, $\sigma_1^2 \approx E[U^2]$ and $\sigma_2^2 \approx E[V^2]$ as $E[U]^2$ and $E[V]^2$ are negligible compared to $E[U^2]$ and $E[V^2]$. If the moments of third and higher orders are omitted, Eq. (S31) can be expanded as

$$\tau = \frac{\mu_1}{\mu_2} (1 + \delta_1 Y_1 - \delta_2 Y_2 - \delta_1 \delta_2 Y_1 Y_2 + \delta_2^2 Y_2^2 + \dots). \quad (\text{S32})$$

We then get the expected value of τ as

$$E[\tau] = \frac{\mu_1}{\mu_2} (1 - \rho \delta_1 \delta_2 + \delta_2^2), \quad (\text{S33})$$

where $\rho = E[Y_1 Y_2]$ is the correlation coefficient of U and Y . We also have

$$E[\tau^2] = \left(\frac{\mu_1}{\mu_2} \right)^2 (1 + \delta_1^2 + 3\delta_2^2 - 4\rho \delta_1 \delta_2). \quad (\text{S34})$$

Therefore, the variance of τ can be calculated as

$$\sigma_\tau^2 = E[\tau^2] - E[\tau]^2 = \left(\frac{\mu_1}{\mu_2} \right)^2 (\delta_1^2 + \delta_2^2 - 2\rho \delta_1 \delta_2), \quad (\text{S35})$$

and the F -value can be calculated with Eq. (S30).

Based on the principle of instant FLIM in **Supplementary Note 1**, the fluorescence signal $F(t)$ can be analytically calculated as

$$F(t) = \frac{1}{\tau} \delta_T(t) * \exp\left(-\frac{t}{\tau}\right) = \frac{1}{\tau} \int_0^T \left[\sum_{k=0}^{\infty} \exp\left(-\frac{x+kT}{\tau}\right) \right] \delta_T(t-x) dx = \frac{1}{\tau} \frac{\exp(-t/\tau)}{1 - \exp(-T/\tau)}, \quad (\text{S36})$$

where we scale the excitation power and the fluorophore concentration down to $P=1$ and $c=1$

such that on average only one photon is emitted during a modulation period T , i.e., $\int_0^T F(t) dt = 1$.

Thus, $F(t)$ can be regarded as the probability density function of detecting a photon, and the mathematical expectation of a random variable X related to detecting a photon is

$$E[X] = \int_0^T X F(t) dt. \quad (\text{S37})$$

We denote the random processes corresponding to the outputs of the four mixers [Eq. (S9)] in instant FLIM as X_1 , X_2 , X_3 and X_4 . With Eqs. (S6) and (S8), Eq. (S9) becomes

$$\begin{aligned} V_{\text{IF}}(\varphi) &= \frac{1}{T} \int_0^T v_{\text{IF}}(t, \varphi) dt \\ &= \frac{1}{T} \int_0^T [M \sin(\omega t + \varphi) v_{\text{RF}}(t) + O_M] dt \\ &= \frac{M}{T} \int_0^T \sin(\omega t + \varphi) [F(t) - q_0] dt + O_M \\ &= \frac{M}{T} \int_0^T \sin(\omega t + \varphi) F(t) dt + O_M, \end{aligned} \quad (\text{S38})$$

where we use the fact that $v_{\text{RF}}(t)$ and q_0 are the RF and DC parts of $F(t)$ and therefore $v_{\text{RF}}(t)$

can be written as $v_{\text{RF}}(t) = F(t) - q_0$. With Eqs. (S37) and (S38), we can write the random

processes as

$$\begin{aligned} X_1 &= \frac{M}{T} \sin(\omega t) + O_M, \\ X_2 &= \frac{M}{T} \cos(\omega t) + O_M, \\ X_3 &= -\frac{M}{T} \sin(\omega t) + O_M, \\ X_4 &= -\frac{M}{T} \cos(\omega t) + O_M. \end{aligned} \quad (\text{S39})$$

Then, based on Eq. (S12), the expected lifetime is calculated by

$$\bar{\tau} = \frac{1}{\omega} \frac{N_{\text{det}} E[X_1] - N_{\text{det}} E[X_3]}{N_{\text{det}} E[X_2] - N_{\text{det}} E[X_4]}. \quad (\text{S40})$$

Since Eq. (S12) follows the form of Eq. (S31), we have $U = V_{\text{IF}}(0) - V_{\text{IF}}(\pi)$ and $V = \omega[V_{\text{IF}}(0.5\pi) - V_{\text{IF}}(1.5\pi)]$. Considering that N_{det} photons are detected in a lifetime measurement, based on Eqs. (S3) and (S39), we get the means of U and V as

$$\begin{aligned} \mu_1 &= N_{\text{det}} E[X_1 - X_3] = -2N_{\text{det}} M \text{Im}\{q_1\} = N_{\text{det}} \frac{2M}{T} \frac{\tau\omega}{1 + \tau^2\omega^2}, \\ \mu_2 &= \omega N_{\text{det}} E[X_2 - X_4] = 2\omega N_{\text{det}} M \text{Re}\{q_1\} = \omega N_{\text{det}} \frac{2M}{T} \frac{1}{1 + \tau^2\omega^2}. \end{aligned} \quad (\text{S41})$$

The variances and correlation coefficients of U and V can also be obtained as

$$\begin{aligned} \sigma_1^2 &= N_{\text{det}} E[(X_1 - X_3)^2] = N_{\text{det}} \frac{2M^2}{T} [q_0 - \text{Re}\{q_2\}] = N_{\text{det}} \frac{2M^2}{T^2} \frac{4\tau^2\omega^2}{1 + 4\tau^2\omega^2}, \\ \sigma_2^2 &= \omega^2 N_{\text{det}} E[(X_2 - X_4)^2] = \omega^2 N_{\text{det}} \frac{2M^2}{T} [q_0 + \text{Re}\{q_2\}] = \omega^2 N_{\text{det}} \frac{2M^2}{T^2} \frac{2 + 4\tau^2\omega^2}{1 + 4\tau^2\omega^2}, \\ \rho\sigma_1\sigma_2 &= \omega N_{\text{det}} E[(X_1 - X_3)(X_2 - X_4)] = -\omega N_{\text{det}} \frac{2M^2}{T} \text{Im}\{q_2\} = \omega N_{\text{det}} \frac{2M^2}{T^2} \frac{2\tau\omega}{1 + 4\tau^2\omega^2}. \end{aligned} \quad (\text{S42})$$

Then, from Eq. (S35), the standard deviation of τ is

$$\sigma_\tau = \frac{\mu_1}{\mu_2} \sqrt{\frac{\sigma_1^2}{\mu_1^2} + \frac{\sigma_2^2}{\mu_2^2} - \frac{2\rho\sigma_1\sigma_2}{\mu_1\mu_2}} = \tau(1 + \tau^2\omega^2) \sqrt{\frac{1 + 2\tau^2\omega^2}{N_{\text{det}}(1 + 4\tau^2\omega^2)}}. \quad (\text{S43})$$

Consequently, we get the F -value of instant FLIM as

$$F = \sqrt{N_{\text{det}}} \frac{\sigma_\tau}{\tau} = (1 + \tau^2\omega^2) \sqrt{\frac{1 + 2\tau^2\omega^2}{1 + 4\tau^2\omega^2}}, \quad (\text{S44})$$

which is identical to the F -value of a two-photon (2P) FD-FLIM when the excitation is modulated as a Dirac comb⁷; this is expected as instant FLIM uses a femtosecond pulse excitation in a 12.5 ns (80 MHz) modulation period, which can be seen as a Dirac comb.

We compare the SNR performances of instant FLIM and conventional FD-FLIM methods⁷, including 2P FD-FLIM with sinusoidal (1.0, 0.5 modulation degrees) and periodic square wave (0.2, 0.5 duty cycles) modulations, as well as one-photon (1P) FD-FLIM with sinusoidal modulation (1.0 modulation degree), by plotting their simulated (symbols) and analytical (curves) F -values in **Supplementary Fig. 4c**. Since the F -value is only dependent on the product of the modulation frequency and the fluorescence lifetime⁶, i.e., $\omega\tau$, and the modulation frequency for instant FLIM is fixed at 80 MHz, for a fair comparison, we fix the modulation frequency of all the methods to 80 MHz and vary the lifetime from 0 to 4.5 ns when we investigate the F -values. The analytical results are in good agreement with the ones obtained from Monte Carlo simulations. Our instant FLIM method has the smallest F -value ($F = 1$), which is the shot noise limit and the best possible SNR performance a FLIM method can have. In comparison, the 2P sinusoidal (1.0, 0.5 modulation degrees) and periodic square wave (0.2, 0.5 duty cycles) modulations have their best SNR performances at $F = 2.62$, $F = 4.07$, $F = 1.44$, and $F = 2.89$, respectively; the conventional 1P sinusoidal (1.0 modulation degree) case has its best F -value at $F = 3.67$. To illustrate the SNR difference among these FD-FLIM methods, we select four targeted lifetime values (0.375 ns, 1.625 ns, 2.875 ns, and 4.125 ns) and plot the traces of the 1,000 lifetime measurements using different FD-FLIM methods from the Monte Carlo simulations (**Supplementary Fig. 4d**). A lifetime histogram and the standard deviation (σ_τ) of the 1,000 lifetime measurements are plotted next to each trace. In all four cases, the instant FLIM measurements have the smallest σ_τ compared to conventional FD-FLIM methods. In summary, through Monte Carlo simulations and error-propagating analysis, instant FLIM has been demonstrated to be superior in SNR performance compared with conventional FD-FLIM techniques; in some cases, instant FLIM can approach the shot noise limit ($F = 1$), the best

possible SNR performance of a FLIM measurement. This is achieved by the efficient utilization of the 80 MHz femtosecond pulsed laser in instant FLIM.

Supplementary Note 5. Super-resolution instant FLIM with GSOS.

In this Note, we show that the instant FLIM system can be used to generate super-resolution FLIM images based on the recently demonstrated generalized stepwise optical saturation (GSOS) technique⁹. By linear combining M FLIM images obtained with different excitation powers in the complex domain, a new FLIM image with a \sqrt{M} -fold increase in spatial resolution can be obtained. Because the linear combination in GSOS is applied to the complex Fourier coefficients, q_k , of the fluorescence, $F(t)$, we rewrite Eq. (S5) such that q_k is explicitly shown in the equation:

$$v_{\text{RF}}(t) = 2 \sum_{k \in \mathbb{Z}^+} \text{Re}\{q_k \exp(ik\omega t)\} = \sum_{k \in \mathbb{Z}^+} 2 \text{Re}\{q_k\} \cos(k\omega t) - 2 \text{Im}\{q_k\} \sin(k\omega t). \quad (\text{S45})$$

Following the analog signal processing in instant FLIM, the output signals of the mixers [Eq. (S9)] become

$$\begin{aligned} V_{\text{IF}}(\varphi) &= \frac{1}{T} \int_0^T v_{\text{IF}}(t, \varphi) dt \\ &= \frac{1}{T} \int_0^T [M \sin(\omega t + \varphi) v_{\text{RF}}(t) + O_M] dt \\ &= \frac{M}{T} [\text{Re}\{q_1\} \sin(\varphi) - \text{Im}\{q_1\} \cos(\varphi)] + O_M. \end{aligned} \quad (\text{S46})$$

Consequently, after introducing the four phase shifts, the measured mixer outputs [Eq. (S10)] are

$$\begin{aligned}
 V_{\text{IF}}(0) &= -\frac{M}{T} \text{Im}\{q_1\} + O_M, \\
 V_{\text{IF}}(0.5\pi) &= \frac{M}{T} \text{Re}\{q_1\} + O_M, \\
 V_{\text{IF}}(\pi) &= \frac{M}{T} \text{Im}\{q_1\} + O_M, \\
 V_{\text{IF}}(1.5\pi) &= -\frac{M}{T} \text{Re}\{q_1\} + O_M.
 \end{aligned} \tag{S47}$$

Then, the differences among them [Eq. (S11)] are directly proportional to the real and imaginary parts of the Fourier coefficient:

$$\begin{aligned}
 V_{\text{IF}}(\pi) - V_{\text{IF}}(0) &= \frac{2M}{T} \text{Im}\{q_1\}, \\
 V_{\text{IF}}(0.5\pi) - V_{\text{IF}}(1.5\pi) &= \frac{2M}{T} \text{Re}\{q_1\}.
 \end{aligned} \tag{S48}$$

Therefore, the magnitude and phase of the complex Fourier coefficient, q_1 , can be extracted as

$$\begin{aligned}
 |q_1| &\approx \sqrt{[V_{\text{IF}}(\pi) - V_{\text{IF}}(0)]^2 + [V_{\text{IF}}(0.5\pi) - V_{\text{IF}}(1.5\pi)]^2}, \\
 \angle q_1 &= \arctan \left[\frac{V_{\text{IF}}(\pi) - V_{\text{IF}}(0)}{V_{\text{IF}}(0.5\pi) - V_{\text{IF}}(1.5\pi)} \right],
 \end{aligned} \tag{S49}$$

which are then combined as a complex value, $q_1 = |q_1| \exp(i\angle q_1)$.

In GSOS with M steps (M-GSOS), the measurement is repeated for M times with M different excitation powers, $I_{01}, I_{02}, \dots, I_{0M}$, where $I_{01} < I_{02} < \dots < I_{0M}$. Hence M images consisting of these complex Fourier coefficients, $q_{1,1}, q_{1,2}, \dots, q_{1,M}$, are obtained based on the measurements described above [Eqs. (S47)-(S49)]. The GSOS linear combination is then applied to these complex images,

$$q_{1,\text{M-GSOS}} = \sum_{m=1}^M c_m q_{1,m}, \tag{S50}$$

where the linear combination coefficients, c_m , are calculated based on the excitation powers,

$I_{01}, I_{02}, \dots, I_{0M}$. Here, we give the general expression to calculate c_m :

$$c_m = \begin{cases} 1 & \text{if } m = 1, \\ -\frac{I_{01}^N}{I_{02}^N}, & \text{if } m = 2 \text{ and } M = 2, \\ (-1)^{M-1} \frac{I_{01}^N}{I_{0m}^N} \prod_{j=2, j \neq m}^M \frac{I_{01}^N - I_{0j}^N}{I_{0j}^N - I_{0m}^N} & \text{otherwise,} \end{cases} \quad (\text{S51})$$

where N is the number of excitation photons needed for a fluorophore to emit one photon ($N=1$ for 1PEF, $N=2$ for 2PEF). The result of the GSOS linear combination is a new image ($q_{1,M\text{-GSOS}}$) with complex pixel values, where its magnitude, $|q_{1,M\text{-GSOS}}|$, is a super-resolution image with a \sqrt{M} -fold increase in resolution over the diffraction limit, and its phase, $\angle q_{1,M\text{-GSOS}}$, is identical to that of the original Fourier coefficient, $\angle q_1$ ^{9,10}. From the phase, a fluorescence lifetime image can be obtained by

$$\tau = -\frac{1}{\omega} \tan(\angle q_{1,M\text{-GSOS}}) = -\frac{1}{\omega} \tan(\angle q_1). \quad (\text{S52})$$

As a result, by linear combining M complex images obtained with an instant FLIM system using the GSOS principle, we can obtain a super-resolution FLIM image where its intensity, $|q_{1,M\text{-GSOS}}|$, is enhanced by a factor of \sqrt{M} and its lifetime information, $\tau = -\tan(\angle q_{1,M\text{-GSOS}}) / \omega$, is preserved.

Whereas GSOS was utilized to generate 2D super-resolution FLIM images of fixed cells⁹ (**Fig. 1g**), it has not been demonstrated in 3D due to the excessive time required to generate multiple 3D FLIM stacks under different excitation powers using conventional methods. In this work, however, no extra time consumption is needed to generate FLIM images due to the

multiplexing analog signal processing in instant FLIM. Therefore, instant FLIM system can be used to generate super-resolution 3D FLIM stacks. **Supplementary Fig. 6** shows a side-by-side comparison between a diffraction-limited (DL) and a super-resolution (two-step GSOS) 3D FLIM stacks of a fixed mouse brain (**Methods**). The DL stack was acquired with an instant FLIM system at an excitation power of 12.31 mW. The two-step GSOS stack, on the other hand, was generated by linear combining two DL instant FLIM stacks, $q_{1,1}$ and $q_{1,2}$, measured at $I_1 = 12.31$ mW and $I_2 = 13.44$ mW, respectively. The GSOS linear combination coefficients were calculated according to Eq. (S51) ($N = 2$ for 2PEF): $c_1 = 1$ and $c_2 = -I_{01}^2 / I_{02}^2 = -0.8389$. The two-step GSOS stack, $q_{1,2\text{-GSOS}}$, was then generated based on Eq. (S50), i.e., $q_{1,2\text{-GSOS}} = c_1 q_{1,1} + c_2 q_{1,2} = q_{1,1} - 0.8389 q_{1,2}$; its intensity, $|q_{1,2\text{-GSOS}}|$, and fluorescence lifetime, $\tau = -\tan(\angle q_{1,2\text{-GSOS}}) / \omega$, are plotted as brightness and hue, respectively, to construct the 3D FLIM stack. The resolution improvement of the GSOS stack compared to the DL stack can be seen in **Supplementary Fig. 6b,d**, where the white arrows denote features that are better resolved in the GSOS stack.

Supplementary Note 6. Instant FLIM with adaptive optics.

Adaptive optics (AO) can be employed in instant FLIM to reduce the optical aberrations induced by the imaging system or the sample, and potentially improve the imaging quality and extend the penetration depth¹¹. We implemented AO as an optional module in instant FLIM by introducing a deformable mirror (Thorlabs DMP40-P01) to the setup. To reduce the system complexity and cost, we employed sensorless AO, in which a wavefront sensor was not required, and indirect wavefront sensing based on an optimization metric was used. Using the optimization algorithms

described in this Note, the AO module iteratively adjusts the parameters of the deformable mirror to improve the image-based optimization metric.

Depending on the user's choice in the Instant-FLIM-Control program (**Supplementary Protocol 1**), the optimization metric, V , can be the mean pixel value or the normalized variance of the image, where the normalized variance is defined as the variance of all the pixel values divided by the square of the mean pixel value¹². We employed Zernike modes to describe the optical aberrations as well as the aberration compensation applied to the deformable mirror. The optimization algorithms are performed in an N -dimensional aberration space generated by a base:

$$\zeta = [z_1, z_2, \dots, z_N]^T, \quad (\text{S53})$$

where z_1, z_2, \dots, z_N are Zernike polynomials. The deformable mirror (Thorlabs DMP40-P01) we used is a low-cost wavefront correction device and it supports up to 12 Zernike modes (Z_2^{-2} , Z_2^0 , Z_2^2 , Z_3^{-3} , Z_3^{-1} , Z_3^1 , Z_3^3 , Z_4^{-4} , Z_4^{-2} , Z_4^0 , Z_4^2 , Z_4^4) in the optimization. The aberration compensation, Φ , can then be described in the aberration space spanned by ζ :

$$\Phi = \alpha^T \zeta = \sum_{n=1}^N a_n z_n, \quad (\text{S54})$$

where

$$\alpha = [a_1, a_2, \dots, a_N]^T \quad (\text{S55})$$

are the Zernike coefficients in which a_j represents the contribution of z_j to Φ . In practice, an optimization algorithm iteratively monitors the image-based metric V and updates the Zernike coefficients α that control the wavefront shaping elements (mirror segments) on the deformable

mirror; after multiple iterations, if the AO optimization is successful, the metric V will be increased and the imaging quality will be improved.

In the Instant-FLIM-Control program, we use three AO algorithms to optimize V and the imaging quality. The first one is a simple max search algorithm that sequentially searches through each Zernike coefficient, from a_1 to a_N , until a maximized V is found for each one of them. For example, to find the optimal value for a_j , the algorithm keeps all the other Zernike coefficients unaltered while changing a_j from -1 to 1 with a step size defined by the user, e.g., 0.2. This is valid due to the orthogonality of the Zernike modes. The optimal a_j is found at the value where V is maximized from $-1 < a_j < 1$. This algorithm is easy and straightforward, but it is time-consuming: for a step size of 0.2, a full optimization of 12 Zernike modes requires the acquisition of 120 raw images. However, this is also the most robust and reliable algorithm, as it guarantees that a global optimum or its proximity can be found, whereas the other algorithms are likely to find a local optimum.

The second algorithm is a quadratic search algorithm¹³ which approximates the metric V of the aberration Φ as a quadratic function of the Zernike coefficients α :

$$V(\Phi) \approx V_0 - \sum_{n=1}^N c_n \alpha_n^2, \quad (\text{S56})$$

where V_0 and c_n are constants and the metric has a paraboloidal shape around its maximum. The goal of the optimization algorithm is to find the coordinates of α that maximizes V . This

process can be decomposed into N independent one-dimensional parabolical optimization problem for each Zernike coefficient a_n , as Eq. (S56) can be written as

$$V(\Phi) \approx \left(V_0 - \sum_{l \neq n}^N c_l a_l^2 \right) - c_n a_n^2. \quad (\text{S57})$$

The optimal a_n that maximizes V can then be calculated by three measurements of V , i.e., $V(\Phi_0)$, $V(\Phi_0 + bz_n)$, and $V(\Phi_0 - bz_n)$ corresponding to the a_n values of a_{n0} , $a_{n0} + b$, and $a_{n0} - b$, respectively, where Φ_0 is the initial aberration, a_{n0} is the initial value of a_n ($a_{n0} = 0$ by default), and b is the bias amplitude used to search the parabolic maximum. With the three metrics obtained from the three raw images, the optimal a_n , i.e., a_{nx} , can be estimated with parabolic maximization as

$$a_{nx} = a_{n0} + \frac{V(\Phi_0 + bz_n) - V(\Phi_0 - bz_n)}{2V(\Phi_0) - V(\Phi_0 + bz_n) - V(\Phi_0 - bz_n)} \frac{b}{2}. \quad (\text{S58})$$

In the algorithm, this one-dimensional optimization process is repeated for N times to calculate the optimal Zernike coefficients $a_{1x}, a_{2x}, \dots, a_{Nx}$ that jointly maximizes V . Whereas each process requires three measurements, the metric for the initial image $V(\Phi_0)$ is common; therefore, to correct for N Zernike coefficients, the algorithm merely requires $2N + 1$ raw images. For our deformable mirror supporting 12 Zernike modes, the optimization needs only 25 raw images. Compared to the other AO optimization algorithms, the quadratic search one is the fastest and requires the least number of raw images to be captured. However, it is not always reliable as the approximation assumption in Eq. (S56) is only accurate for small aberration amplitudes, which may not be satisfied in practice¹⁴. Therefore, this algorithm is recommended only if the speed is an essential requirement for AO optimization.

The third algorithm in the program is based on the stochastic parallel gradient descent (SPGD) method^{15,16}. In each SPGD iteration, after the metric V is acquired from a raw image, the Zernike coefficients in α are perturbed in parallel by a small non-zero stochastic value. In our program, the value is randomly chosen from $[-0.05, -0.025, 0.025, 0.05]$. During the m -th iteration, the Zernike coefficients applied to the $m+1$ -th iteration is calculated as

$$\alpha^{(m+1)} = \alpha^{(m)} - \eta[V(\Phi + \delta^T \zeta) - V(\Phi)]\delta, \quad (\text{S59})$$

where the superscripts in brackets are the indices of the iteration, η is the learning rate, Φ is the aberration before the iteration, ζ is the Zernike base described in Eq. (S53), and δ is an array consisting of the non-zero stochastic values. The learning rate η is negative in our case (-0.01 by default) as the optimization is to maximize V . If η is chosen properly, the metric V will be increased after each iteration. The algorithm is stopped when a maximal V is found or the specified steps of iterations are reached. Compared to the previous algorithms, the SPGD method updates the Zernike coefficients in parallel and it could acquire the optimal coefficients more accurately. However, due to the stochastic nature of the method, the algorithm usually takes much more iterations, hence imaging time, than the other methods, and it could also easily fall into a local maximum. As a complement to the other algorithms, the SPGD method is recommended when a high precision is preferred in determining the optimal Zernike coefficients.

To demonstrate the performance of instant FLIM when the AO module is added, we acquired through-skull 3D FLIM stacks of the intact brain in a living mouse (**Methods**) with and without AO. We used the simple max search algorithm for the AO optimization. With AO, the instant FLIM system was able to generate 3D intensity, lifetime, and phasor ROI-labeled stacks of the living mouse brain, through the skull, with a penetration depth up to $\sim 300 \mu\text{m}$ (**Supplementary**

Fig. 10a). Note that the excitation power of the laser was gradually increased from 8.53 mW to 21.13 mW during the imaging; the penetration depth limit was achieved when further increasing the power could not increase the signal level. We then imaged the animal with the same imaging condition but without the AO module. Specifically, we added a folding mirror in front of the AO module to reflect the laser beam directly into the two-photon microscope. As shown in **Supplementary Fig. 10b**, when the AO module was not used, we could only achieve a penetration depth of ~ 130 μm . In comparison, the penetration depth for instant FLIM with a well-optimized AO module (~ 300 μm) was more than double of that without AO.

Supplementary Table 1. Parts and price list for instant FLIM.

A table showing the budget of all the components necessary for instant FLIM (< 2,500 USD)

Vendor	Part Number	Quantity	Unit Price	Total Price	Description	Link
Instant FLIM Components						
ThorLabs	EF502	4	\$69.86	\$279.44	Low Pass Filter (LPF), DC-100 kHz, BNC Connector	https://www.thorlabs.com/thorproduct.cfm?partnumber=EF502
Mini-Circuits	BLP-90+	2	\$35.45	\$70.90	Low Pass Filter (LPF), DC-81 MHz, BNC Connector	https://www.minicircuits.com/WebStore/dashboard.html?model=BLP-90%2B
Mini-Circuits	ZX60-P103LN+	6	\$69.95	\$419.70	Low Noise Amplifier (LNA), 50-3000 MHz, SMA Connector	https://www.minicircuits.com/WebStore/dashboard.html?model=ZX60-P103LN%2B
Mini-Circuits	ZSC-4-3+	2	\$56.95	\$113.90	4-Way Power Splitter, 0.25-250 MHz, BNC Connector	https://www.minicircuits.com/WebStore/dashboard.html?model=ZSC-4-3%2B
Mini-Circuits	JSPHS-150+	8	\$34.95	\$279.60	Phase Shifter (PS), 100-150 MHz, Surface Mount	https://www.minicircuits.com/WebStore/dashboard.html?model=JSPHS-150%2B
Mini-Circuits	TB-152+	8	\$29.95	\$239.60	Board to Surface Mount Phase Shifters, SMA Connector	https://www.minicircuits.com/WebStore/dashboard.html?model=TB-152%2B
Mini-Circuits	ZAD-3H+	4	\$50.95	\$203.80	Level 17 Frequency Mixer, 0.05-200 MHz, BNC Connector	https://www.minicircuits.com/WebStore/dashboard.html?model=ZAD-3H%2B
Mini-Circuits	ZFBT-282-1.5A+	1	\$59.95	\$59.95	Bias Tee, 10-2800 MHz, SMA Connector	https://www.minicircuits.com/WebStore/dashboard.html?model=ZFBT-282-1.5A%2B
<i>Instant FLIM Components Total Cost:</i>				<i>\$1,666.89</i>		
Cables and Adapters						
Mini-Circuits	141-24BM+	4	\$19.45	\$77.80	24" Coaxial Cable, BNC Connector	https://www.minicircuits.com/WebStore/dashboard.html?model=141-24BM%2B
Mini-Circuits	141-18BM+	18	\$18.45	\$332.10	18" Coaxial Cable, BNC Connector	https://www.minicircuits.com/WebStore/dashboard.html?model=141-18BM%2B
Mini-Circuits	086-6BM+	6	\$15.75	\$94.50	6" Coaxial Cable, BNC Connector	https://www.minicircuits.com/WebStore/dashboard.html?model=086-6BM%2B
Mini-Circuits	086-2SM+	8	\$10.75	\$86.00	2" Coaxial Cable, BNC Connector	https://www.minicircuits.com/WebStore/dashboard.html?model=086-2SM%2B
Mini-Circuits	SF-BF50+	6	\$3.95	\$23.70	SMA-F to BNC-F Adapter	https://www.minicircuits.com/WebStore/dashboard.html?model=SF-BF50%2B
Mini-Circuits	SM-BF50+	12	\$3.95	\$47.40	SMA-M to BNC-F Adapter	https://www.minicircuits.com/WebStore/dashboard.html?model=SM-BF50%2B
Mini-Circuits	SM-BM50+	6	\$3.95	\$23.70	SMA-M to BNC-M Adapter	https://www.minicircuits.com/WebStore/dashboard.html?model=SM-BM50%2B
<i>Cables and Adapters Total Cost:</i>				<i>\$685.20</i>	<i>Note: Cheaper Cables and Adapters Available from Other Vendors</i>	

Supplementary Table 2. Acquisition parameters for all data.

A table showing the acquisition parameters for all data used in this work.

Figure	Sample	Dwell Time (μs)	Excitation Wavelength (nm)	Excitation Power (mW)	Image Size (Pixel/Voxel)	Pixel Size (nm)	Voxel Depth (μm)	Time Interval (s)	Notes
Figs. 1b	Fixed BPAAE cells, mitochondria labeled with MitoTracker Red, F-actin with Alexa Fluor 488, nuclei with DAPI	12 (Average x20)	800	8.95	560 x 560	100	N/A	N/A	2D fixed sample
Figs. 1g	Fixed BPAAE cells, mitochondria labeled with MitoTracker Red, F-actin with Alexa Fluor 488, nuclei with DAPI	12 (Average x20)	800	Step1: 8.95 Step2: 10.61	560 x 560	100	N/A	N/A	2D fixed sample; two-step GSOS
Fig. 1e	Fixed Cx3cr1-GFP/+ mouse brain, microglia labeled with EGFP, blood vessel injected with Dextran 594	12	920	8.53 to 21.13	540 x 540 x 350	200	0.5	N/A	3D fixed sample
Fig. 2b, left	Live <i>Tg(pul:gfp)</i> zebrafish, microglia labeled with EGFP	12	920	12.31	360 x 360 x 60	200	1	N/A	3D live animal
Fig. 2b, right	Live <i>Tg(pul:gfp)</i> zebrafish, microglia labeled with EGFP	12	800	18.43	360 x 360 x 30	300	1	N/A	3D live animal
Fig. 2f	Live <i>Tg(pul:gfp)</i> zebrafish, microglia labeled with EGFP	12	920	12.31	360 x 360 x 30 x 48	300	1	900	4D live animal
Fig. 2i, 2k	Live Cx3cr1-GFP/+ mouse, microglia labeled with EGFP, blood vessel injected with Texas Red-Dextran	12	920	12.31	300 x 300 x 20 x 3	200	2	120	4D live animal
Fig. 3b, S13	Live <i>Tg(pul:gfp)</i> zebrafish, microglia labeled with EGFP, injury induced by 800 nm laser at 43.50 mW for 1 s	12	920	11.05	560 x 560 x 30 x 49	300	1.5	900	4D live animal
Fig. 3g, S8	Live <i>Tg(pul:gfp)</i> zebrafish, microglia labeled with EGFP, injury induced by 800 nm laser at 43.50 mW for 20 s	12	920	11.05	560 x 560 x 30 x 9	300	1.5	900	4D live animal
Fig. 3i, 3k	Live Cx3cr1-GFP/+ mouse, microglia labeled with EGFP, blood vessel injected with Texas Red-Dextran, injury induced by 800 nm laser at 43.50 mW for 120 s	12	920	12.31	300 x 300 x 20 x 24	200	2	120	4D live animal
Fig. S5b	Lifetime standards, including coumarin 6, fluorescein, and rhodamine B	12	800	6.64 to 9.59	360 x 360	200	N/A	N/A	2D fluorophore solution
Fig. S5d	Mixture of fluorescein and rhodamine B	12	800	9.59	360 x 360	200	N/A	N/A	2D fluorophore solution
Fig. S6a	Fixed Cx3cr1-GFP/+ mouse brain, microglia labeled with EGFP, blood vessel injected with Dextran 594	12 (Average x5)	920	Step1: 12.31 Step2: 13.44	540 x 540 x 118	150	0.5	N/A	3D fixed sample; two-step GSOS
Fig. S6c	Fixed Cx3cr1-GFP/+ mouse brain, microglia labeled with EGFP, blood vessel injected with Dextran 594	12 (Average x10)	920	Step1: 12.31 Step2: 13.44	540 x 540 x 57	150	0.5	N/A	3D fixed sample; two-step GSOS
Fig. S7	Live MDA-MB-231-EGFP cells imaged at a temperature between 18.1 and 46.7 °C	12 (Average x10)	920	8.53	360 x 360	200	N/A	N/A	2D live cells
Fig. S9b	Live Cx3cr1-GFP/+ mouse, microglia labeled with EGFP, blood vessel injected with Texas Red-Dextran	12	920	12.31	520 x 520 x 20 x 10	200	2	120	4D live animal
Fig. S9e	Live Cx3cr1-GFP/+ mouse, microglia labeled with EGFP, blood vessel injected with Texas Red-Dextran, injury induced by 800 nm laser at 43.50 mW for 120 s	12	920	12.31	520 x 520 x 20 x 29	200	2	120	4D live animal
Fig. S10	Live Cx3cr1-GFP/+ mouse, microglia labeled with EGFP, blood vessel injected with Texas Red-Dextran	12	920	8.53 to 21.13	360 x 360 x 600 360 x 360 x 260	300	0.5	N/A	3D live animal
Fig. S11	Live Cx3cr1-GFP/+ mouse, microglia labeled with EGFP, blood vessel injected with Texas Red-Dextran, injury induced by 800 nm laser at 43.50 mW for 120 s	12	920	12.31	300 x 300 x 20 x 8	200	2	120	4D live animal
Fig. S12	Live Cx3cr1-GFP/+ mouse, microglia labeled with EGFP, blood vessel injected with Texas Red-Dextran, injury induced by 800 nm laser at 43.50 mW for 120 s	12	920	12.31	530 x 530 x 20 x 14	200	2	120	4D live animal

Supplementary Video 1

Slices of 3D two-photon intensity, composite lifetime, and phasor ROI-labeled stacks of a fixed Cx3cr1-GFP/+ mouse brain (microglia labeled with EGFP; blood vessel injected with Dextran 594) measured with an instant FLIM system. The slices were captured from the surface to the depth of 175 μm inside the tissue. Maximized z-projections and 3D reconstructions of the same stacks are shown in **Fig. 1e**, where the color bar representing the lifetime values in the composite lifetime slices are also shown. The ROIs on the phasor plot labeling the phasor stacks can be found in **Fig. 1d**.

Supplementary Video 2

Slices of composite 3D lifetime stacks of a fixed Cx3cr1-GFP/+ mouse brain (microglia labeled with EGFP; blood vessel injected with Dextran 594) captured by an instant FLIM system conventionally (left) and combined with the two-step GSOS technique (right), identical to the ones in **Supplementary Fig. 6**. The slices were captured from the surface to the depth of 59 μm inside the tissue. The conventional stack was imaged at a power of 12.31 mW, and the GSOS stack was generated by linear combining two stacks imaged at 12.31 mW and 13.44 mW, respectively.

Supplementary Video 3

Reconstructed 3D two-photon fluorescence intensity, lifetime, and phasor ROI-labeled stacks of a living Cx3cr1-GFP/+ mouse brain acquired with an instant FLIM system combined with the deformable mirror-based adaptive optics module (related to **Supplementary Fig. 10a**). The stacks were captured from the surface of the skull to 300 μm inside the brain. The excitation

power was gradually increased from 8.53 mW to 21.13 mW to compensate for the signal loss as the imaging depth increased.

Supplementary Video 4

4D reconstruction of the two-photon intensity, composite lifetime, and phasor ROI-labeled stacks of the microglia in a living *Tg(pul:gfp)* zebrafish brain at 4dpf acquired with an instant FLIM system. The time-lapse 3D stacks were captured every 15 minutes and the totally imaging session was 12 hours long. A laser injury was induced at $t = 30$ minutes by an 800 nm laser at 43.50 mW lasting for 1 s. The dynamics as well as the lifetime changes of the zebrafish microglia responding to the injury can be observed with the 4D movie.

Supplementary Video 5

4D reconstruction of the two-photon intensity, composite lifetime, and phasor ROI-labeled stacks of the microglia in a living *Cx3cr1-GFP/+* mouse brain acquired with an instant FLIM system. The time-lapse 3D stacks were captured every 2 minutes and the totally imaging session took 56 minutes. A laser injury was induced at $t = 4$ minutes by an 800 nm laser at 43.50 mW lasting for 120 s. The dynamics and the lifetime changes of the mouse microglia responding to the injury can be seen with the 4D movie.

Supplementary Video 6

Maximized z-projections of the 3D time-lapse intensity and lifetime stacks as well as the phasor plots for each time point of the microglia in a living *Cx3cr1-GFP/+* mouse brain. The stacks were acquired with an instant FLIM system and they are related to **Supplementary Fig. 11**. A

laser injury was induced right before $t = 0$ by an 800 nm laser with a power of 43.50 mW lasting for 120 s. The stacks were captured at 8 different injury sites from one of two mice.

Supplementary Video 7

Reconstructed time-lapse 3D stacks of the microglia in a living Cx3cr1-GFP/+ mouse brain labeled with the phasor ROIs in **Supplementary Fig. 12a**. A laser injury was induced right before $t = 0$ by an 800 nm laser with a power of 43.50 mW lasting for 120 s. The cellular structures segmented by the ROIs all responded to the injury.

Supplementary Video 8

Reconstructed time-lapse 3D stacks of the microglia in a living Cx3cr1-GFP/+ mouse brain labeled with the phasor clusters in **Supplementary Fig. 12b** generated by the K-means clustering algorithm ($K=5$). A laser injury was induced right before $t = 0$ by an 800 nm laser with a power of 43.50 mW lasting for 120 s. The cellular structures segmented by the ROIs all responded to the injury.

Supplementary Video 9

4D reconstruction of the surface rendered lifetime stack obtained by decomposing the composite lifetime stack (microglia in a living zebrafish brain in **Supplementary Video 4**) in the RGB color space, independently surface rendering the decomposed RGB components, and recombining the rendered R, G, and B surfaces. With the surface rendering, the cellular structures involved in the laser-induced microglia response are better differentiated compared to the ones in the lifetime stack.

Supplementary Protocol 1. Instant-FLIM-Control LabView program.

A protocol of the open-source LabView program to control the instant FLIM system

Supplementary Protocol 2. Instant-FLIM-Analysis Matlab program.

A protocol of the open-source Matlab program to analyze the instant FLIM imaging data

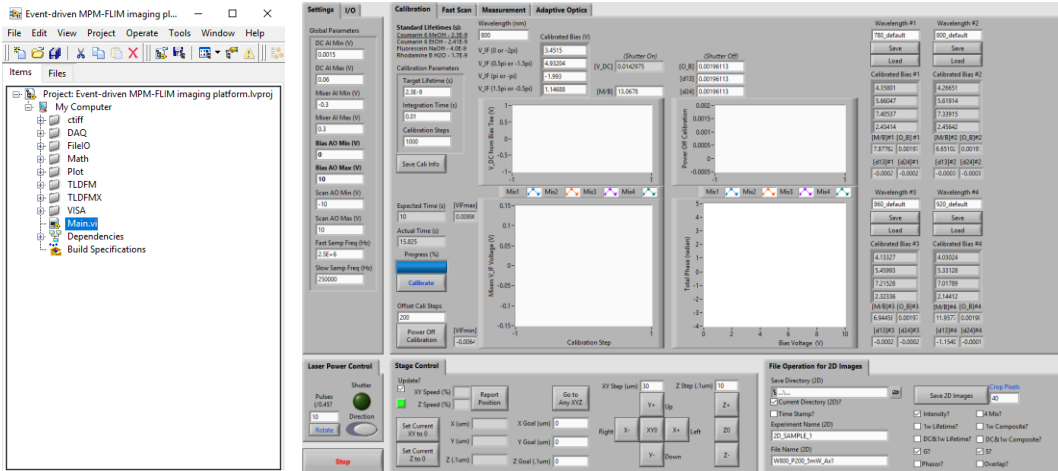
References

1. Kurtz, S. R. *Mixers as Phase Detectors Most. Edge, The Communications* (2014).
2. Stringari, C. *et al.* Phasor approach to fluorescence lifetime microscopy distinguishes different metabolic states of germ cells in a live tissue. *Proc. Natl. Acad. Sci.* **108**, 13582–13587 (2011).
3. Berberan-Santos, M. N. Phasor plots of luminescence decay functions. *Chem. Phys.* **449**, 23–33 (2015).
4. Ranjit, S., Malacrida, L., Jameson, D. M. & Gratton, E. Fit-free analysis of fluorescence lifetime imaging data using the phasor approach. *Nat. Protoc.* **13**, 1979–2004 (2018).
5. Kristoffersen, A. S., Erga, S. R., Hamre, B. & Frette, Ø. Testing Fluorescence Lifetime Standards using Two-Photon Excitation and Time-Domain Instrumentation: Rhodamine B, Coumarin 6 and Lucifer Yellow. *J. Fluoresc.* **24**, 1015–1024 (2014).
6. Philip, J. & Carlsson, K. Theoretical investigation of the signal-to-noise ratio in fluorescence lifetime imaging. *Journal of the Optical Society of America A* **20**, 368–379 (2003).
7. Zhang, Y., Khan, A. A., Vigil, G. D. & Howard, S. S. Investigation of signal-to-noise ratio in frequency-domain multiphoton fluorescence lifetime imaging microscopy. *J. Opt. Soc. Am. A* **33**, B1 (2016).
8. Li, D.-U., Bonnist, E., Renshaw, D. & Henderson, R. On-chip, time-correlated, fluorescence lifetime extraction algorithms and error analysis. *J. Opt. Soc. Am. A* **25**, 1190 (2008).
9. Zhang, Y., Benirschke, D., Abdalsalam, O. & Howard, S. S. Generalized stepwise optical saturation enables super-resolution fluorescence lifetime imaging microscopy. *Biomed.*

- Opt. Express* **9**, 4077 (2018).
10. Zhang, Y. *et al.* Super-resolution fluorescence microscopy by stepwise optical saturation. *Biomed. Opt. Express* **9**, 1613 (2018).
 11. Ji, N. Adaptive optical fluorescence microscopy. *Nat. Methods* **14**, 374–380 (2017).
 12. Alexander, N. S. *et al.* Image registration and averaging of low laser power two-photon fluorescence images of mouse retina. *Biomed. Opt. Express* **7**, 2671 (2016).
 13. Debarre, D., Booth, M. J. & Wilson, T. Image based adaptive optics through optimisation of low spatial frequencies. *Opt. Express* **15**, 8176 (2007).
 14. Pozzi, P., Soloviev, O., Wilding, D., Vdovin, G. & Verhaegen, M. Optimal model-based sensorless adaptive optics for epifluorescence microscopy. *PLoS One* **13**, e0194523 (2018).
 15. Vorontsov, M. A. & Sivokon, V. P. Stochastic parallel-gradient-descent technique for high-resolution wave-front phase-distortion correction. *J. Opt. Soc. Am. A* **15**, 2745 (1998).
 16. Palczewska, G. *et al.* Noninvasive two-photon microscopy imaging of mouse retina and retinal pigment epithelium through the pupil of the eye. *Nat. Med.* **20**, 785–789 (2014).

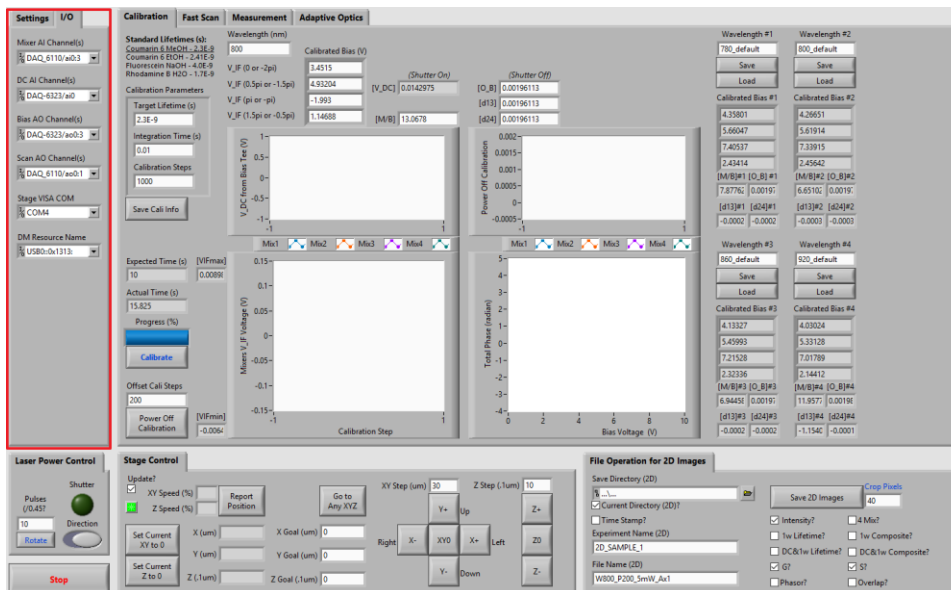
<https://github.com/yzhang34/Instant-FLIM-Control.git>

- Open the project “Event-driven MPM-FLIM imaging platform.lvproj” in LabView and run the file “Main.vi” to execute the program:



3. Hardware Configuration

This step is to establish the connection between the LabView software and the instant FLIM hardware. Use the pop-up menus in the “I/O” tab to configure the input and output ports.

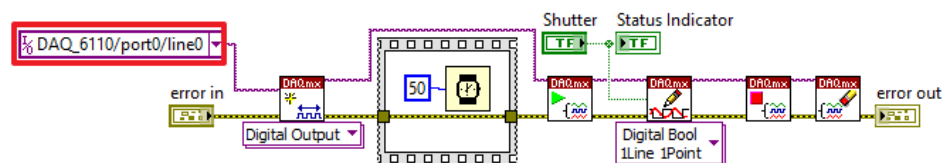


The following ports and channels should be configured before running the program:

- Mixer AI Channel(s)

- Configure 4 analog input (AI) channels of a DAQ card (e.g., National Instruments DAQ 6110) to read the IF voltages of the four mixers in instant FLIM
- DC AI Channel(s)
 - Configure 1 AI channel of a DAQ card (e.g., National Instruments DAQ 6323) to read the DC voltage from the bias tee (i.e., the intensity signal) in instant FLIM
- Bias AO Channel(s)
 - Configure 4 analog output (AO) channels of a DAQ card (e.g., National Instruments DAQ 6323) to generate the bias voltages for the four phase shifters in instant FLIM
- Scan AO Channel(s)
 - Configure 2 AO channels of a DAQ card (e.g., National Instruments DAQ 6110) to generate the controlling voltages for the galvo scanners (e.g., Thorlabs GVS002); AO1 and AO2 for fast and slow scanning axes, respectively
- Stage VISA COM
 - Configure the computer's COM port that connects to the motorized stage system (e.g., Prior OptiScan III)
- DM Resource Name (Optional)
 - Configure the USB resource name assigned to the deformable mirror (e.g., Thorlabs DMP40-P01) used in the optional adaptive optics system

In addition, a mechanical shutter (e.g., Thorlabs SHB1T) should be controlled by a digital output line of a DAQ card (e.g., National Instruments DAQ 6110). By default, the program uses port0:line0 of a DAQ 6110 card to control the shutter. The user can change the line that controls the shutter in the file “ShutterControl.vi”:



4. System Calibration

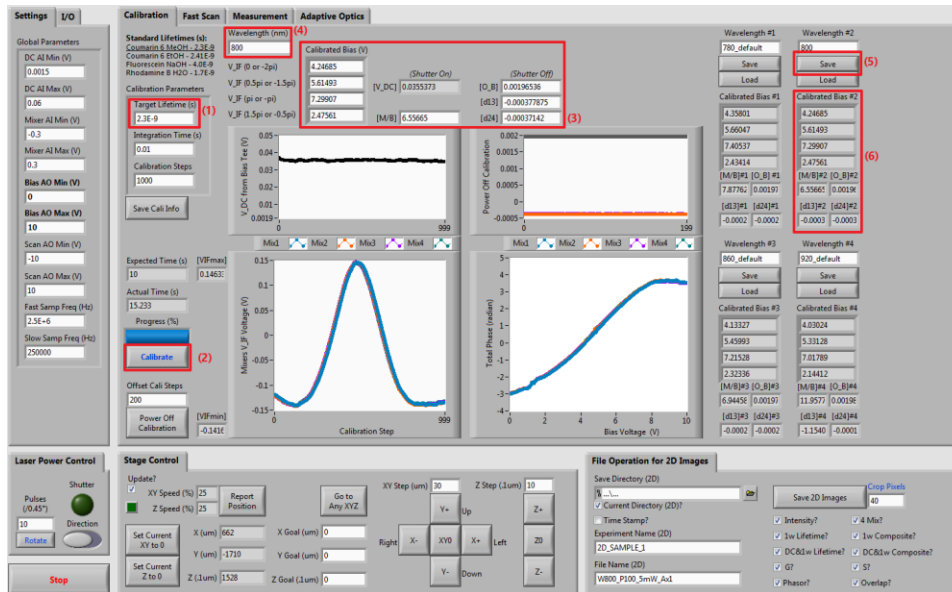
Prepare lifetime standards, i.e., fluorophore solutions with known fluorescence lifetimes^{1,2}. Here are a few examples of lifetime standards:

- 1 mM Coumarin 6 in Methanol: $\tau = 2.3$ ns
- 1 mM Coumarin 6 in Ethanol: $\tau = 2.4$ ns
- 1 mM Fluorescein in 0.1M NaOH (pH=13): $\tau = 4.0$ ns
- 1 mM Rhodamine B in water: $\tau = 1.7$ ns

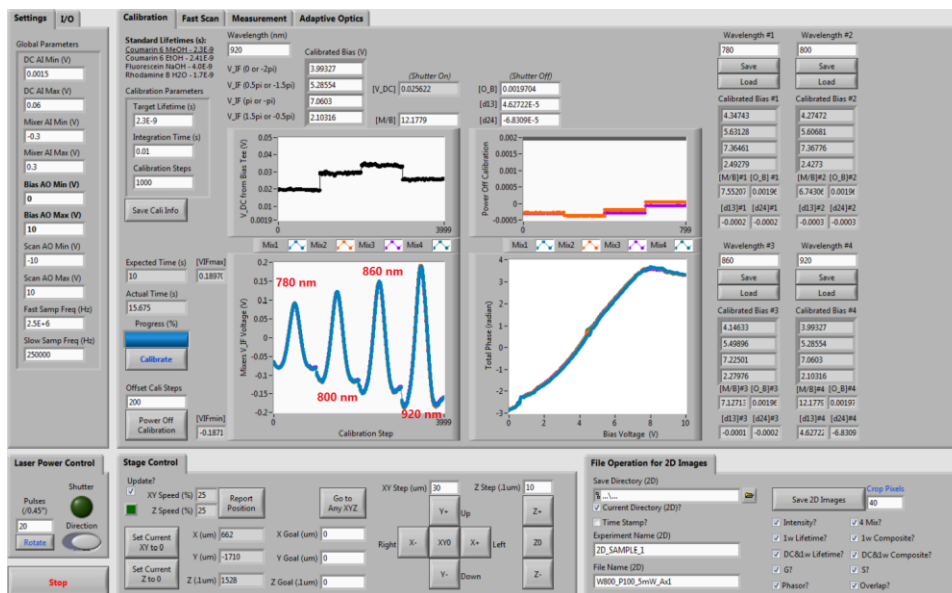
Once a lifetime standard is prepared (in a cuvette, petri dish, or glass slide with cavity), fill in “Target Lifetime (s)” (1) with the expected lifetime of the standard (e.g., 2.3E-9 for 1mM Coumarin 6 in Methanol), place the standard on the stage, open the laser shutter, focus the beam into the fluorophore solution, and click the button “Calibrate” (2) to start the necessary system calibration. The program automatically performs calibration using the lifetime standard. Once the calibration is complete, the coefficients (3) required for instant FLIM measurements are automatically calculated. These coefficients are:

- Calibrated Bias (V): Bias voltages that are needed for the four mixers to effectively induce phase shifts of 0, 0.5π , π , and 1.5π
- M/B : The ratio between the conversion losses of the mixer (RF to IF ports) and the bias tee (RF&DC to DC ports)
- O_B : The DC offset (invariant to PMT signal variations) on the bias tee’s DC port
- d_{13} : The difference between the DC offsets of the first and third mixers’ IF ports
- d_{24} : The difference between the DC offsets of the second and fourth mixers’ IF ports

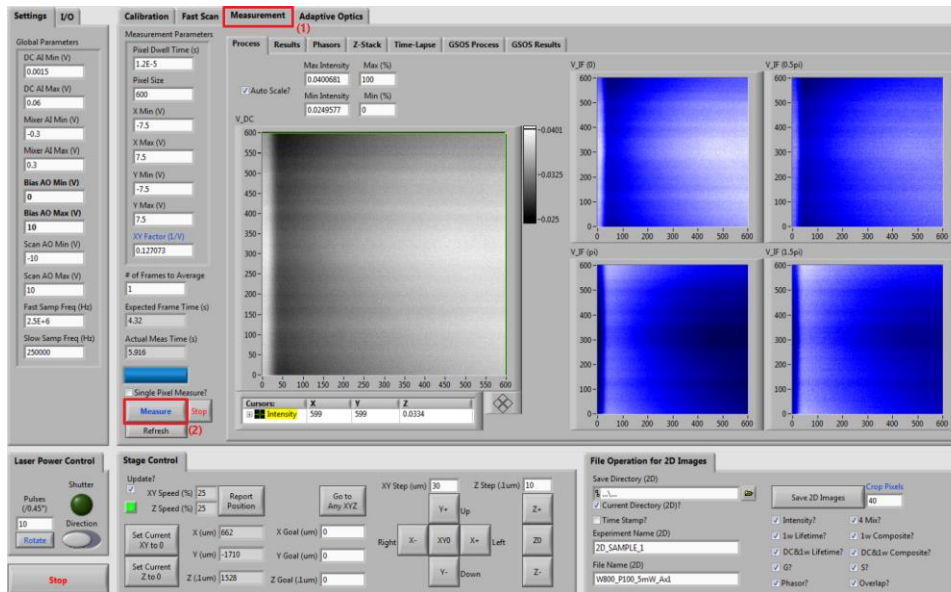
Because different excitation wavelengths result in different measurement coefficients, the calibration procedure should be performed for each excitation wavelength that will be used. The user can fill in the “Wavelength (nm)” box (4) to record the excitation wavelength currently being calibrated with and, after calibration, click the “Save” button (5) to save the calibrated coefficients to the program’s front panel (6).



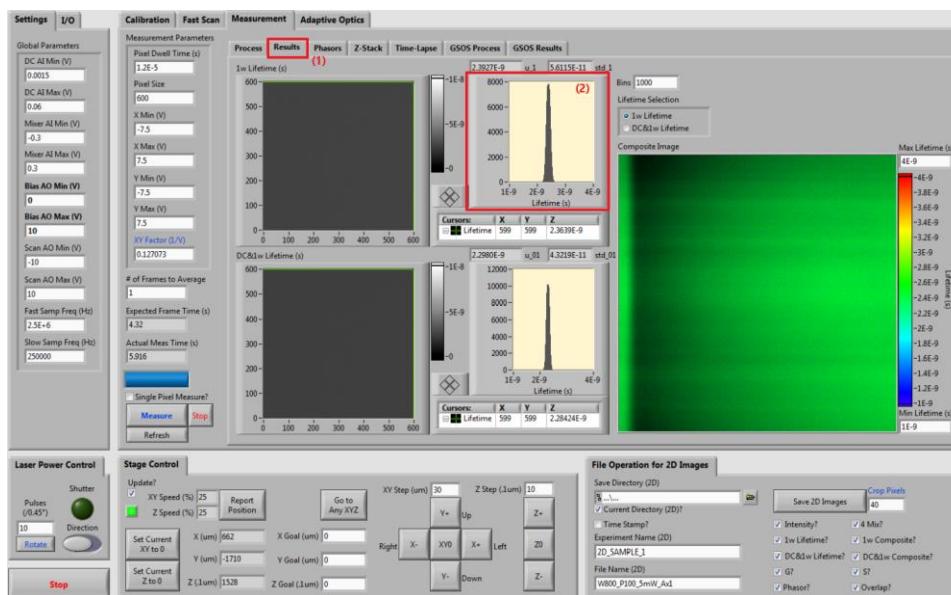
A total of four calibration results (four different excitation wavelengths) can be stored simultaneously. Before performing real measurements, the user should click the “Load” button to load the calibrated coefficients matching the experimental condition into the program.



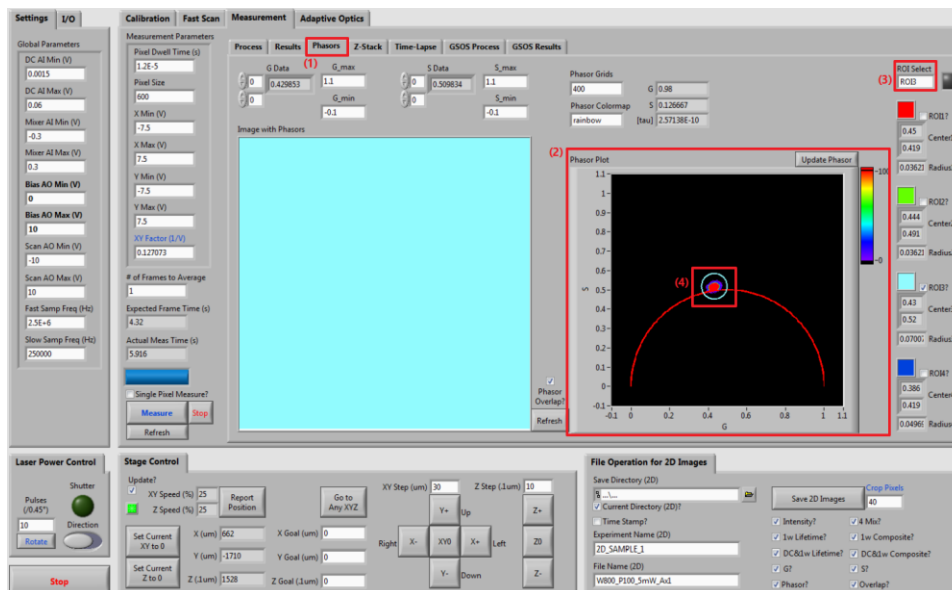
To evaluate if the calibration is successful, the user can perform a measurement while the lifetime standard is still under the microscope. Switch to the “Measurement” tab (1) and click the “Measurement” button (2):



Switch to the “Results” tab (1) to check the measurement results. If the calibration is correct, the values in the lifetime image and histogram (2) should match that of the lifetime standard used for calibration:



Meanwhile, on the “Phasors” tab (1), the phasors in the phasor plot (2) should be located at the semicircle. The user can label the pixels corresponding to the phasors by selecting a region of interest (ROI) (3) and then draw the ROI on the phasor plot (4). If the calibration is correct, all image pixels on the left should be labeled with the ROI’s color.

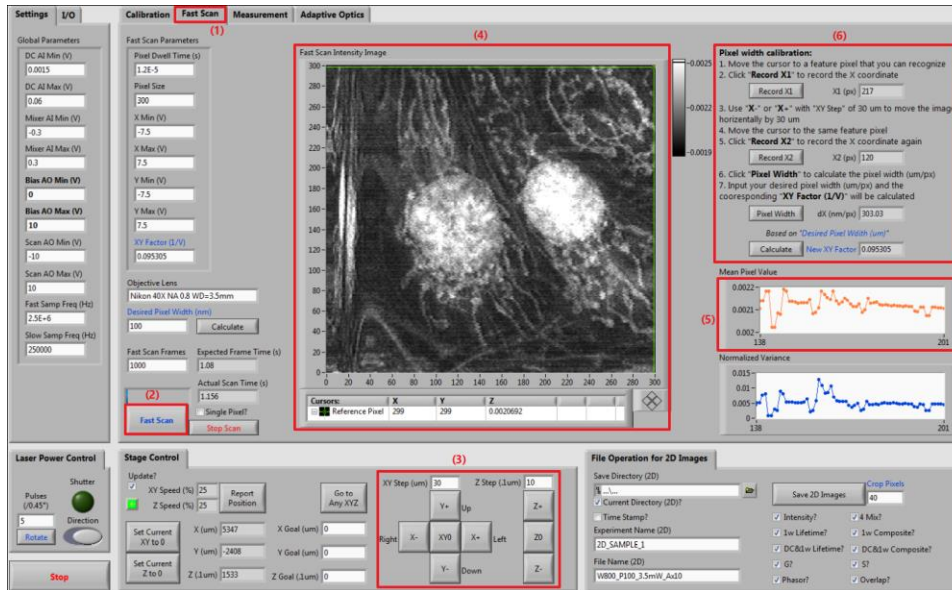


5. Find Focal Position

In this protocol, we will use a standard biological test slide (FluoCells prepared slide #1, F36924) to demonstrate how to perform an instant FLIM measurement.

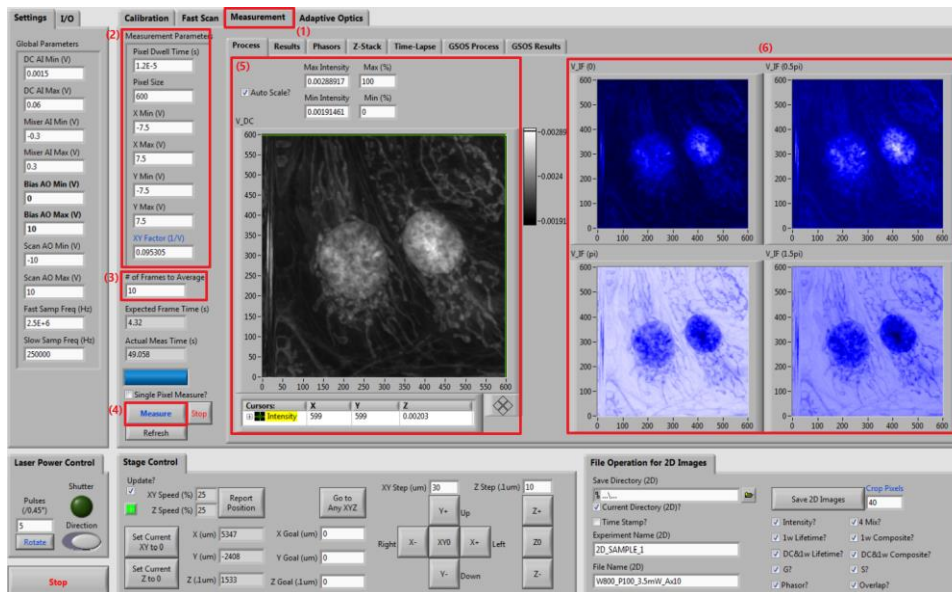
After placing the sample on the stage, switch to the “Fast Scan” tab (1) where the program uses crude but fast scans (faster than one frame per second) to help the user find the focal position. Click the “Fast Scan” button (2) to start scanning and change the stage positions (3) while the images are generated in real time. Change the XY and Z step sizes if needed. When a focal position is found, the user should expect not only a clear image (4) but also a high “Mean Pixel Value” of the image (5).

Once a clear image of the sample is obtained, the user can calibrate the pixel width according to the on-screen instructions (6). The pixel width is related to the objective lens used; therefore, the pixel width calibration should be performed each time a new objective lens is used.



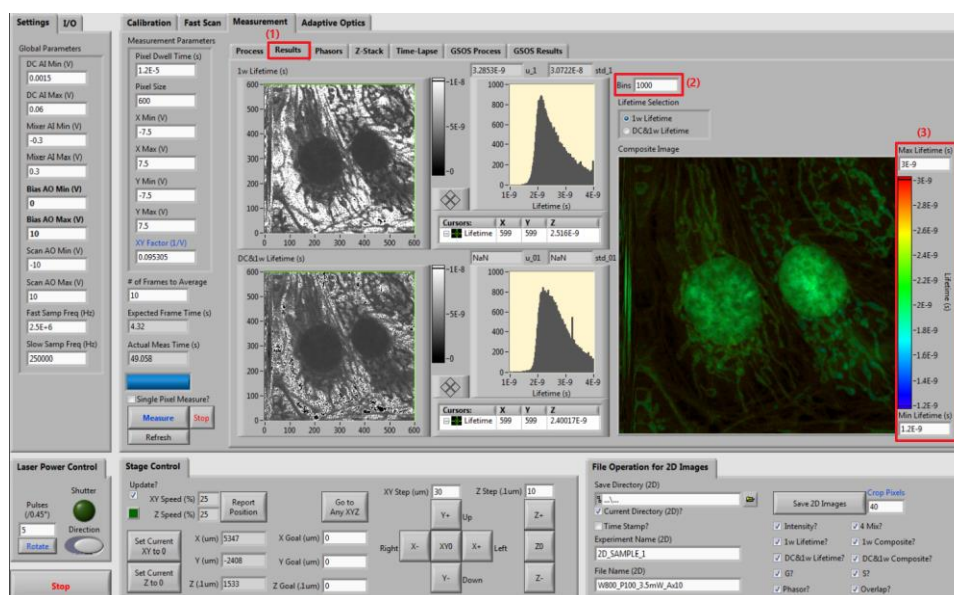
6. Intensity Imaging

Switch to the “Measurement” tab (1) for intensity imaging. Fill in the measurement parameters (2), including the pixel dwell time, pixel size, and XY Factor (obtained from pixel width calibration). Specify the “# of Frames to Average” (3) for each image; the more frames used for averaging, the higher signal-to-noise ratio the resulting image has. Click the “Measure” button to start measurement (4). When the measurement is complete, one can modify the brightness/contrast of the intensity image (5). The mixer images from the four mixers can also be seen (6).



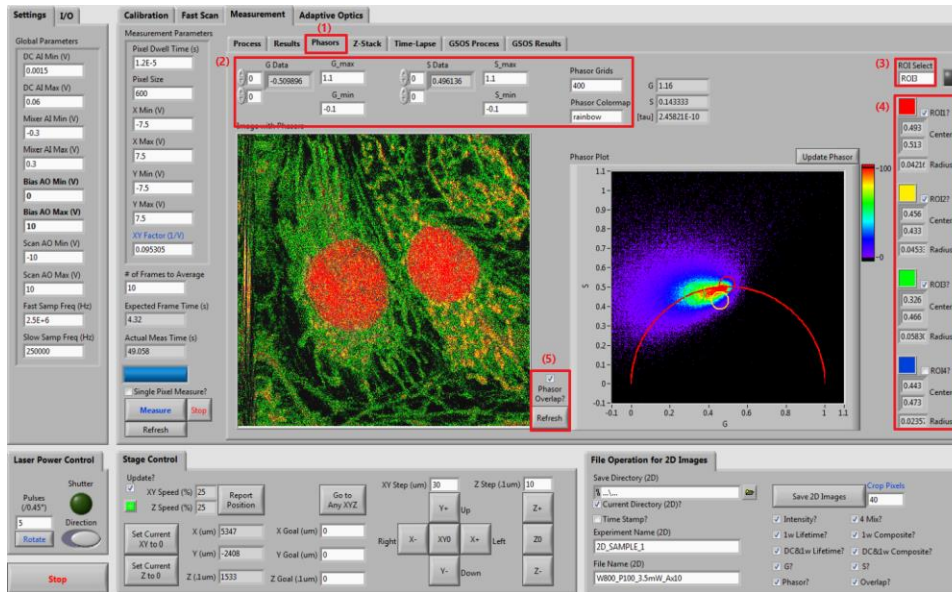
7. Fluorescence Lifetime Imaging

In instant FLIM, all FLIM data, including lifetime images, phasor plots, etc., are generated simultaneously with the intensity image; therefore, once the intensity imaging is complete, the lifetime images and phasor plots are also ready. Switch to the “Results” tab (1) to view the raw (gray scale) and composite (HSV mapping: lifetime to hue, intensity to value) lifetimes images. Both conventional (1ω) and super-sensitivity ($DC&1\omega$)³ lifetime images and histograms are generated. The bin of the histograms can be adjusted (2). In the composite lifetime image, the max and min of displayed lifetime values can be changed (3).



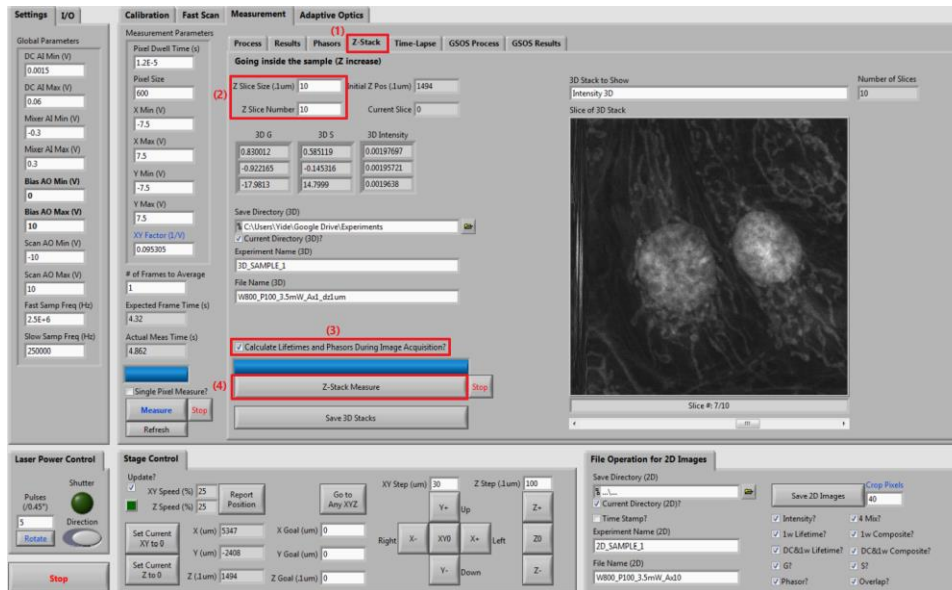
8. Phasor Plots

Phasor plots are also generated simultaneously with the intensity image. Switch to the “Phasors” tab (1) to view the phasor results. The parameters of the phasor plot, including the ranges of G and S, the number of bins (grids) of each direction of the 2D phasor histogram, and the colormap, can be modified (2). Up to four ROIs can be drawn on the phasor plot and label the corresponding pixels in the raw image. The user can draw ROIs by selecting a ROI (3) and then clicking and holding the mouse on the phasor plot. The drawn ROIs can be enabled or hidden by the check boxes (4). The pixels corresponding to the ROIs will be labeled/overlapped with the ROIs’ colors if the “Phasor Overlap?” box is checked (5).

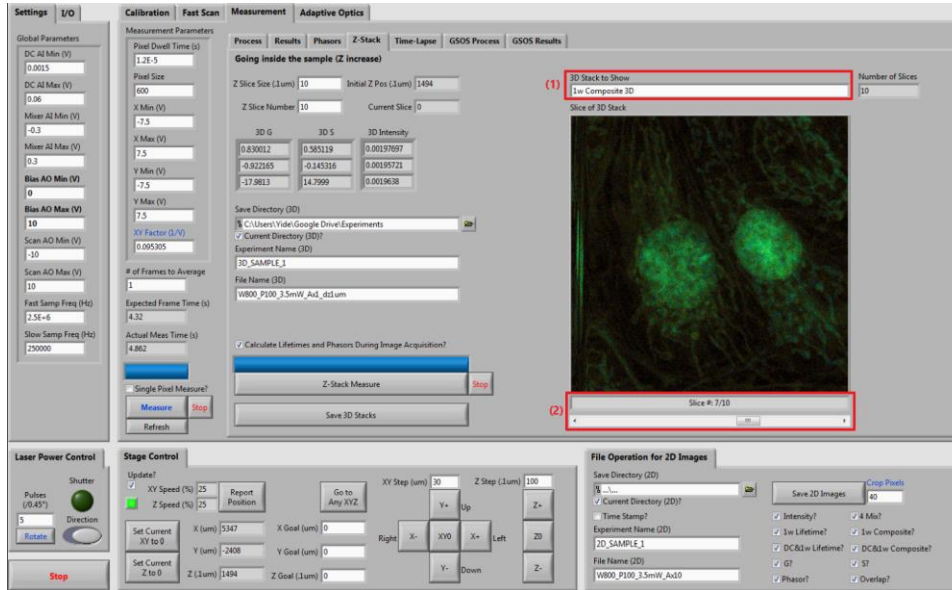


9. 3D Measurements

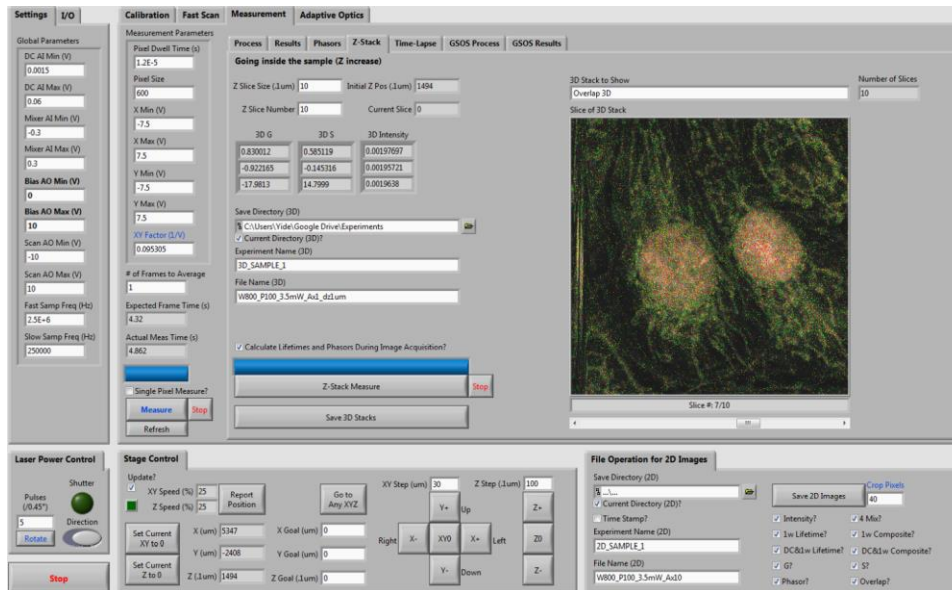
Switch to the “Z-Stack” tab (1) for 3D stack measurements. Specify the depth of each slice in the Z-stack (2). Check the “Calculate Lifetimes and Phasors During Image Acquisition?” box (3) if needed; disabling the box can speed up the 3D image acquisition. Start the 3D measurement by clicking the “Z-Stack Measure” button (4).



Once the 3D measurement is complete, the user can view different versions of 3D stack, such as intensity, lifetime, composite lifetime, and phasor plot (1). Adjust the slider (2) below the image to view different slices in the stack.

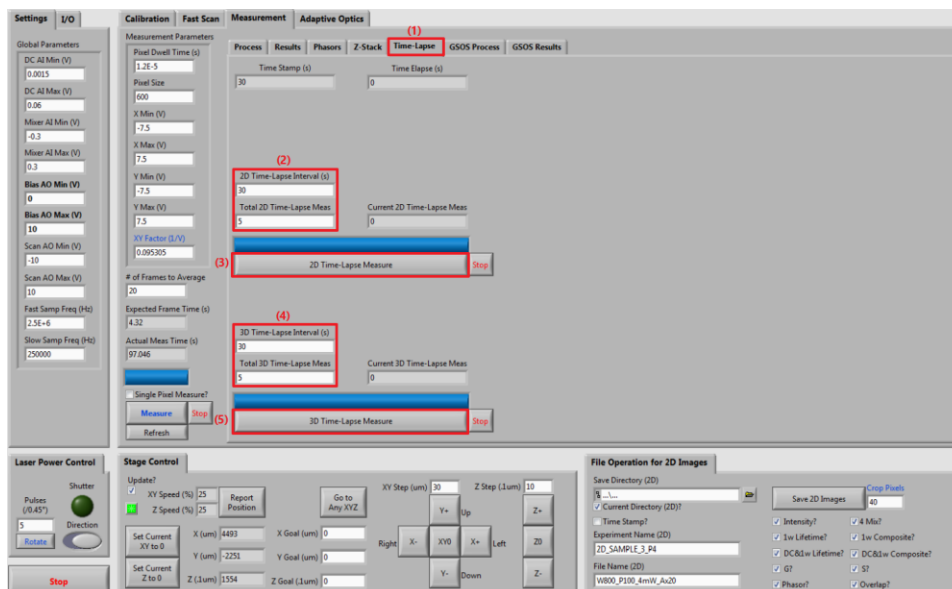


The displayed phasor overlap images are labeled according to the ROI configurations in the “Phasors” tab.



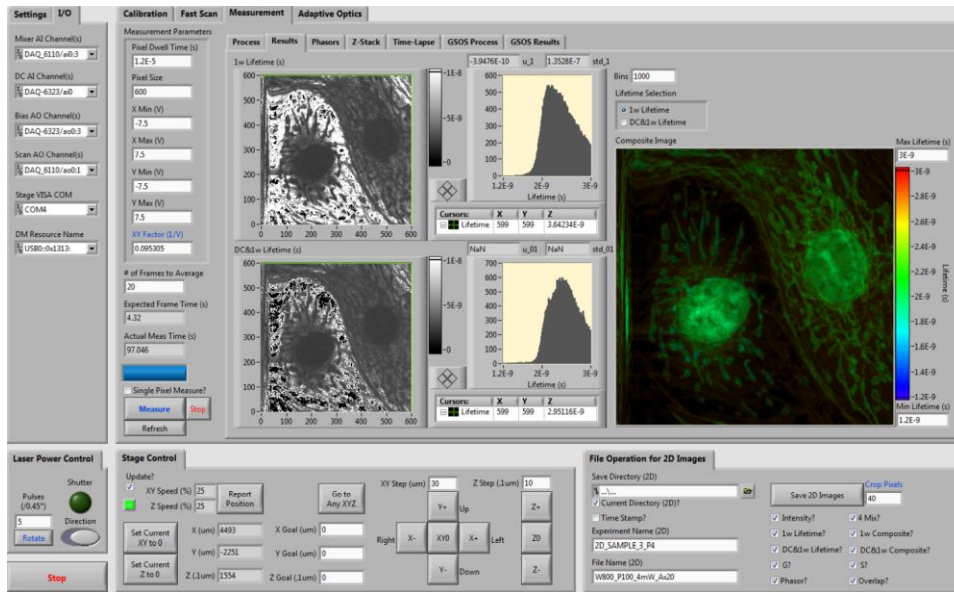
10. 4D Measurements

Switch to the “Time-Lapse” tab (1) to perform 2D time-lapse or 3D time-lapse (4D) measurements. For 2D time-lapse imaging, specify the time-lapse interval and the number of time points (2), and then start the measurement by clicking the “2D Time-Lapse Measure” button (3). For 3D time-lapse imaging, specify the interval and number of time points (4) and then start the measurement with the “3D Time-Lapse Measure” button (5). As the measurement goes, the imaging data are automatically saved as TIF files in your computer’s disk.

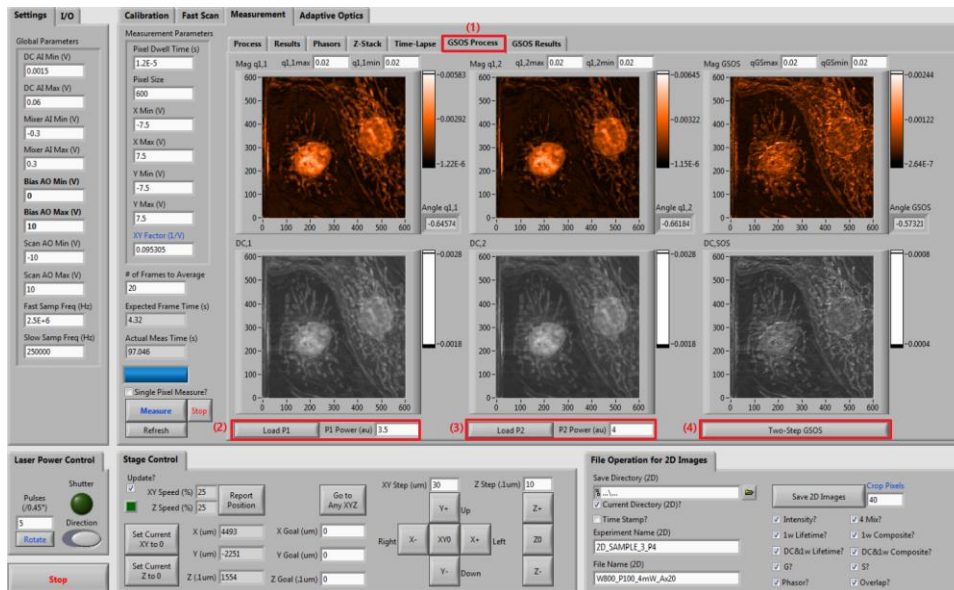


11. GSOS (Super-Resolution FLIM)

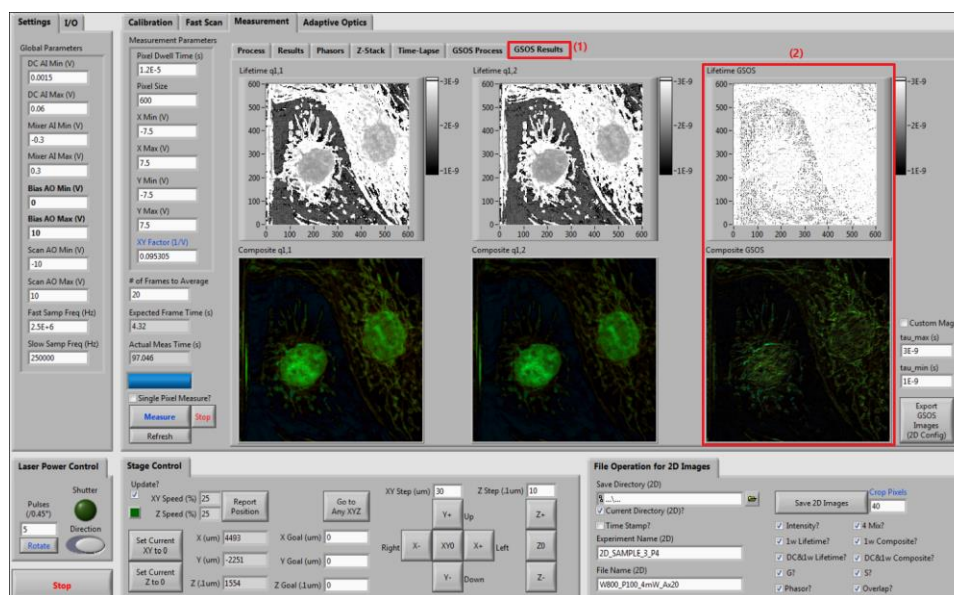
The instant FLIM system is compatible with GSOS, a super-resolution frequency-domain FLIM technique⁴. To perform GSOS microscopy, two instant FLIM imaging experiments with the same field of view on the same sample are needed. When performing the two experiments, the power of the excitation laser needs to be controlled and recorded (by a power meter) such that the power of the second experiment (P2) is slightly higher than that of the first one (P1). For example, we can set P1=3.5% and P2=4.0% for these two imaging experiments. First, set the power to P1 and perform the instant FLIM measurement as usual:



When the imaging at P1 is complete, switch to the “GSOS Process” tab (1) and click the “Load P1” button to load the instant FLIM data into the GSOS panel (2); the value of P1 should be filled in the “P1 Power (au)” box as the GSOS algorithm requires the values of P1 and P2. Then, change the laser power to P2 and perform another instant FLIM imaging experiment. When that is complete, switch back to the “GSOS Process” tab again, click the “Load P2” button to load the instant FLIM data for P2, and fill in the value of P2 (3). Finally, click the “Two-Step GSOS” button to start the GSOS processing (4), which can be executed instantly.



Switch to the “GSOS Results” tab (1) to view the results of the GSOS processing: the raw and composite lifetimes of the super-resolution FLIM image (2).



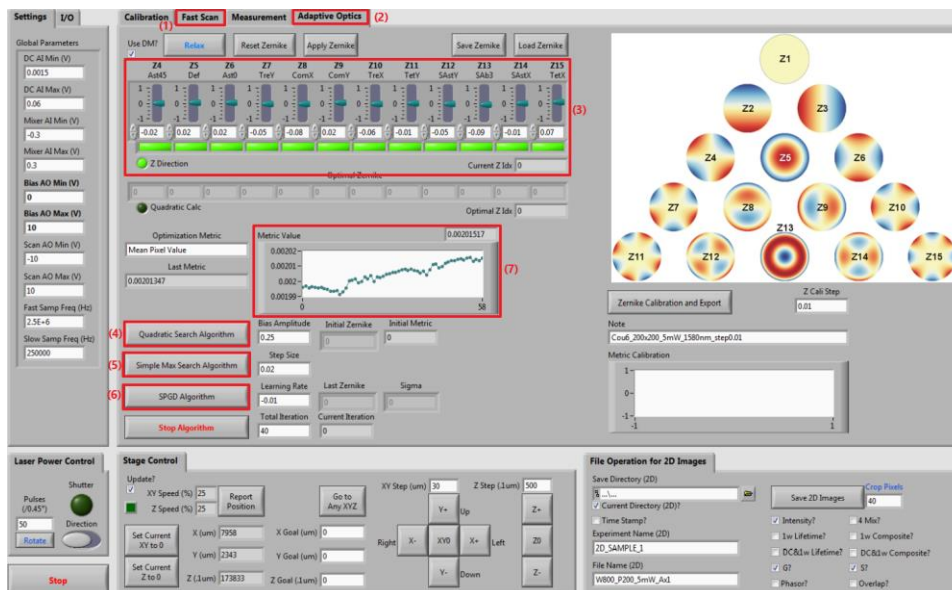
12. Adaptive Optics (Optional)

An adaptive optics (AO) setup consisting of a deformable mirror (Thorlabs DMP40-P01) can be used in instant FLIM to correct wavefront distortions and thus improve the imaging quality. Three adaptive optics optimization algorithms are included in this program to configure the wavefront correction elements:

- Simple Max Search Algorithm
 - This algorithm iterates through all possible Zernike coefficients, one by one, until a maximal metric is found
- Quadratic Search Algorithm⁵
 - This algorithm assumes that the optimization metric (e.g., the mean pixel value) is a quadratic function of the Zernike coefficients of the deformable mirror; the algorithm requires $2N + 1$ measurements to correct for N Zernike coefficients
- Stochastic Parallel Gradient Descent Algorithm^{6,7}
 - This algorithm stochastically variates the Zernike coefficients in parallel; every time the metric changes, the algorithm uses the gradient of the change to update the

coefficients until a maximal metric is obtained or the specified steps of iterations are reached

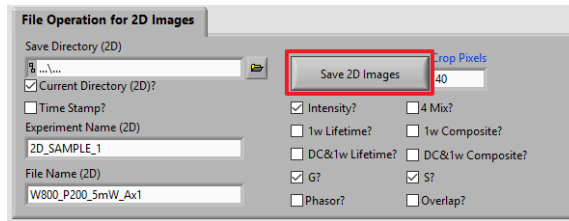
The AO optimization is based on the image metric obtained from the “Fast Scan” module (1). Switch to the “Adaptive Optics” tab (2) to perform AO related operations. The sliders (3) can directly control each one of the Zernike coefficients of the deformable mirror. The user may manually adjust these sliders, instead of using the optimization algorithms, to improve the imaging quality. The optimization algorithms mentioned above can be performed by clicking the “Quadratic Search Algorithm” (4), the “Simple Max Search Algorithm” (5), or the “SPGD Algorithm” (6) buttons. Regardless of the algorithm used, the metric (7) should increase as the optimization proceeds. The optimization is complete when the metric no longer increases.



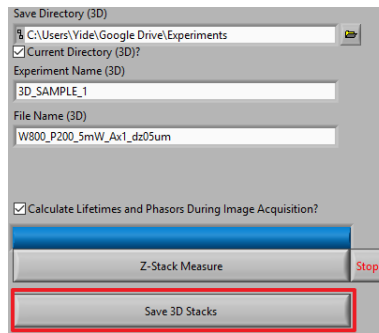
13. Data Export

All the data acquired or generated by the program can be exported.

The 2D images (intensity, mixer, raw/composite lifetime, phasor, overlap) can be exported using the “Save 2D Images” button in the “File Operation for 2D Images” tab. It is essential to save the “Intensity”, “G”, and “S” images because all other images (except for the mixer ones) can be recovered from these three images. In practice, we recommend the users to only save these three images to save the computer’s disk space.



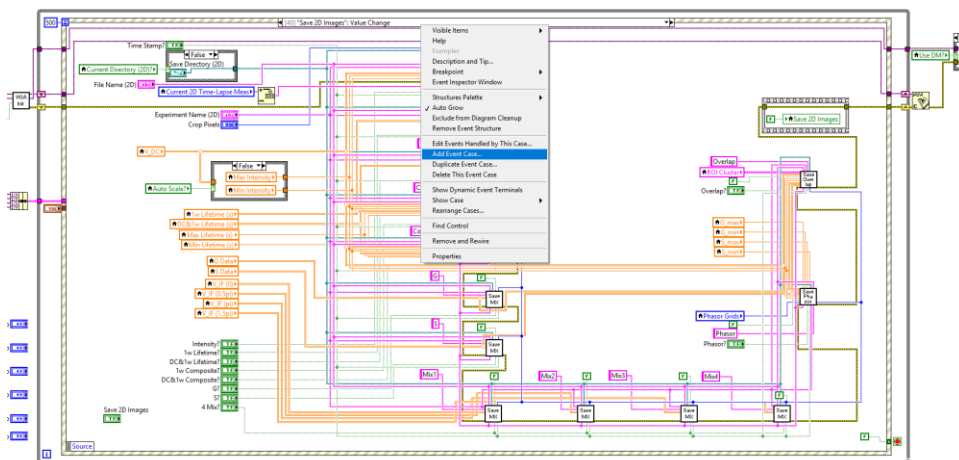
The 3D images can be exported using the “Save 3D Stacks” button in the “Z-Stack” tab. To save disk space, the program only saves the “Intensity”, “G”, and “S” stacks.



The time-lapse images are exported automatically according to the directory and file name defined in the “Z-Stack” tab.

14. Add New Functions

This program is fully open-source and highly modularized so users with LabView program skills can easily add new functions to the program. New functions can be added as new event cases so they will not interfere with existing functions:



References

1. Boens, N. *et al.* Fluorescence Lifetime Standards for Time and Frequency Domain Fluorescence Spectroscopy. *Anal. Chem.* **79**, 2137–2149 (2007).
2. Kristoffersen, A. S., Erga, S. R., Hamre, B. & Frette, Ø. Testing Fluorescence Lifetime Standards using Two-Photon Excitation and Time-Domain Instrumentation: Rhodamine B, Coumarin 6 and Lucifer Yellow. *J. Fluoresc.* **24**, 1015–1024 (2014).
3. Zhang, Y., Khan, A. A., Vigil, G. D. & Howard, S. S. Super-sensitivity multiphoton frequency-domain fluorescence lifetime imaging microscopy. *Opt. Express* **24**, 20862 (2016).
4. Zhang, Y., Benirschke, D., Abdalsalam, O. & Howard, S. S. Generalized stepwise optical saturation enables super-resolution fluorescence lifetime imaging microscopy. *Biomed. Opt. Express* **9**, 4077 (2018).
5. Debarre, D., Booth, M. J. & Wilson, T. Image based adaptive optics through optimisation of low spatial frequencies. *Opt. Express* **15**, 8176 (2007).
6. Vorontsov, M. A. & Sivokon, V. P. Stochastic parallel-gradient-descent technique for high-resolution wave-front phase-distortion correction. *J. Opt. Soc. Am. A* **15**, 2745 (1998).
7. Palczewska, G. *et al.* Noninvasive two-photon microscopy imaging of mouse retina and retinal pigment epithelium through the pupil of the eye. *Nat. Med.* **20**, 785–789 (2014).

Supplementary Protocol 2: Instant-FLIM-Analysis Matlab Program

1. Introduction

Instant-FLIM-Analysis is an open-source Matlab program with graphical user interfaces (GUIs) that allows users to analyze the imaging data acquired with an instant FLIM system. Specifically, only the “Intensity”, “G”, and “S” images from the instant FLIM experiments are required; all other FLIM data, such as fluorescence lifetime images, phasor plots, and image segments based on regions of interest (ROIs) or K-means clustering, can be generated by the program. The program is easy to use for its user-friendly GUIs. Meanwhile, as the program is fully open-source and highly modularized, users with Matlab programming expertise can easily modify the code to customize existing functions or to add new functions.

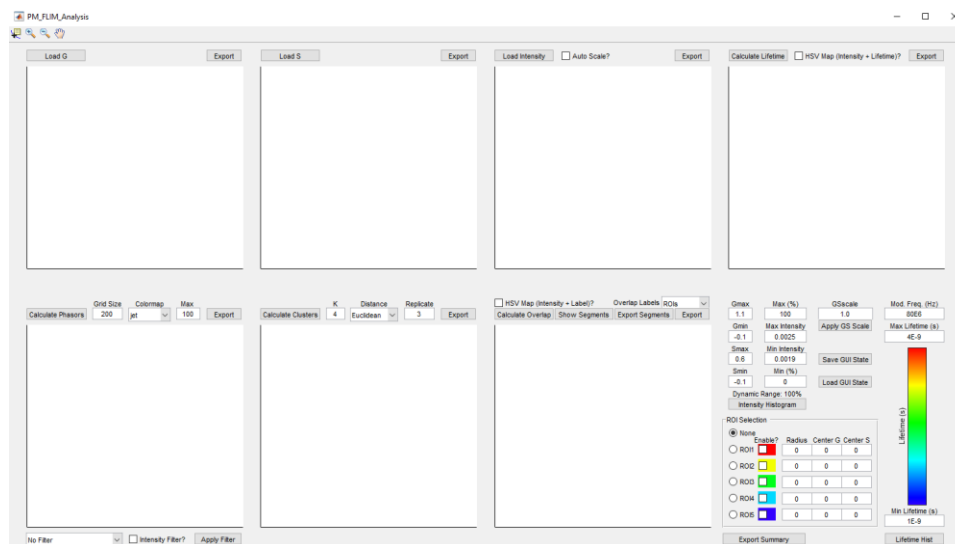
2. Installation

a. Option 1

- *This option requires a Matlab license*
- Install Matlab on your computer
- Download or clone (git clone) this GitHub repository:
<https://github.com/yzhang34/Instant-FLIM-Analysis.git>
- Open the file “Instant_FLIM_Analysis.m” in Matlab and RUN it

b. Option 2

- *This option does not require a Matlab license*
- Download or clone (git clone) this GitHub repository:
<https://github.com/yzhang34/Instant-FLIM-Analysis.git>
- Execute "MyAppInstaller_web.exe" in the "installer" directory
- Follow the instructions to install the program
- Matlab running environment will be automatically downloaded and installed
- Once the installation is complete, the program can be started with the icon on your Desktop



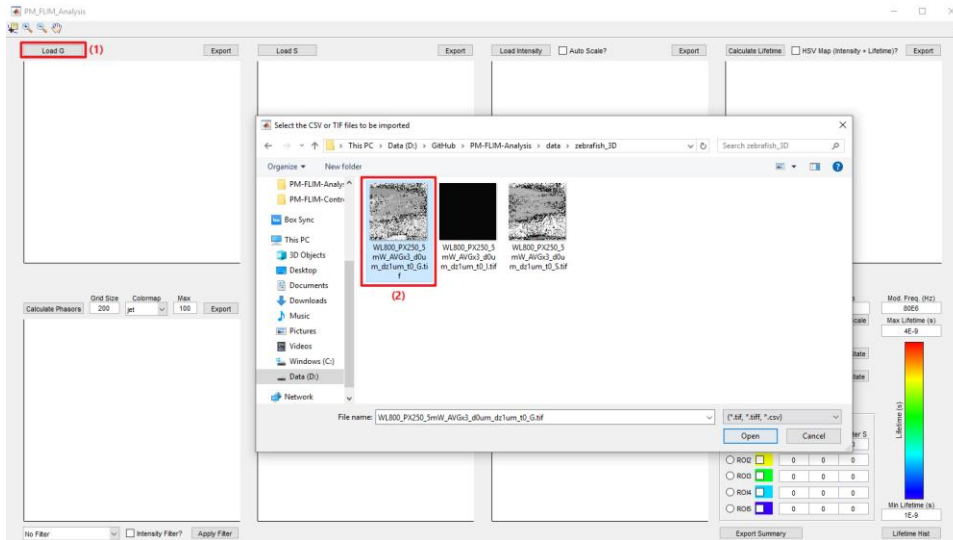
3. Data Import

The user only needs to acquire and store the “Intensity”, “G”, and “S” images from an instant FLIM imaging experiment, as other FLIM data can be generated from these three raw images in the Instant-FLIM-Analysis program.

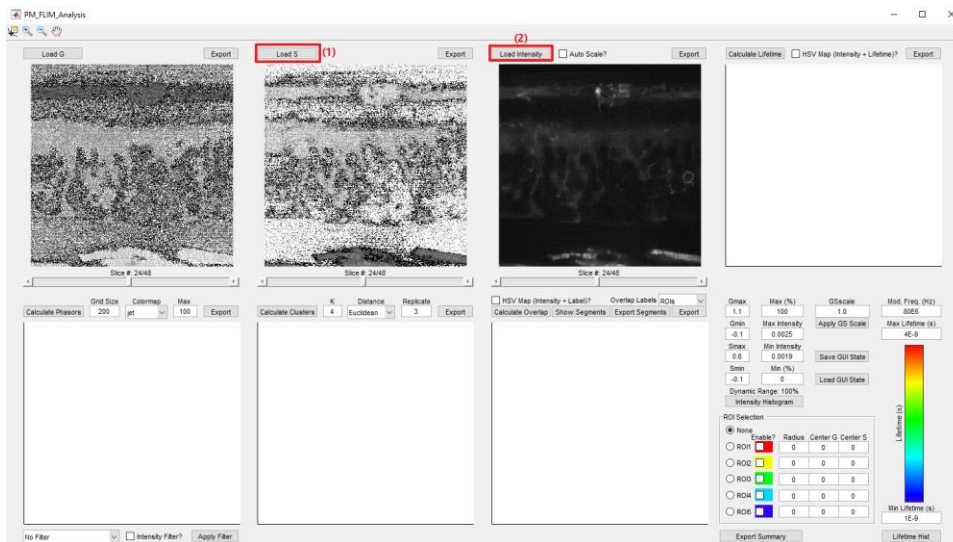
- In the “G” image, the value of each pixel is the x-coordinate (horizontal coordinate) of the phasor plot for that pixel. The G values should be between 0 to 1. Values outside of this range are caused by noise.
- In the “S” image, the value of each pixel is the y-coordinate (vertical coordinate) of the phasor plot for that pixel. The S values should be between 0 to 0.5. Values outside of this range are caused by noise.
- In the “Intensity” image, the value of each pixel is the two-photon fluorescence intensity reading, i.e., the voltage output of the detection PMT.

We have included two sets of instant FLIM data as examples in the GitHub repository. The 2D images in “/data/BPAE_cells_2D” were acquired from fixed bovine pulmonary artery endothelial (BPAE) cells (FluoCells prepared slide #1, F36924); the 3D image stacks in “/data/zebrafish_3D” were captured from a living EGFP-labeled *Tg(sox10:megfp)* zebrafish embryo at two days post fertilization. In this protocol, we will use the 3D zebrafish data to demonstrate the functions of the program.

Import the “G” image by clicking the “Load G” button (1) and selecting the related file (2). Here, we use the “WL800_PX250_5mW_AVGx3_d0um_dz1um_t0_G.tif” file in “/data/zebrafish_3D”.



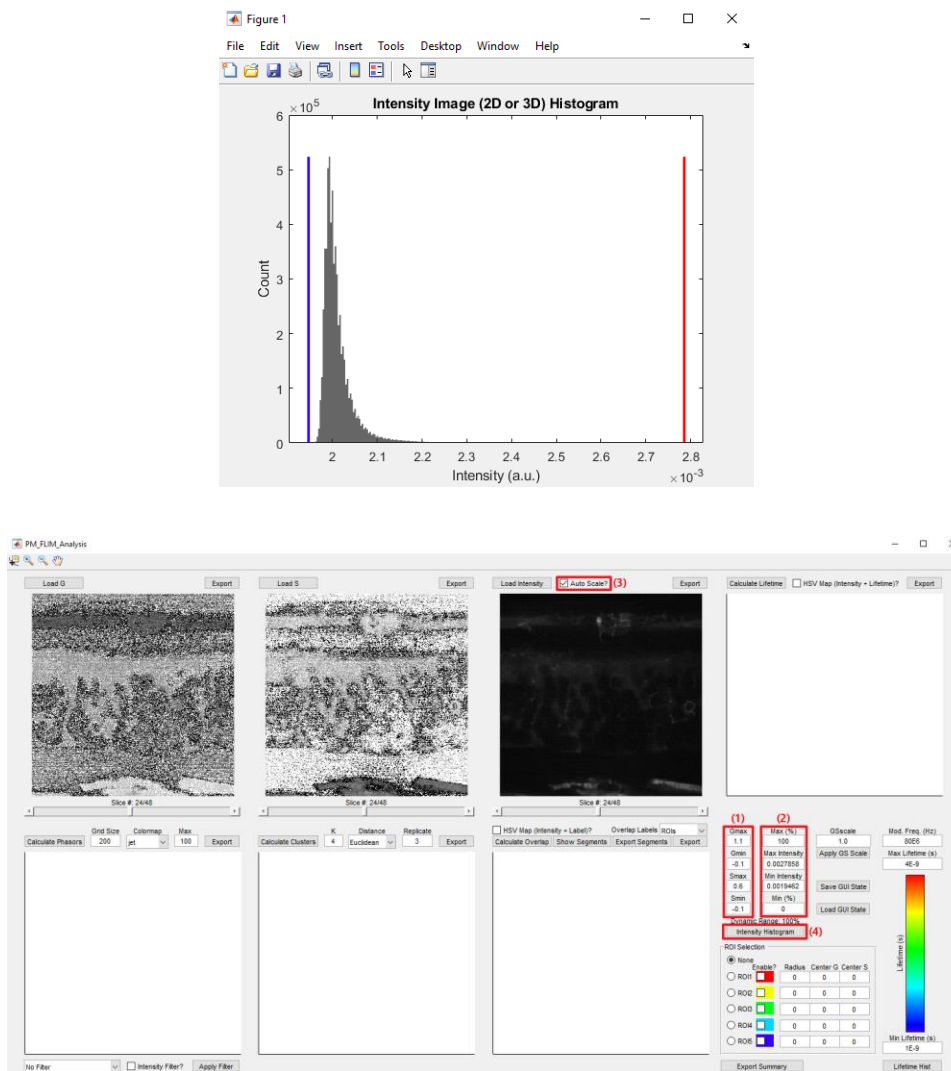
Similarly, import the “S” image, “WL800_PX250_5mW_AVGx3_d0um_dz1um_t0_S.tif”, and the “Intensity” one, “WL800_PX250_5mW_AVGx3_d0um_dz1um_t0_I.tif”, using the “Load S” (1) and “Load Intensity” (2) buttons, respectively.



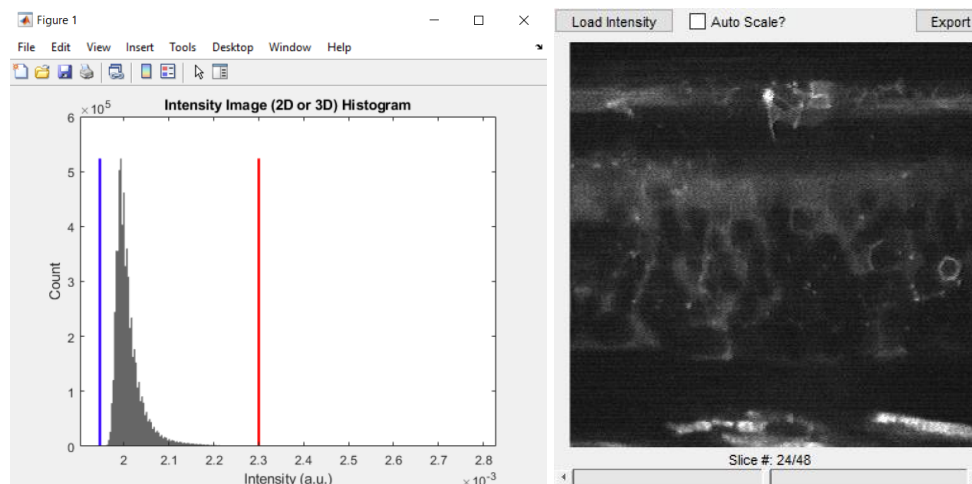
At this moment, all the raw instant FLIM data required by the program has been imported. The sliders below the images can be used to visualize different slices in the 3D stack.

4. Data Pre-Processing

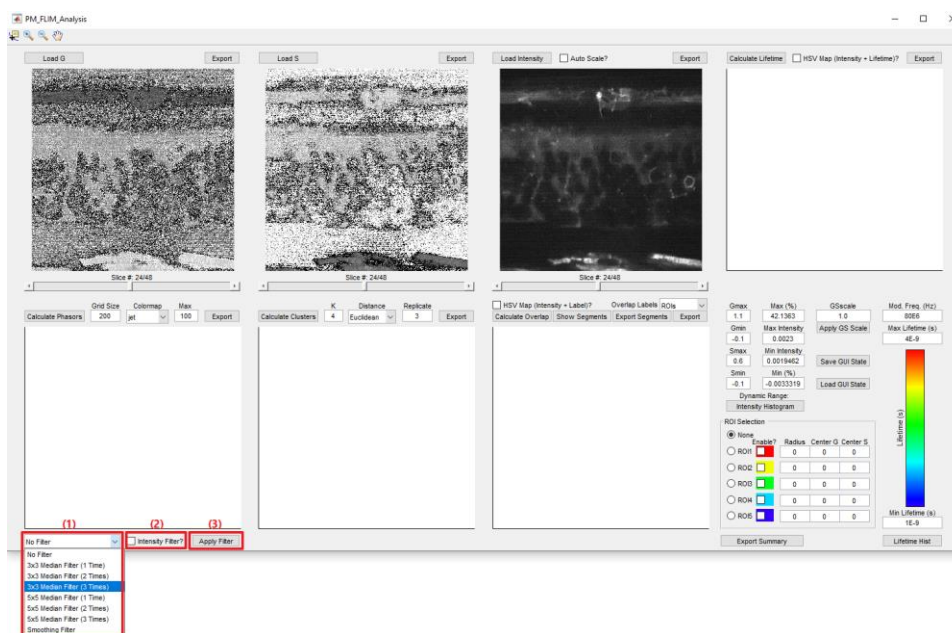
Some pre-processing steps are needed before analyzing the data. First, adjust the range of G and S by filling in the values of “Gmax”, “Gmin”, “Smax”, and “Smin” (1). The default values, “Gmax=1.1”, “Gmin=-0.1”, “Smax=0.6”, and “Smin=-0.1”, are recommended as pixels slightly perturbed by noise are included in the analysis. Next, adjust the Intensity range by either specifying the exact or percentage max and min intensity values (2) or enabling the “Auto Scale?” checkbox (3). The histogram of the intensity image can be viewed with the “Intensity Histogram” button (4), where the max and min intensities are marked with the red and blue lines, respectively:



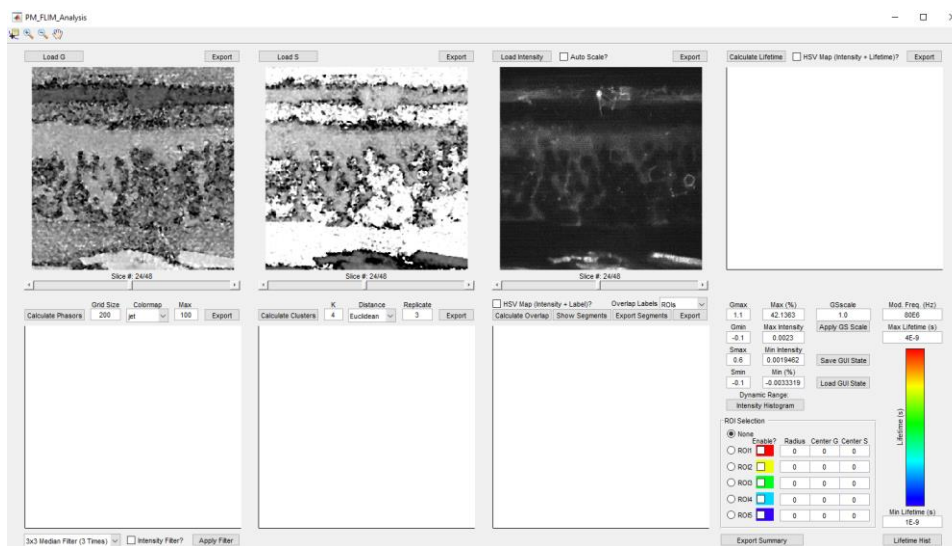
We recommend the user to adjust the max and min intensity values such that, by saturating a small percentage of pixels with high intensity, more details in the image can be visualized:



In addition, the signal-to-noise ratio (SNR) of the raw images, and consequently the SNR of generated images, can be improved by applying filters to the raw data. To do that, select a filter from the “No Filter” pop-up menu (1). If the “Intensity Filter?” checkbox (2) is enabled, the filter is also applied to the Intensity image; otherwise, only the phasor images (G and S) are filtered. Click the “Apply Filter” button (3) to perform the filtering operation. We recommend using the “3x3 Median Filter (3 Times)” or other median filters, as median filtering does not decrease the image resolution¹. The filtering operation could take some time depending on the size of the raw data. A progress window showing the filtering progress will appear during the operation.

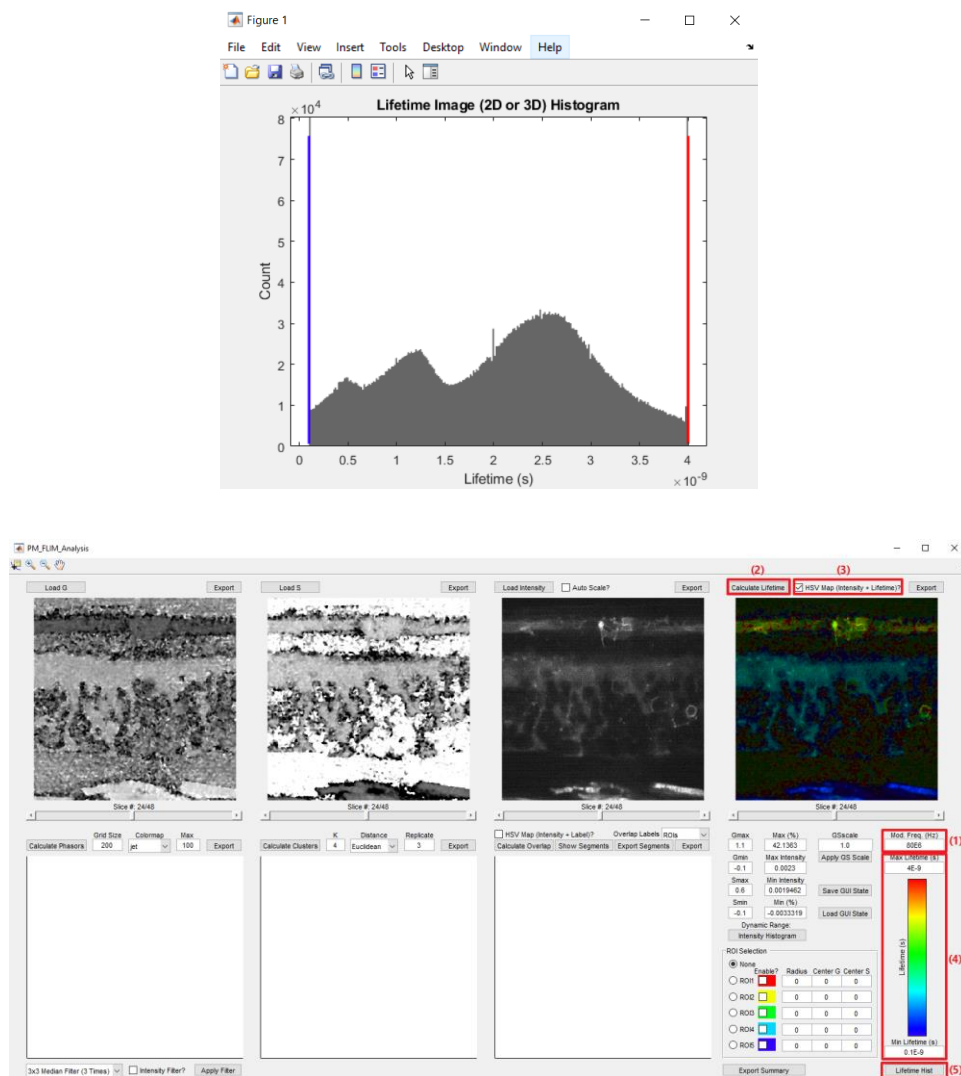


After filtering, the raw images look less noisy than before:



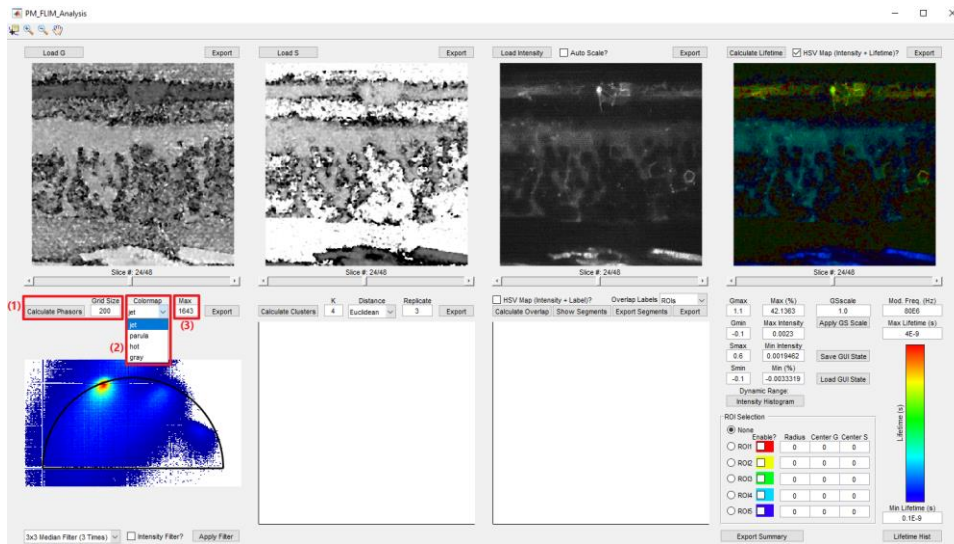
5. Fluorescence Lifetime Images

Fill in the “Mod. Freq. (Hz)” box (1) with the modulation frequency of the excitation laser during the instant FLIM image acquisition. We use a mode-locked Ti:sapphire laser (Spectra Physics Mai Tai BB, 710-990 nm, 100 fs, 80 MHz) in our instant FLIM system, so we write “80E6” in this box. Click the “Calculate Lifetime” button (2) to calculate fluorescence lifetimes. Note that there are two approaches to calculate fluorescence lifetimes in frequency-domain FLIM: phase-derived or modulation-derived approaches². In this work, we only consider phase-derived lifetimes for its simpler mathematical form compared to modulation-derived ones. The “HSV Map (Intensity + Lifetime)?” button (3) determines whether the lifetime image is displayed in raw or composite mode: if it is disabled, the raw lifetime image is shown in gray scale; if it is enabled, a composite lifetime image, where the image’s intensity and lifetime values are mapped to the pixels’ brightness and hue, respectively, is displayed. The range of displayed lifetime values can be adjusted with the “Max Lifetime (s)” and “Min Lifetime (s)” boxes (4). The histogram of the lifetime image can be viewed with the “Lifetime Hist” button (5), where the max and min lifetimes are marked with the red and blue lines, respectively:

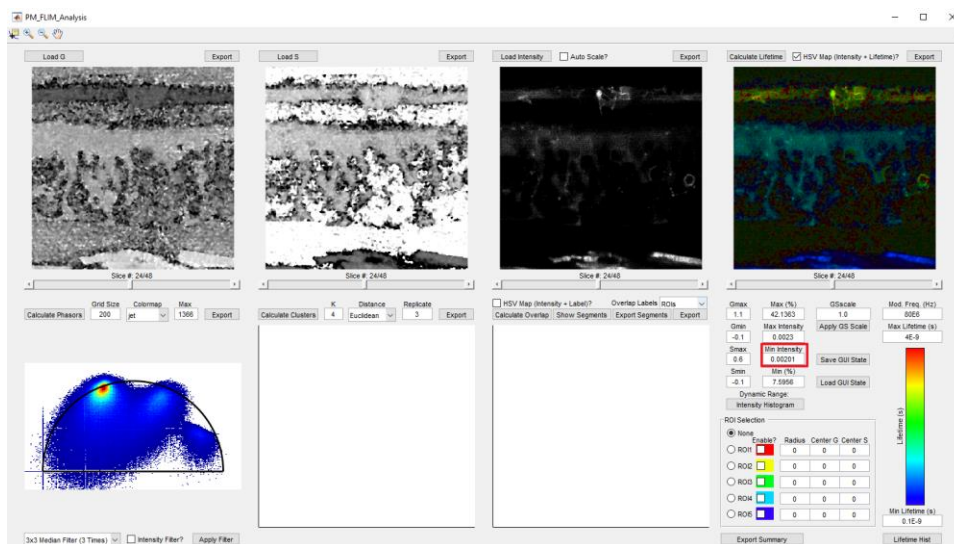


6. Phasor Plots

Phasor plots are 2D histograms of the pixels' G and S values. To generate phasor plots, specify the number of bins, or grids, in the "Grid Size" box and then click the "Calculate Phasors" button (1). A window will pop up showing the calculation progress. Once the phasor plot is generated, the user can change its colormap in the "Colormap" pop-up menu (2). The max displayed value of the 2D histogram, which is generated automatically, can also be changed in the "Max" box (3).



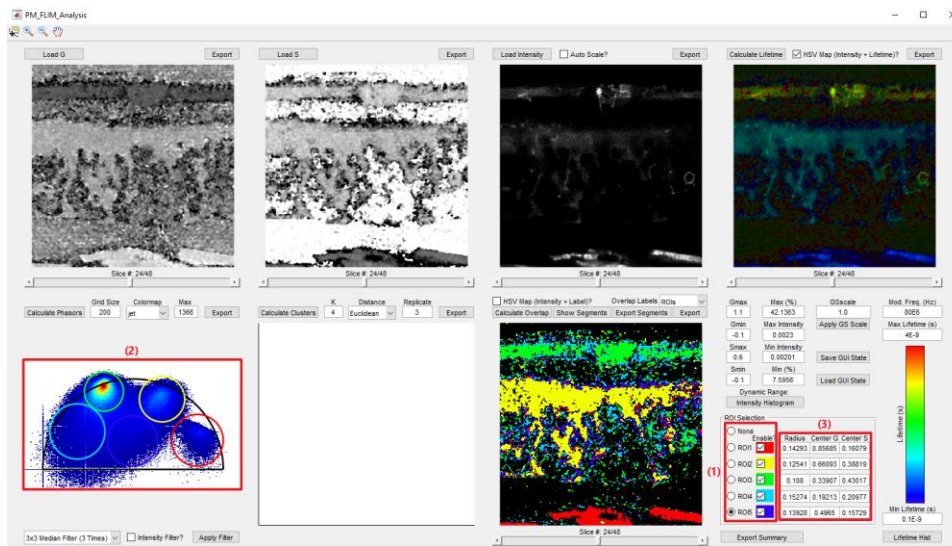
Because most of the pixels in the raw data are background noise, it is not uncommon to see these noise phasors locating outside of the semicircle. This issue can be addressed by increasing the value in the “Min Intensity” box to prevent the background noise pixels (intensity lower than the “Min Intensity” value) from being considered in calculating phasors:



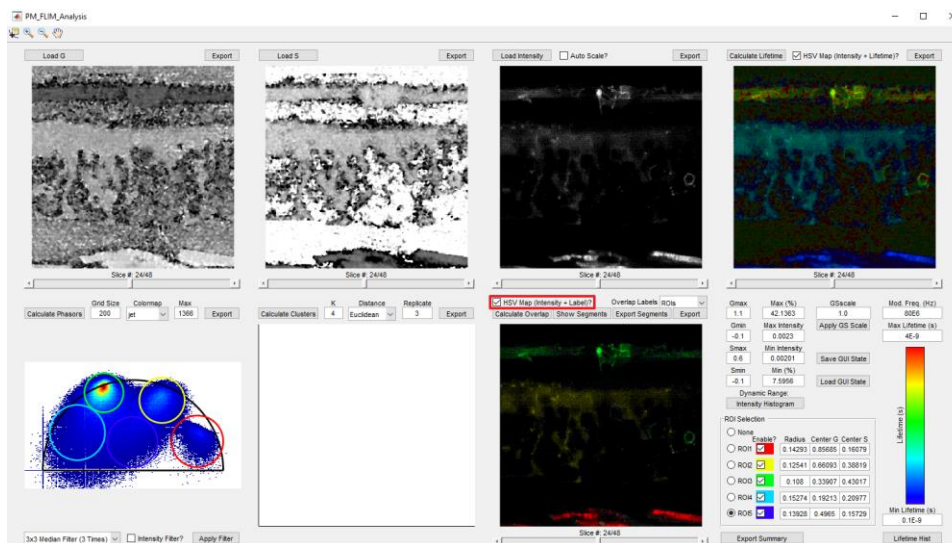
7. ROI Labeling of Phasors

The Instant-FLIM-Analysis program allows the user to draw ROIs on the phasor plot such that the pixels corresponding to the phasors located inside the ROIs can be identified and labeled with the ROIs’ colors. By properly drawing the ROIs and labeling the pixels, the user can effectively segment the raw images based on different FLIM signatures of the image structures. Before

drawing ROIs, make the ROI selection with the radio buttons (1). Draw the ROI on the phasor plot (2) by clicking, holding, moving, and releasing your mouse. The corresponding pixels in the raw image will be labeled to the ROI's color whenever the ROI is drawn or updated. Up to five ROIs can be drawn simultaneously. Once drawn, the ROIs and the labeled pixels can be enabled or disabled using the “Enable?” checkboxes (1). The ROIs' radii and center G and S coordinates are shown in the “Radius”, “Center G”, and “Center S” boxes (3) when they are drawn. The user can manually modify these values to change the sizes and locations of the corresponding ROIs.

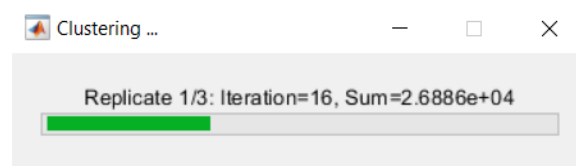


Like the composite lifetime image, the user can enable the “HSV Map (Intensity + Label)?” checkbox to map the intensity and labeled colors to the pixels' brightness and hue, respectively:

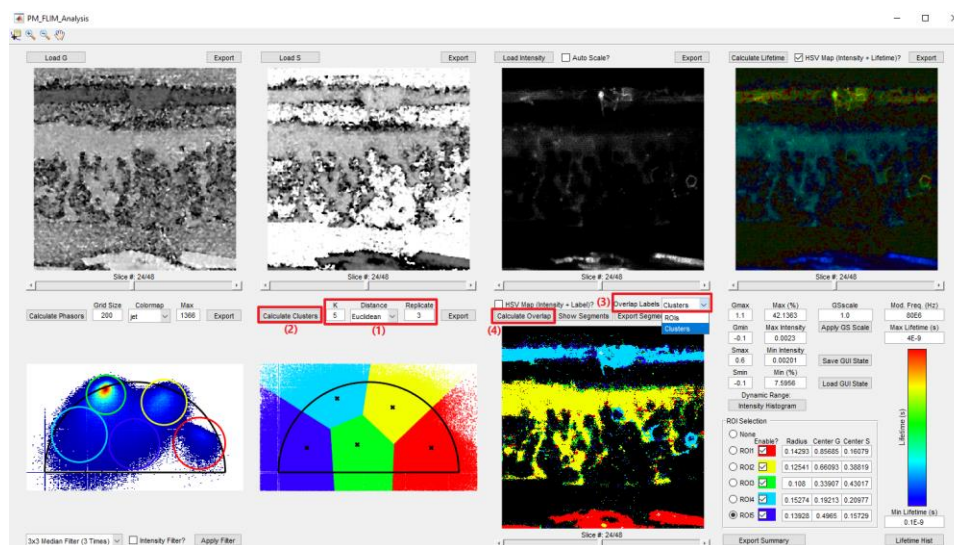


8. K-Means Clustering of Phasors

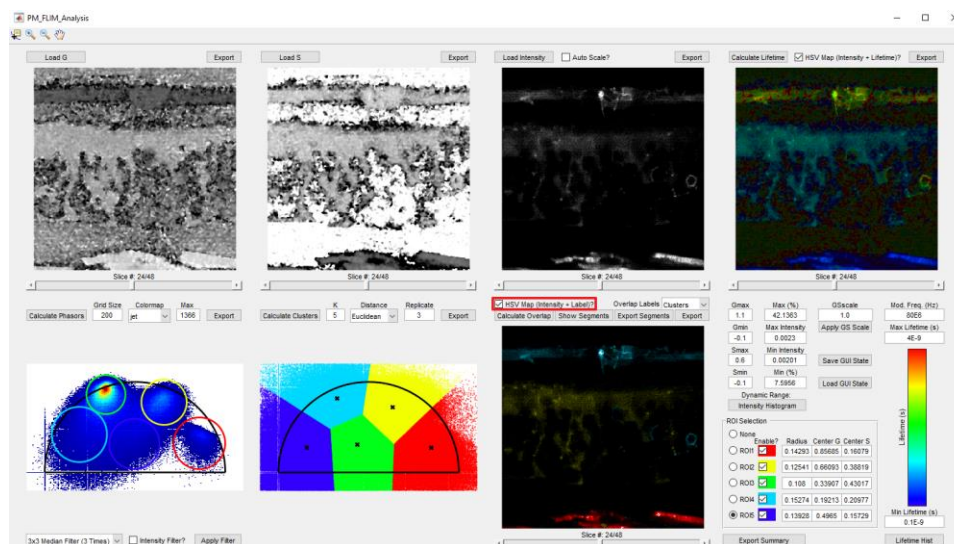
The Instant-FLIM-Analysis program includes an unsupervised machine learning feature, i.e., K-means clustering^{3,4}, which can be used to automate the manual ROI-based phasor labeling approach above in an unbiased way. Before performing K-means, specify the number of clusters (K), the distance metric (squared Euclidean, L1, or cosine), and the number of times to replicate the procedure (1). Start the procedure by clicking the “Calculate Clusters” button (2). The K-means clustering algorithm can be time-consuming for large images (3D or 4D). A window will pop-up showing the progress of the operation:



When the K-means clustering is complete, switch the “Overlap Labels” pop-up menu (3) to “Clusters”, and click the “Calculate Overlap” button (4). In the overlap image below, the pixels corresponding to different clusters will be labeled with the clusters’ colors.

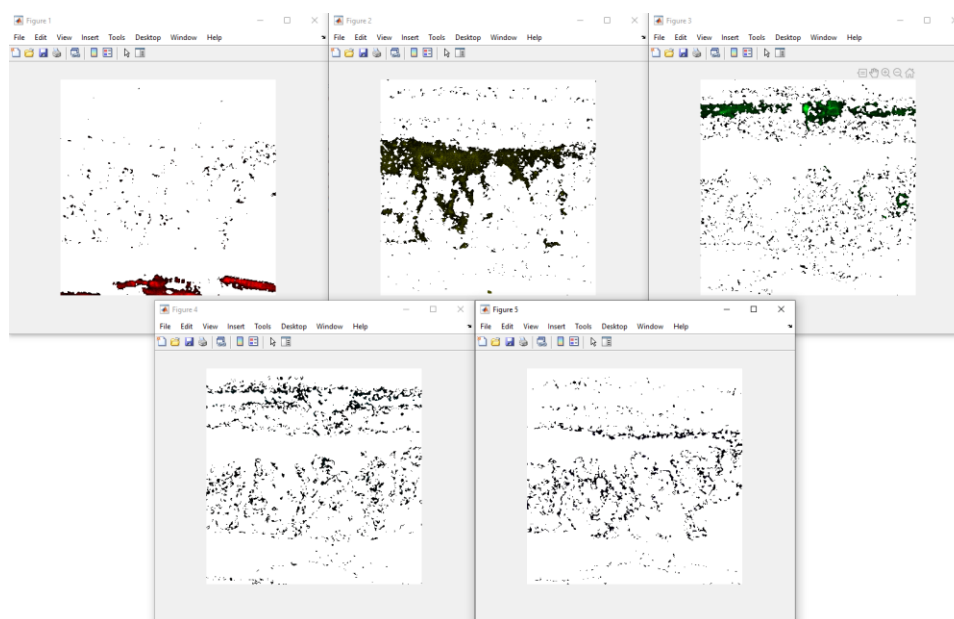


Likewise, the user can enable the “HSV Map (Intensity + Label)?” checkbox to map the intensity and cluster colors to the pixels’ brightness and hue, respectively:

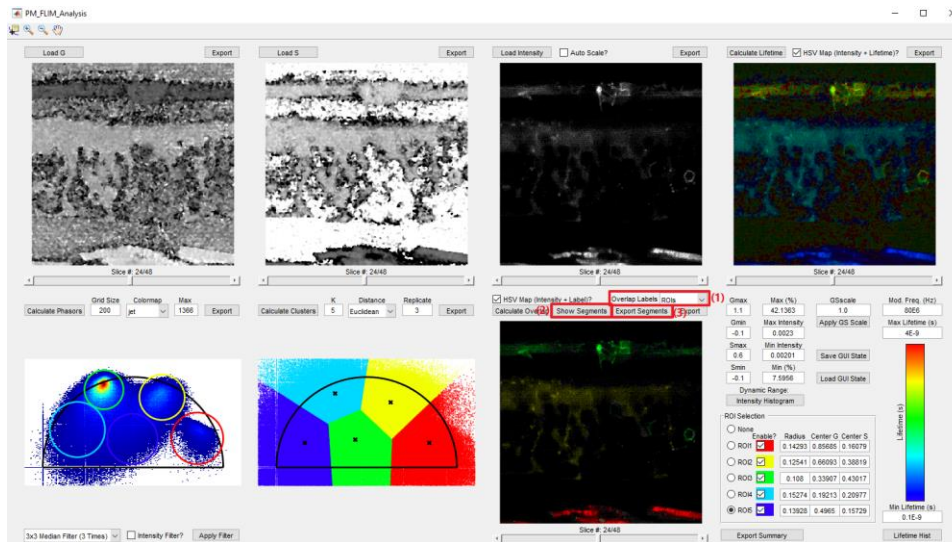
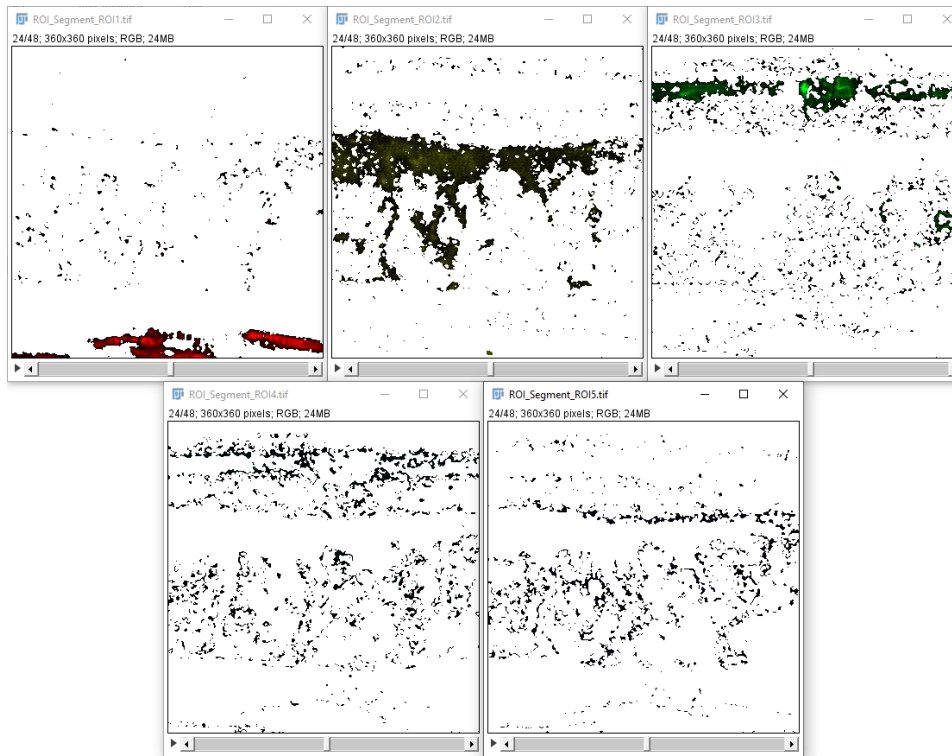


9. Image Segmentation

Both the ROI labeling and K-means clustering operations can be used to segment the images. For the ROI labeling and K-means clustering results, the pixels corresponding to each ROI and each cluster are grouped into a single segment, respectively. Before performing image segmentation, select whether the ROIs or clusters results are used in the “Overlap Labels” pop-up menu (1). The “Show Segments” button (2) can be used to display the segmented images as separate figures. Note that only a single frame of the stack (3D or 4D) can be displayed in this way:

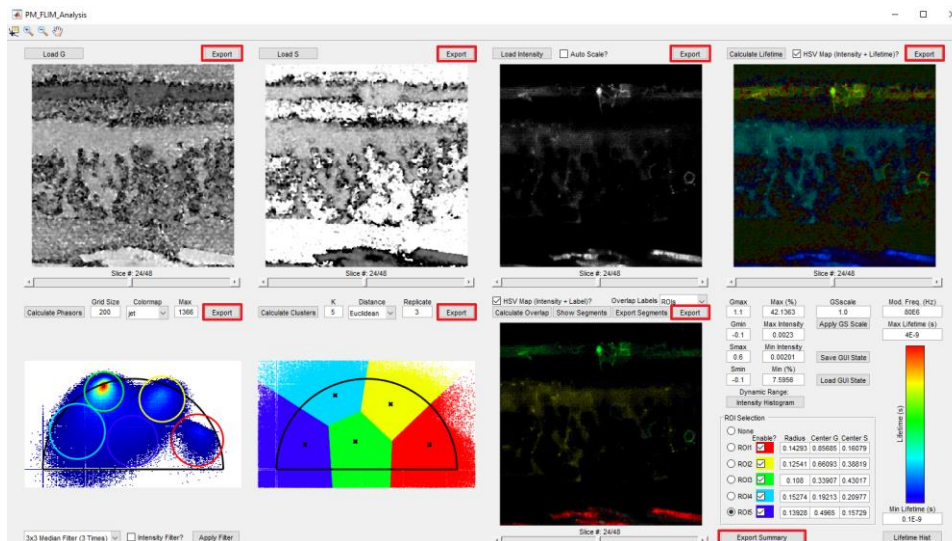


The “Export Segments” button (3) can be used to export the segments into separate TIF images. In this way, the exported segmented images have the same size as the raw image (3D or 4D).

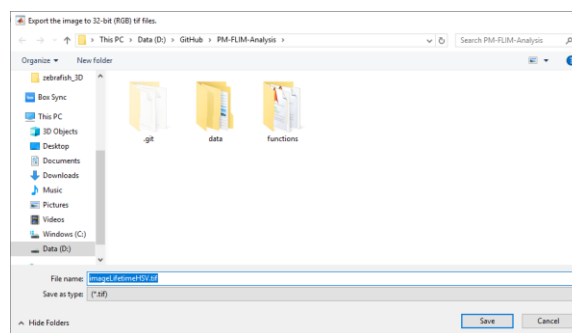


10. Data Export

All images and plots that can be seen in the Instant-FLIM-Analysis program can be exported into TIF files by using the “Export” buttons next to the images/plots. In addition, the screenshot of the program’s whole GUI can be exported using the “Export Summary” button.



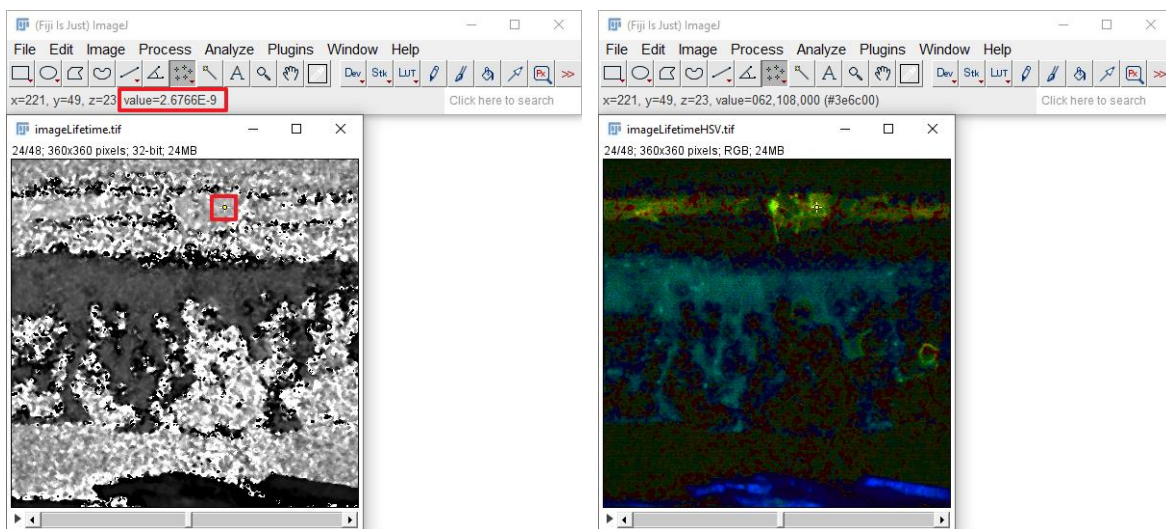
The user needs to specify the file names in order to export the images. All files should be saved to the default directory, where the program itself locates.



All exported TIF images are 32-bit. If the images are gray scale, the value of each pixel is a single-precision (32-bit) real number; if the images or plots have colors, the exported files are RGB format where each channel is 8-bit.

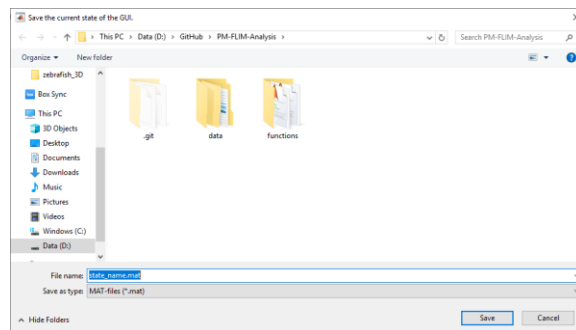
We recommend the user to view the 32-bit TIF images in ImageJ (<https://fiji.sc/>). For the single-precision images, such as the gray scale lifetime image, the lifetime value of each pixel can be

directly viewed. For the images with colors, the information of the exact lifetime values is lost; one can refer to the lifetime colormap in the program to get this information. Also, the Instant-FLIM-Analysis program will only export images to 3D stacks, even if the raw data are 4D; therefore, the user needs to manually change the exported 3D stacks to 4D by using the “Stack to Hyperstack” function in ImageJ.

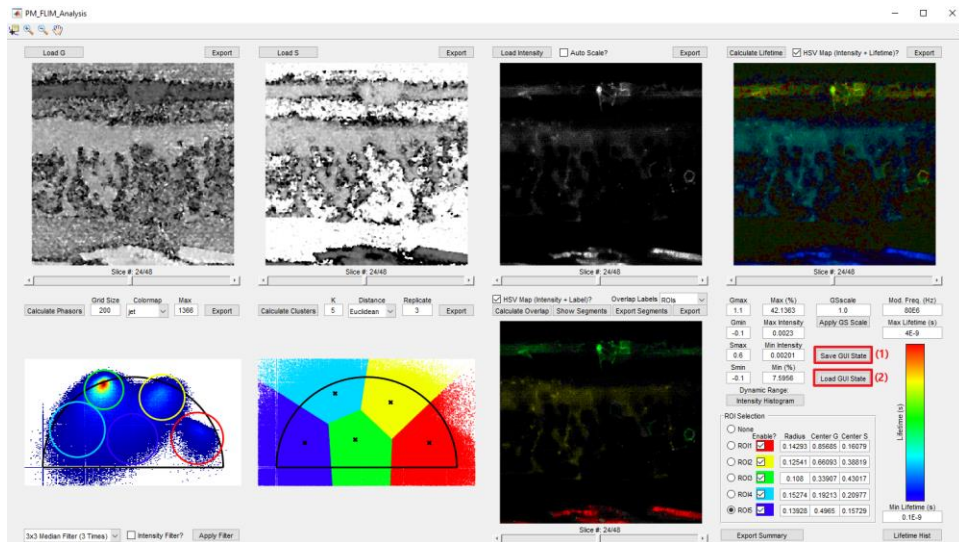


11. Save/Load Program States

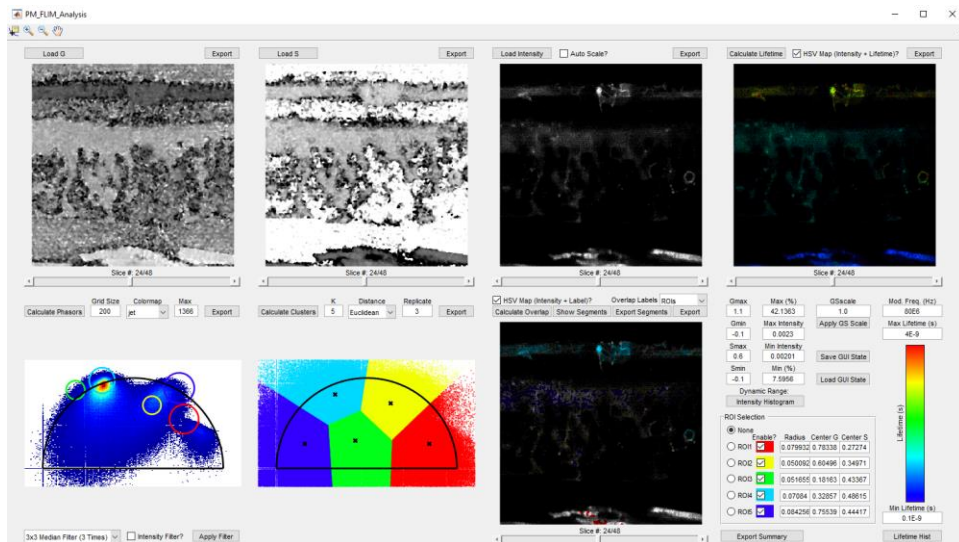
The program allows the user to save the GUIs’ current states, including the values of all edit boxes, pop-up menus, radio buttons, checkboxes, and most importantly, the radii and locations of the ROIs. To save the program states, click the “Save GUI State” button (1). A window will pop up asking the user to specify the file name. The file should be saved to the default directory, where the program itself locates.



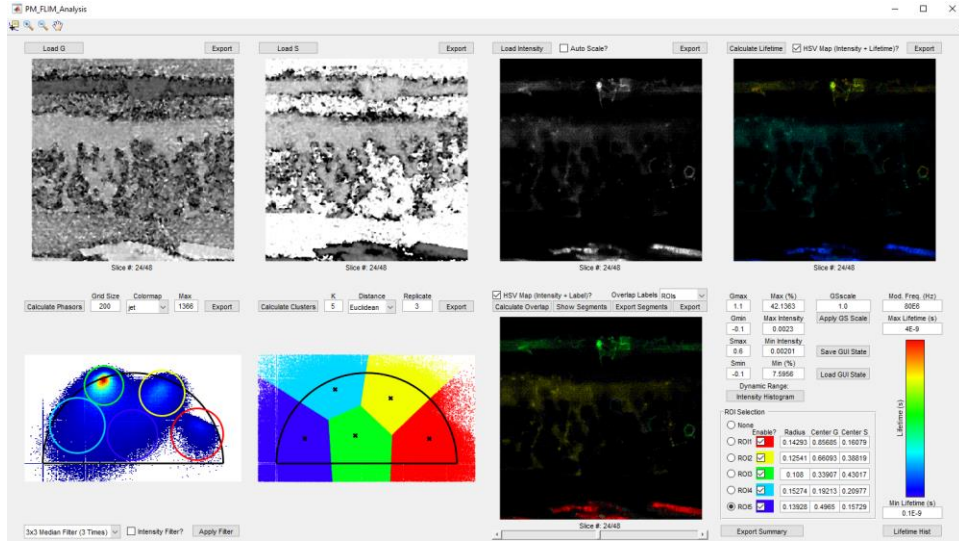
To recover the GUIs' state from a saved file, click the “Load GUI State” button (2) and select the state file (.mat) you just saved.



As an example, we modify the ROIs as follows:

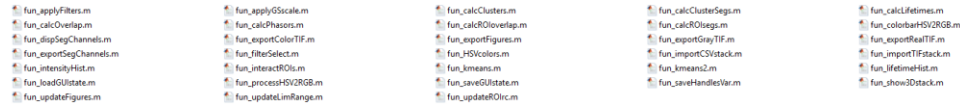


By loading the GUI state file, the ROIs, as well as other GUI elements, can be recovered to the previous states:

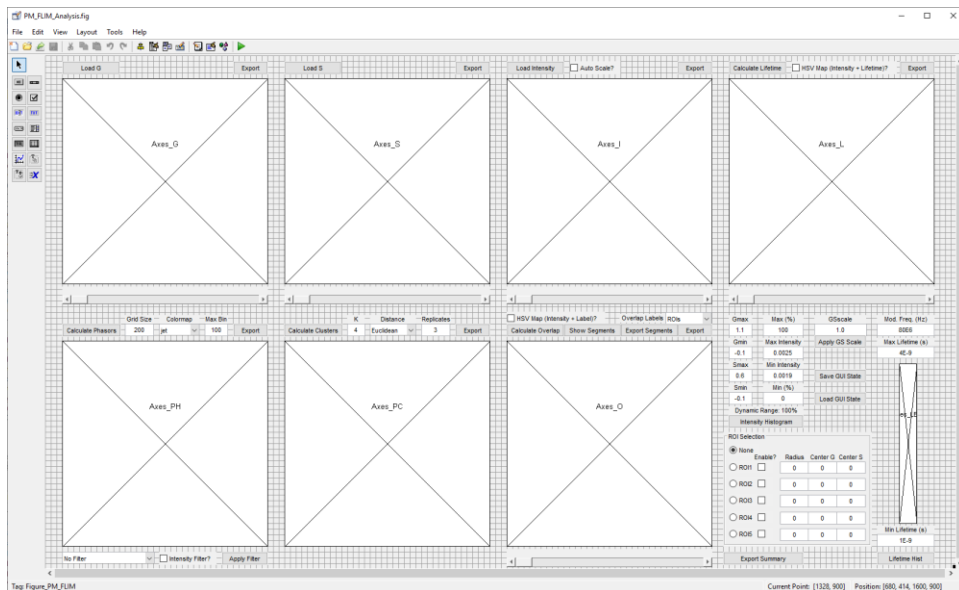


12. Add New Functions

The Instant-FLIM-Analysis program is fully open-source and highly modularized into subfunctions. Users with Matlab programming expertise can easily modify the code to customize existing functions or to add new functions in the “functions” folder:



The GUI can also be changed using Matlab’s “guide” command:



References

1. Ranjit, S., Malacrida, L., Jameson, D. M. & Gratton, E. Fit-free analysis of fluorescence lifetime imaging data using the phasor approach. *Nat. Protoc.* **13**, 1979–2004 (2018).
2. Berezin, M. Y. & Achilefu, S. Fluorescence Lifetime Measurements and Biological Imaging. *Chem. Rev.* **110**, 2641–2684 (2010).
3. Jain, A. K. Data clustering: 50 years beyond K-means. *Pattern Recognit. Lett.* **31**, 651–666 (2010).
4. Zhang, Y. *et al.* Automatic segmentation of intravital fluorescence microscopy images by K-means clustering of FLIM phasors. *Opt. Lett.* **44**, 3928–3931 (2019).